

EXPERIMENTAL INVESTIGATION OF THE INTERACTION
BETWEEN THE ELECTRON GAS AND THE EXCITED ATOMS IN A PLASMA
BY MEANS OF A XENON LASER

By

R. Freiberg and L. Goldstein

Scientific Report No. 2

November 1966

Sponsored by
National Aeronautics and Space Administration
NASA NGR 14-005-037

Gaseous Electronics Laboratory
Department of Electrical Engineering
Engineering Experimental Station
University of Illinois
Urbana, Illinois

ABSTRACT

The study of the interaction between the electron gas and the atoms in excited states has been undertaken for a gas discharge situated in a high gain optical cavity. Of particular interest is the effect of lasering upon this interaction. Spatially resolved electron density and electron temperature measurements are presented for a DC excited $3.51\ \mu$ ($5d_{33} \rightarrow 6p_{22}$) xenon laser operating in a capillary bore tube over a pressure range of 12.5 to 25.5 m Torr. Anode directed gradients in the electron and neutral gas densities are observed and are attributed to electrophoretic effects present in the closed capillary discharge tube. As a result of these gradients, the local population inversion along the axis of the tube varies and, consequently, affects the output of the $3.51\ \mu$ laser. The influence of lasering upon these low-pressure capillary xenon discharges is investigated experimentally by periodically spoiling the Q of the laser cavity by means of a mechanical chopping wheel. It is observed that lasering noticeably alters both the state of the electron gas and the populations of the excited xenon atoms. The current of the DC excited discharge is quenched up to 0.02 per cent during lasering due to laser-induced variations of the electron density and mean energy. Spatially resolved microwave cavity measurements indicate that the electron number density may experience increases and decreases depending upon local discharge conditions. Microwave radiometric measurements reveal that the electron temperature is also affected by lasering. Variations in the microwave cavity Q and in the electron drift velocity due to lasering are in good qualitative agreement with the radiometric data. Confirming spectroscopic observations of laser-induced changes in the spontaneous

radiation along the discharge tube are presented. It is demonstrated that excitation of the 6s metastables via electronic impact is instrumental in populating the lower laser level and contributes to a reduction in the local population inversion. Evidence for various radiative and collisional mechanisms responsible for the propagation of the laser-induced perturbation from the $5d_{33}$ and $6p_{22}$ levels to other excited levels is also presented. It is suggested that laser media in general can be analyzed and improved upon by studying the laser-induced changes in the excitation and relaxation processes.

ACKNOWLEDGMENT

The author wishes to express his sincere gratitude to Professor J. T. Verdeyen for his many helpful suggestions and discussions and to Dr. L. A. Weaver for his substantial contributions and assistance. The author gratefully acknowledges the members of the Gaseous Electronics Laboratory for their many helpful comments.

The author wishes to extend his thanks to Mr. R. A. Kawcyn and Mr. L. Dreyer for their contributions with electronic design and instrumentation. Special thanks are extended to Mr. M. E. Fein for his assistance in computer programming. The technical services of Messrs. M. Watson, K. Kuehl, E. Boose and A. Wilson are gratefully acknowledged. Special thanks are also due to Mrs. W. J. James for her help in typing, Mr. B. Sandorfi for the preparation of the diagrams and the staff of the Publications Office in preparing the manuscript for publication.

The author is grateful for the support of the National Aeronautics and Space Administration and the Air Force Cambridge Research Laboratories, under whose sponsorship this work was performed. The author also wishes to thank the National Science Foundation for their two years of fellowship support during this investigation.

TABLE OF CONTENTS

	Page
I. INTRODUCTION	1
II. THEORETICAL FOUNDATIONS FOR ELECTROMAGNETIC INTERACTIONS IN GASEOUS PLASMAS	6
2.1 Effects of Optical Radiation upon the Excited Atomic Populations	6
2.1.1 Gain Requirement for Lasering	7
2.1.2 Excitation and Decay Mechanisms for Excited Atomic States	13
2.2 Microwave Interaction with the Electron Gas	17
2.2.1 Conductivity of an Ionized Gas	18
2.2.2 Influence of an Electron Gas upon a Microwave Cavity	24
2.2.3 Microwave Noise Emitted by a Radiating Plasma	28
III. EXPERIMENTAL APPARATUS AND TECHNIQUES	31
3.1 Vacuum and Gas Filling System	32
3.2 Design of the Xenon Laser	34
3.3 Electrical Circuitry for Monitoring Current Variations ..	36
3.4 Microwave Cavity Circuitry	39
3.5 Plasma Emissivity Measurements	46
3.6 Microwave Noise Power Measurements	52
3.7 Spectroscopic System	54
IV. EXPERIMENTAL OBSERVATIONS AND RESULTS	57
4.1 Characteristics of the Xenon Laser Discharge	58
4.2 The Effects of Lasering upon the Electron Gas	72

TABLE OF CONTENTS - (continued)

	Page
4.2.1 Laser-Induced Current Quenching	72
4.2.2 Laser-Induced Electron Density Perturbation	74
4.2.3 Laser-Induced Electron Temperature Variation	80
4.3 Effects of Lasering upon the Excited Atomic State Populations	86
V. SUMMARY AND CONCLUSIONS	99
APPENDIX A	103
APPENDIX B	114
APPENDIX C	116
LIST OF REFERENCES	120
VITA	125

LIST OF TABLES

Table		Page
1	ESTIMATED LIFETIMES OF THE 5d STATES OF XENON USING THE BATES-DAMGAARD APPROXIMATION	69
2	ESTIMATED LIFETIMES OF THE 6p STATES OF XENON USING THE BATES-DAMGAARD APPROXIMATION	70
3	EXPERIMENTALLY OBSERVED LASER-INDUCED CURRENT AND ELECTRON DENSITY DECREASES AND COMPUTED CHANGES IN ELECTRON DRIFT VELOCITY AT A XENON PRESSURE OF 18.5 m Torr WITH ALL QUANTITIES EXPRESSED AS A PERCENTAGE OF THEIR NON-LASERING VALUES	87
4	RELATIVE LINE STRENGTHS OF THE (5d \rightarrow 6p) TRANSITIONS IN XENON USING THE j-l COUPLING SCHEME OF RACAH	92
5	COMPUTER SOLUTION OF THE RELATIONSHIP BETWEEN THE ELECTRON DENSITY AND THE RESONANT FREQUENCY SHIFT OF THE TM ₀₁₀ MICROWAVE CAVITY	115

LIST OF FIGURES

Figure		Page
1.	Vacuum and gas filling system.	33
2.	Design of xenon laser tube.	35
3.	Overall view of the shock-mounted 3.51 μ laser assembly.	37
4.	Schematic diagram of the circuit used to monitor laser-induced variations of the discharge current.	38
5.	Schematic diagram of the microwave cavity apparatus used to measure laser-induced electron density perturbations.	42
6.	TM ₀₁₀ microwave cavity resonance characteristics for the cathode end of the discharge at a xenon pressure of 12.5 m Torr. Curve A, steady-state cavity response for the non-lasering plasma; Curve B, perturbation of the cavity response induced by lasering.	43
7.	TM ₀₁₀ microwave cavity resonance characteristics for the center of the discharge at a xenon pressure of 25.5 m Torr. Curve A, steady-state cavity response for the non-lasering plasma; Curve B, perturbation of the cavity response induced by lasering.	45
8.	Bottom half of demountable section of X-band waveguide, showing position of laser tube within the guide assembly.	48
9.	Assembled view of the demountable waveguide section and the associated supporting structure.	49
10.	Schematic diagram of the microwave apparatus used to measure the plasma absorptivity and radiated noise power.	51
11.	Photograph of experimental system used to measure the electron temperature of the xenon discharge.	55
12.	Schematic diagram of the spectroscopic apparatus used to monitor the laser-induced intensity variations of the spontaneous emission.	56
13.	Spatial dependence of the steady-state 9923 Å spontaneous emission intensity at various values of discharge current.	59

LIST OF FIGURES - (continued)

Figure		Page
14(a).	Spatial dependence of the steady-state electron density at a discharge current of 50 ma for various xenon pressures.	60
14(b).	Current dependence of the steady-state electron density at a xenon pressure of 18.5 m Torr at various axial locations. Curve A, anode; Curve B, between anode and center; Curve C, center; Curve D, between center and cathode; Curve E, cathode.	60
15.	Current dependence of the 3.51 μ laser output for various xenon pressures.	67
16.	Simplified energy level diagram of the xenon system.	68
17.	Current dependence of the laser-induced quenching of the discharge current at a xenon pressure of 18.5 m Torr.	73
18.	Current dependence of the electron density perturbation due to lasering at a xenon pressure of 25.5 m Torr at various locations along the discharge.	76
19.	Current dependence of the laser-induced electron density perturbation at a xenon pressure of 18.5 m Torr at the center of the discharge.	77
20.	Current dependence of the electron temperature variations due to lasering at the center of the discharge for a xenon pressure of 18.5 m Torr.	83
21.	Comparison of the current dependence displayed by the laser-induced perturbations of the sidelight and the electron density at the center of the discharge for a xenon pressure of 18.5 m Torr.	89
22.	Current dependence of the laser-induced perturbation of the 9923 Å sidelight at the anode end of the discharge for various pressures.	94
23.	Comparison of the current dependence displayed by the laser-induced sidelight perturbations at the anode end of the discharge for a xenon pressure of 18.5 m Torr.	96

LIST OF FIGURES - (continued)

Figure		Page
24.	Cross-sectional view of the plasma-filled, quartz discharge tube within the TM_{010} microwave cavity.	107
25.	Schematic circuit diagram of the phase sensitive detector.	117
26.	Schematic circuit diagram of the biasing supply for the diode switch.	118
27.	Schematic circuit diagram of the low-noise transistorized amplifier for the InSb detector.	119

I. INTRODUCTION

In general a gaseous discharge is a highly complex nonequilibrium system of competing radiative and nonradiative reactions. The electrons, neutral atoms and excited atoms interact with one another via electron-atom and atom-atom collisions. Placing the active medium within a high gain optical cavity drastically increases the intensity of the optical radiation fields of the laser transition. The onset of lasering, therefore, imposes a highly selective population perturbation upon the upper and lower laser states. This effect constitutes a powerful means of studying the interaction between the electron gas and the excited atoms in the plasma. Previous investigations^{1,2,3,4,5} have shown that lasering indeed constitutes an effective means of changing many of the excited state populations within the active laser medium. The initial laser-induced disturbance of the laser levels is transmitted to lower-lying levels via spontaneous radiative decay processes. As a result, a change is produced in the intensity of the spontaneous emission radiated by atoms excited in these states. However, it has also been observed that the spontaneous emission from energy levels lying above the upper laser level also experience the effects of lasering. The transfer of the initial laser-induced perturbation to such states is clearly nonradiative and implies that collisional processes between the electrons and excited atoms and in some cases between neutral atoms and excited atoms are of importance. Additional evidence supporting the existence of strong electron-excited atom interactions is displayed by the observed decrease of the current flowing through DC excited discharges during lasering.^{5,6,7,8,9}

Thus, the electron gas not only serves to couple the laser disturbance to other excited states, but is itself influenced by the process of lasering.

The primary goal of this investigation is to determine the nature and strength of the interaction between the electron gas and the gas of excited atoms by means of the measurably observed effects of lasering upon gas discharges. Furthermore, a description of the physical processes responsible for the observed interaction is sought. In particular, the high gain 3.51μ ($5d_{33} \rightarrow 6p_{22}$) xenon laser was chosen as a means by which low-pressure xenon discharges could be studied. However, it must be pointed out that the particular laser was selected as a matter of convenience. The approach and the conclusions of these experiments are completely general and are equally applicable to any lasering system.

In order to investigate the state of the electron gas, microwave techniques were employed. The correlated study of the excited atomic gas was performed using spectroscopic techniques. Spatially resolved electron density measurements, taken at various positions along the discharge tube, were made using a demountable C-band microwave cavity operating in the TM_{010} mode. Electron densities between 8×10^{10} to 2×10^{12} electrons/cc were measured for discharge currents up to 100 ma over a pressure range of 12.5 to 25.5 m Torr. An anode-directed electron density gradient was observed which increased with increasing gas pressure. This axial inhomogeneity was attributed to a preferential loss of ion momentum due to collisions with the walls of the discharge tube. Microwave measurements of the plasma emissivity in conjunction with microwave radiometric measurements of the noise power radiated by the plasma indicate that the electron temperature is typically

between 8,000 to 10,000 $^{\circ}\text{K}$ if a Maxwellian velocity distribution is assumed. Spectroscopic techniques are utilized in order to monitor the intensity of the spontaneous emission radiated perpendicular to the axis of the tube. The axial inhomogeneity of the plasma is also exhibited in the positional dependence of the sidelight intensity which increases toward the anode.

By mechanically chopping the laser cavity and employing a phase sensitive detector whose reference signal is in synchronism with the chopped laser output, the effects of lasering upon various plasma parameters can be monitored. Spatially resolved measurements of the laser-induced electron density changes were made possible through the development of a more sensitive plasma diagnostic technique¹⁰ incorporating the spatial resolution of a microwave cavity with the sensitivity of a synchronous detector. The electron density exhibited laser-induced increases and decreases of approximately 10^9 electrons/cc in magnitude depending upon local discharge conditions. Similarly, changes in the plasma emissivity and radiation temperature were also recorded. Assuming the distribution function remains Maxwellian during lasering, these changes corresponded to electron temperature variations $\lesssim 0.4$ per cent in some cases. In general, the electron temperature is enhanced in regions of electron density depletion. On the other hand, when the electron density is increased, the temperature displays a quenching. Calculations based upon the laser-induced current quenching and observed variations in cavity Q are in good qualitative agreement with the electron density and temperature measurements. The net change in the rate of ionization from the upper laser level and the xenon metastables is suggested as the dominant mechanism for the laser dependent perturbation of the electron gas.⁵ Spectroscopic observations

of the spontaneous sidelight variation indicate that cumulative ionization is accompanied by cumulative excitation processes. The term cumulative implies the excitation or the ionization involved takes place via successive inelastic collisions between the electrons and the excited atoms, i.e., the final state is realized in a stepwise fashion beginning with the ground state in contrast to direct excitation in which only a single collision with a ground state atom is involved. The laser-induced disturbance is coupled to states lying above the laser levels by either direct or cumulative electronic excitation processes; therefore, variations in the populations of the excited atomic states strongly reflect any changes in the state of the electron gas. On the other hand, lower levels which are radiatively coupled to the laser states reflect changes in the local population inversion, which is also, of course, influenced by the electron gas.

For electron densities in excess of 10^{12} electrons/cc, the Q of the microwave cavity was seriously degraded and under these conditions only qualitative measurements of laser-induced changes, Δn_e and ΔT_e , could be made. However, at lower steady-state densities, good quantitative reliability existed. The output of the xenon laser was analyzed spectroscopically and found to contain several weakly oscillating transitions between 2.2μ and 3.6μ ; since their effects were quite small in comparison with those of the 3.51μ laser, no elaborate attempts were made to discriminate against them.

The spectroscopic notation adopted to describe the xenon energy levels is a modified Racah or systematic notation.^{11,12} This notation is particularly suitable for systems whose energy level structure obeys a $j-l$ coupling scheme;^{13,14} xenon, which is a heavy noble gas, is an excellent candidate.

The first subscript represents the intermediate quantum number K less $1/2$, and the second subscript is the total angular momentum J . The other symbols retain their conventional meaning.

In summary, the investigation describes excitation and ionization processes important to an understanding of gas lasers, and outlines a powerful diagnostic method of probing laser media in general.

II. THEORETICAL FOUNDATIONS FOR ELECTROMAGNETIC INTERACTIONS IN GASEOUS PLASMAS

The primary theoretical and experimental objective of the present investigation is to attain a greater understanding of the interaction between electromagnetic radiation and ionized media. Of particular concern is the influence of the laser fields upon the excited state population of the atoms and the parameters of the electron gas in a DC discharge located within a high-gain optical cavity. An investigation of the laser-induced perturbation of these quantities in conjunction with an appropriate theoretical treatment can yield information concerning the nature of the physical mechanisms involved. Probing the electron gas with a low-level electromagnetic wave in the microwave range reveals the nature and magnitude of the effects produced by lasering upon the electron density and temperature. Therefore, it is the purpose of this chapter to prepare a theoretical foundation for the influence of electromagnetic radiation upon a gaseous plasma as it pertains to a spectroscopic and microwave study of lasering gas media.

2.1 Effects of Optical Radiation upon the Excited Atomic Populations

The chief concern of this section is the interaction between an optical radiation field and a system of appropriately excited atoms. In particular, the effect produced by a highly monochromatic beam of resonance radiation in passing through a collection of excited atoms is treated theoretically. In addition, a theoretical description of the physical processes responsible for the establishment of an inverted population is presented and the expression of the gain requirement for lasering is developed.

2.1.1 Gain Requirement for Lasering

In order to develop the theoretical foundation for the effect of resonant laser radiation fields upon the excited atoms of a gas discharge, we treat the following hypothetical case. Consider a monochromatic, parallel beam of light having a frequency ν_{21} , propagating in the +z direction and passing through a layer of excited atoms bounded by the planes z and z + dz. Focusing attention upon a particular transition, suppose there are n_1 atoms per cc in the lower level which are capable of absorbing radiation of frequency ν_{21} and n_2 atoms per cc in the upper level which are capable of emitting this frequency. Neglecting the effects of spontaneous emission since it occurs in all directions, the decrease in the beam intensity per unit area $-dI_{\nu_{21}}$, according to the Einstein theory of radiation,¹⁵ is given by

$$-dI_{\nu_{21}} = (n_1 \Gamma_{12} - n_2 \Gamma_{21}) h \nu_{21} dz \quad (2-1)$$

where Γ_{12} is the probability per second that an atom in the lower state will absorb a photon $h \nu_{21}$ and undergo a transition to the upper level.

Similarly, Γ_{21} is the probability per second that the incident radiation induces an atom in the upper state to emit a photon of the same frequency and in the same direction as the stimulating quantum and in the process drop into the lower state. These probability rates are expressible in terms of the Einstein B coefficients

$$\Gamma_{12} = B_{12} w L(\nu) \quad (2-2)$$

$$\Gamma_{21} = B_{21} w L(\nu) \quad (2-3)$$

where w is the radiation energy density and $L(\nu)$ is the normalized line shape of the atomic resonance.

It must be emphasized here that, in laser theory, we are primarily concerned with the response of a system of excited atoms to resonance radiation of extremely high spectral purity whose energy is distributed over a spectral range which is appreciably smaller than the atomic absorption linewidth. Therefore, in order to discuss the transition probabilities for absorption and induced emission, it is necessary to introduce the concept of atomic line shape $L(\nu)$. For the low-pressure conditions under which the gas lasers are operated, the origin of the line shape is the thermal motion of the atoms and the resultant Doppler effect. The term, inhomogeneously-broadened, is applied to a transition that exhibits gain and whose natural linewidth is small compared to the Doppler width.

In a plane wave the energy densities stored within the electric and magnetic fields are equal at any point and the time average of the total energy density of these sinusoidally time-varying fields is given by

$$w = \frac{\epsilon E^2}{8\pi} = \frac{\mu H^2}{8\pi} \quad (2-4)$$

where ϵ and μ are the dielectric constant and magnetic permeability of the ionized gaseous medium and E and H are the peak electric and magnetic fields of the incident beam, respectively.

A laser consists of a Fabry-Perot interferometer filled with a gas of excited atoms which are capable of amplifying light of frequency ν_{21} . The amplification is due to the process of stimulated emission which has the unique property of preserving the frequency, phase and direction of the stimulating quanta. The interferometer plays the role of a multimode resonant cavity, which, by virtue of its highly reflective mirrors, supplies positive feedback necessary for oscillation.

If the gain of the medium at the frequency ν_{21} is large enough to compensate for the losses at this frequency due to various loss processes, the system of excited atoms will break into oscillation. Among the dominant loss mechanisms are the following: absorption and transmission in the laser cavity mirrors, scattering by optical inhomogeneities and diffraction of the light beam due to the finite aperture of the mirrors. The total power loss at the resonant frequency ν_{21} can be expressed in terms of the quality factor Q of the resonant optical cavity.¹⁶

$$Q = \frac{2\pi \nu_{21} W}{P_{\text{loss}}} \quad (2-5)$$

where W is the total energy stored in the resonator fields and is given by

$$W = \int_{\text{resonator}} w \, dV = \frac{1}{8\pi} \int_{\text{resonator}} \epsilon E^2 \, dV \quad (2-6)$$

The net power gained by the monochromatic beam via interactions with the excited atoms in states 1 and 2 is given by

$$P_{\text{gain}} = (n_2 B_{21} - n_1 B_{12}) \hbar \nu_{21} w V L(\nu) \quad (2-7)$$

where V is the volume occupied by the excited atoms which interact with the laser beam.

If the resonant cavity is filled with the active medium and has a resonant frequency equal to that of the atomic transition, the threshold requirement for oscillation at a frequency ν_{21} is given by

$$n_2 - n_1 \frac{B_{12}}{B_{21}} = [\hbar Q B_{21} L(\nu)]^{-1} \quad (2-8)$$

The Einstein B coefficients which are a measure of the interaction between the atoms and the radiation field can be expressed in terms of the electric dipole matrix element.

$$B_{21} = \frac{2\pi |\mu_{21}|^2}{3 \hbar^2 g_2} \quad (2-9)$$

$$B_{12} = \frac{2\pi |\mu_{21}|^2}{3 \hbar^2 g_1} \quad (2-10)$$

where g_i is the degeneracy of the i^{th} state and $|\mu_{21}|^2$ is the square of the total electric dipole moment summed over all degenerate initial and final substates.

The Einstein A_{21} coefficient is defined as the probability per second that an atom in the upper state will spontaneously emit a photon of frequency ν_{21} in a random direction and in the process fall into the lower state.

$$A_{21} = \frac{64 \pi^4 \nu_{21}^3 |\mu_{21}|^2}{3 h c^3 g_2} \quad (2-11)$$

Unlike induced emission the probability for spontaneous emission is completely independent of the radiation fields of the incident beam. Therefore, the minimum inverted population density required for lasering is given by

$$(\Delta n)_{\text{threshold}} = \left(n_2 - n_1 \frac{g_2}{g_1} \right) = \frac{16 \pi^2 \nu_{21}^3}{c^3 A_{21} Q L(\nu)} \quad (2-12)$$

threshold

If the atomic absorption linewidth is Doppler-broadened, the normalized atomic line shape is a Gaussian function of the frequency centered about the resonance frequency ν_{21} ¹⁷

$$L(\nu) = \sqrt{\frac{\ln 2}{\pi}} \frac{1}{\Delta \nu_D} \exp \left\{ - \ln 2 \left[\frac{(\nu - \nu_{12})}{\Delta \nu_D} \right]^2 \right\} \quad (2-13)$$

where $\Delta \nu_D$ is the half-width of the line at half maximum intensity and is given by

$$\Delta \nu_D = \nu_{12} \sqrt{\frac{2 k T \ln 2}{M c^2}} \quad (2-14)$$

M is the atomic mass and T is the absolute temperature of the gas.

For a Doppler-broadened laser transition, Equation (2-12) reduces to

$$(\Delta n)_{\text{threshold}} = \frac{16 \pi^{5/2} \nu_{21}^3 \Delta \nu_D}{(\ln 2)^{1/2} Q A_{21}} \quad (2-15)$$

It is often convenient to express the population inversion in terms of the fractional intensity gain of the monochromatic beam per unit length.

Beginning with Equation (2-1), it can be shown that

$$G_{21} = \frac{1}{I_{\nu_{21}}} \frac{d I_{\nu_{21}}}{dz} = \frac{(\ln 2)^{1/2}}{4\pi^{3/2}} \frac{g_2 A_{21} c^2}{\nu_{21}^2 \Delta \nu_D} \left(\frac{n_2}{g_2} - \frac{n_1}{g_1} \right) \quad (2-16)$$

Therefore, the fractional gain per unit length is inversely proportional to $\nu_{21}^2 \Delta \nu_D$, i.e.,

$$G_{21} \propto \nu_{21}^{-3} \left(\frac{M}{T} \right)^{1/2} \quad (2-17)$$

Consequently, the gain is expected to be larger for lasering transitions in the infrared as compared to those in the visible. Furthermore, the heavy noble gas lasers such as xenon have smaller Doppler widths which also contribute to higher gain. It is also apparent that significant cooling of the lasering gas can also result in slight increases in gain.

The threshold condition for lasering requires an inverted population distribution between the upper and lower levels. It is quite obvious that an atomic system exhibiting gain is, by definition, not in thermodynamic equilibrium with its environment. The concept of negative temperature is frequently used in the discussion of lasers where an effective temperature can be defined in terms of the relative populations of the upper and lower states of the transition.¹⁸

$$\frac{n_2}{n_1} = \frac{g_2}{g_1} \exp \left[- \frac{(E_2 - E_1)}{k T_{\text{eff.}}} \right] \quad (2-18)$$

Since $n_2 > n_1$ for a transition exhibiting gain, $T_{\text{eff.}} < 0$.

2.1.2 Excitation and Decay Mechanisms for Excited Atomic States

The relative lifetimes of the laser levels are among the most important parameters of the plasma, for if an inverted population cannot be maintained, no lasering will ensue. The effective lifetimes of the excited levels can differ considerably from their purely radiative values due to the combined effects of resonance trapping, spontaneous decay and inelastic collisions between atoms and electrons.

Consider an excited level which is optically connected with the ground state. A typical rate equation for this m^{th} excited state is given by

$$\begin{aligned} \frac{d N_m}{dt} = & - F A_{m0} - \sum_{\substack{n < m \\ n \neq 0}} A_{mn} + n_e N_0 \langle \sigma v \rangle_o^m \\ & - n_e N_m \sum_p \langle \sigma v \rangle_m^p - N_m N_0 \langle \sigma v \rangle_m^o \end{aligned} \quad (2-19)$$

where F is the imprisonment factor for resonance radiation trapping, N_m is the population of the m^{th} state and $\langle \sigma v \rangle_r^s$ denotes the velocity averaged product of the relative velocity v of the collision partners and cross section σ for the reaction from the r^{th} state to the s^{th} state.

The first term on the right-hand side of the above equation involves the imprisonment factor F which can vary between zero and unity. It is a measure of the effective trapping of spontaneous emission between the excited level and the ground state after repeated emission and reabsorption. The imprisonment factor is a function of the discharge geometry, pressure,

temperature, line shape, wavelength and transition probability.

For a Doppler-broadened line and a cylindrical discharge of radius R , the imprisonment factor is given by¹⁹

$$F = 1.60 / K R \sqrt{\pi \ell_n K R} \quad (2-20)$$

where

$$K = \frac{\lambda^3 N_o g_m}{8 \pi g_o} A_m \sqrt{\frac{M}{2 \pi k T}} \quad (2-21)$$

M is the mass of the atom, g_m and g_o are the statistical weights of the m^{th} and ground states, respectively, λ is the wavelength of the radiation, A_m is the Einstein coefficient of the m^{th} level and T is the temperature of the gas.

At pressures of a few m Torr, the departure of F from unity is quite pronounced; and at the low pressures used in most gas lasers, the trapping is essentially complete for the strong vacuum ultraviolet transitions involving the laser levels.²⁰ In the noble gas lasers the levels in the $(n p)^5 (n + 1) s$ which are not metastable due to quantum mechanical selection rules are rendered quasi-metastable due to the strong resonant trapping. The principal quantum number n corresponds to 2, 3, 4 and 5 for Ne, Ar, Kr and Xe, respectively.

The summation appearing in the second term of Equation (2-19) implies that the sum is to be taken over all allowable states below m except for the ground state, i.e., all possible spontaneous decay routes are to be taken into account.

The last two terms of Equation (2-19) involve inelastic encounters of the m^{th} excited state with atoms and electrons. $n_e N_o < \sigma v >_o^m$ represents the contribution of direct electron excitation from the ground state. The summation on the next term $n_e N_m \sum_p < \sigma v >_m^p$ represents the sum of various loss mechanisms due to electron impact, i.e., successive excitation to higher lying excited states, ionization and superelastic collisions. The last term $N_m N_o < \sigma v >_m^o$ represents the losses due to inelastic collisions with neutral atoms. Mechanisms represented by the last two terms are important only if the density of the collision partners is large and the lifetime of the m^{th} excited state is relatively long. The cross sections σ pertaining to these processes differ considerably in magnitude and are dependent upon the nature of the reaction, the relative velocity of the collision partners and the energy levels involved.

Atoms in metastable states have lifetimes which are typically orders of magnitude longer than those in excited states capable of spontaneous radiative decay. The metastable states are depopulated mainly by diffusion and by inelastic collisions with electrons and other atoms. The rate equation for the metastable density M can be expressed as

$$\frac{dM}{dt} = S - \Gamma M \quad (2-22)$$

where S is the rate at which the metastables are produced via radiative cascade from higher-lying states. The total decay rate expressed by Γ can be subdivided into its individual contributors.

$$\Gamma = \gamma_D + \gamma_o + N_o < \sigma v >_M^o + n_e \sum_n < \sigma v >_M^n \quad (2-23)$$

At high discharge intensity the metastable temporal behavior may depart from Equation (2-22) due to metastable-metastable collisions. However, at low pressure and for the discharge geometry used in most gas lasers, namely, the small-bore discharge tube, the primary mode of metastable destruction is by diffusion to the walls or by two body collisions. The terms γ_D and γ_0 in Equation (2-23) represent the diffusion and the volume loss mechanisms which are characteristic of the pure gas. γ_D can be expressed in terms of the diffusion coefficient D , the diffusion length Λ and the pressure P .²¹

$$\gamma_D = \frac{D}{\Lambda^2 P} \quad (2-24)$$

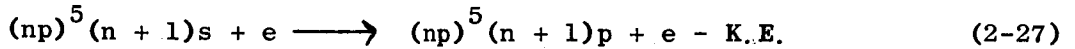
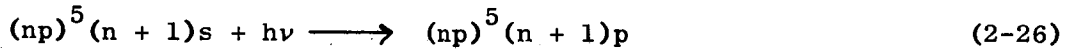
The diffusion length is a function of the discharge geometry.

$$\frac{1}{\Lambda^2} = \left(\frac{\pi}{L} \right)^2 + \left(\frac{2.4}{R} \right)^2 \quad (2-25)$$

L is the length and R the radius of the cylindrical discharge. It is apparent from Equations (2-24) and (2-25) that the rate at which the metastables are lost by diffusion to the walls can be accelerated by decreasing the inside diameter of the discharge tube.

The last two terms of Equation (2-23) denote the losses due to collisional effects. The first of these, $N_0 < \sigma v >_M^0$, is the collisional de-excitation of the metastable state due to inelastic encounters with neutral atoms. Such a mechanism is extremely important in the He-Ne lasers. The He metastable collisionally excites the ground state neon atom into the upper laser level and is primarily responsible for establishing the inverted

population in the lasering neon transitions. The last term, $n_e \sum_p < \sigma v >_M^p$, is the loss term due to the combined effects of electronic impact which results in metastable excitation, ionization or superelastic collisions. Due to the relatively long lifetimes associated with the metastables, these processes become important in regions of high electron and metastable densities. Resonance trapping and electronic excitation from the metastable states into the lower laser level degrades the population inversion. For the noble gases these reactions can be expressed, respectively, as



where $n = 2, 3, 4$ and 5 apply to Ne, Ar, Kr and Xe, respectively. Therefore, it is highly desirable to minimize the effectiveness of reactions (2-26) and (2-27) by reducing the metastable population. This accounts for the necessity of the narrow bore discharge tube which enhances the diffusional loss rate.

Since the electron gas plays an important role in determining the populations of the excited atomic states, it is essential that both the electron density as well as the mean electron energy be known. The following section deals with this aspect of the problem.

2.2 Microwave Interaction with the Electron Gas

In measuring the electron gas parameters, it is essential that the probing mechanism does not unduly perturb the plasma. Extremely low power electromagnetic waves at microwave frequencies can be used as probing signals

and can be considered to have negligible effect upon the phenomena being studied.

Three aspects of the problem are discussed in this section: the complex RF conductivity of the ionized gas, the effect of the plasma upon the resonant frequency and quality factor of the microwave cavity and the ability of the plasma to radiate a continuous noise spectrum which is related to the electron temperature.

2.2.1 Conductivity of an Ionized Gas

An ionized medium such as a plasma presents a complex conductivity to high-frequency propagating electromagnetic waves. In general, this complex quantity is defined as the ratio of the current density to the applied electric field. Since the electric current due to the motion of the free electrons in a vacuum is in quadrature with the applied electromagnetic field, the conductivity of the free electrons in a vacuum is purely imaginary. This implies that the electrons on the average extract no energy from oscillating electric fields and their mean energy is dependent only upon their mean thermal energy.

However, when the free electrons are no longer in vacuum but are in the presence of gas molecules, their directed velocities are randomized via electron-molecule collisions. This randomization causes the electrons to acquire a velocity component in phase with the oscillating electric field, enabling the electrons to extract energy from the fields. This gives rise to a real part of the conductivity which depends upon the number of collisions a particular electron will make with a gas molecule per unit time. Therefore, the conductivity of a plasma medium can be expressed as

$$\sigma = \sigma_r + j \sigma_i \quad (2-28)$$

where σ_r represents the real part of the conductivity and is associated with an energy transfer from the field to the electrons. σ_i is the imaginary component of the conductivity.

The microwave interaction with the ions can be considered negligible with respect to that of the electrons, due to the larger mass of the ions. Therefore, microwave investigations of the plasma conductivity yield information concerning only the free electrons of the plasma.

The complex conductivity $\sigma(\vec{r}, t)$ of a plasma is a function of both time and space and is dependent upon the velocity distribution of the electrons $f(\vec{r}, \vec{v}, t)$. f is by definition the probability density in the six-dimensional phase space of velocity and spatial coordinates, and constitutes the number of electrons located in the element of phase space between \vec{r} and $\vec{r} + d\vec{r}$ and \vec{v} and $\vec{v} + d\vec{v}$ at a time t . The total electron density $n_e(\vec{r}, t)$ can be expressed as an integral over all velocity space of $f(\vec{r}, \vec{v}, t)$.²²

$$n_e(\vec{r}, t) = \int f(\vec{v}, \vec{r}, t) d^3 v \quad (2-29)$$

The development of the complex conductivity in terms of the distribution function has been treated by others^{23,24,25,26} and the details can be found in the literature. The formalism is based upon the Boltzmann transport equation²⁷

$$\frac{\partial}{\partial t} f(\vec{r}, \vec{v}, t) + \vec{v} \cdot \nabla_{\vec{r}} f(\vec{r}, \vec{v}, t) + \vec{a} \cdot \nabla_{\vec{v}} f(\vec{r}, \vec{v}, t) = \left(\frac{\partial}{\partial t} f(\vec{r}, \vec{v}, t) \right)_{\text{coll.}} \quad (2-30)$$

where \vec{v} and \vec{a} are the electron velocity and acceleration due to the applied field and ∇_r and ∇_v represent the gradient operators in geometrical and velocity space. The term $\left(\frac{\partial}{\partial t} f(r, v, t) \right)_{\text{coll.}}$ represents the contribution due to collisional encounters of the electrons with other constituents of the plasma.

For the purposes of the present development, the effects of electron-electron collisions and the electron-ion collisions have been neglected in comparison with the electron-neutral collisions. The net rate of change of the number of electrons in the elemental volume d^3v in velocity space is determined by the difference between the number of electrons scattered into d^3v and the number of electrons scattered out of d^3v . The collisional term can be expressed as

$$\begin{aligned} \left(\frac{\partial}{\partial t} f(\vec{r}, \vec{v}, t) \right)_{\text{coll.}} d^3v = & \int F(\vec{v}') f(\vec{v}') v_r \sigma(v_r, \theta, \phi) d^3v' d^2\Omega \\ & - \int F(\vec{v}) f(\vec{v}) v_r \sigma(v_r, \theta, \phi) d^3v d^2\Omega \end{aligned} \quad (2-31)$$

$F(\vec{v})$ is the velocity distribution of the scattering particles, which in this case are the neutrals. The relative velocity between the neutrals and the electrons is given by v_r and the differential scattering cross section is denoted by $\sigma(v_r, \theta, \phi)$. The elemental solid angle of the scattering sphere $d^2\Omega$ is expressed as $\sin \theta d\theta d\phi$. The prime superscripts denote the contributions due to the inverse scattering, i.e., scattering into the elemental volume d^3v .

$$d N(\vec{v}') = F(\vec{v}') d^3v' \quad (2-32)$$

and

$$d n_e(\vec{v}') = f(\vec{v}') d^3 v' \quad (2-33)$$

represent the number of neutrals and electrons, respectively, which are in the proper elemental volumes of velocity space to be scattered into $d^3 V$ and $d^3 v$, respectively.

Under the influence of the electromagnetic wave, the distribution function is perturbed from its field free value. Since the incident electromagnetic wave has a preferred orientation in space, the distribution function is conveniently expanded in terms of spherical harmonics in velocity space.

$$f(\vec{r}, \vec{v}, t) = \sum_{\ell} f_{\ell}(\vec{r}, \vec{v}, t) P(\cos \theta) = f_0 + f_1(\vec{r}, \vec{v}, t) \cos \theta + \dots \quad (2-34)$$

f_0 is the unperturbed distribution function which is assumed to be isotropic in geometrical space but not necessarily Maxwellian in velocity space. For low-level electromagnetic waves only the zeroth order and first order correction $f_1(\vec{r}, \vec{v}, t)$ need be included in the expansion. Since under these conditions $f_1 \ll f_0$, higher-order contributions can be considered negligible.

For the sake of simplicity, a uniform plasma medium is assumed and the electric field is taken to be independent of position. Equation (2-30) then reduces to

$$\frac{\partial}{\partial t} f(\vec{v}, t) + \frac{e \vec{E}}{m} \cdot \nabla_v f(\vec{v}, t) = \left(\frac{\partial}{\partial t} f(\vec{v}, t) \right)_{\text{coll.}} \quad (2-35)$$

If only terms of the first order are retained, it can be shown through the use of Equations (2-31), (2-34) and (2-35) that the Boltzmann transport equation reduces to²⁸

$$\frac{\partial f_1}{\partial t} + \frac{e E}{m} \frac{\partial f_0}{\partial v} = - f_1 N v \int_{\theta, \phi} \sigma(v, \theta, \phi) [1 - P_1(\cos \theta)] \sin \theta d\theta d\phi \quad (2-36)$$

The integral on the right side of Equation (2-36) is related to the collision frequency for momentum transfer $\nu(v)$.

$$\nu(v) = N v \int_{\theta, \phi} \sigma(v, \theta, \phi) (1 - \cos \theta) \sin \theta d\theta d\phi \quad (2-37)$$

The cross section for momentum transfer is given by²⁹

$$\sigma(v) = \int_{\theta, \phi} \sigma(v, \theta, \phi) (1 - \cos \theta) \sin \theta d\theta d\phi \quad (2-38)$$

$$\therefore \nu(v) = N v \sigma(v) \quad (2-39)$$

The solution of Equation (2-36) yields the first-order term of the distribution function.

$$f_1(v) = - \frac{e E}{m} \frac{\partial f_0 / \partial v}{\nu(v) + j\omega} \quad (2-40)$$

The current density for the electrons is given by

$$J = + e n_e \left\langle \frac{\vec{E} \cdot \vec{v}}{|E|} \right\rangle \quad (2-41)$$

or

$$J = - \frac{4\pi n_e e^2}{3m} E \int_0^\infty \frac{\partial f_o / \partial v}{\nu(v) + j\omega} v^3 dv \quad (2-42)$$

Therefore, the conductivity of the plasma medium is

$$\sigma = \frac{J}{E} = - \frac{4\pi}{3} \frac{n_e e^2}{m} \int_0^\infty \frac{\partial f_o / \partial v}{\nu(v) + j\omega} v^3 dv \quad (2-43)$$

In the limiting case where $\omega \ll \nu$, which applies to the direct current limit, Equation (2-43) takes the form

$$\sigma = - \frac{4\pi n_e e^2}{3m} \int_0^\infty \frac{\partial f_o / \partial v}{\nu(v)} v^3 dv \quad (2-44)$$

Hence, the DC conductivity is purely real.

In the other extreme, where $\omega \gg \nu$, the high frequency conductivity can be expressed as

$$\sigma = - \frac{4\pi n_e e^2}{3m} \int_0^\infty \left[\frac{\nu(v)}{\omega^2} - j \left(\frac{1}{\omega} \right) \right] \frac{\partial f_o}{\partial v} v^3 dv \quad (2-45)$$

Hence, the high-frequency conductivity is complex, having both real and imaginary components.

In order to evaluate the above integrals it is necessary to know not only the electron distribution function f_o but also the velocity dependence of the collision frequency $\nu(v)$. For the special case in which the collision

frequency is independent of electron velocity,

$$f_o(v) = \left(\frac{m}{2 \pi k T} \right)^{3/2} e^{-mv^2/2kT} \quad (2-46)$$

the conductivity given by Equation (2-43) reduces to

$$\sigma = \frac{n_e e^2}{m} \frac{1}{\nu + j\omega} \quad (2-47)$$

which is exactly the Lorentz conductivity.³⁰

2.2.2 Influence of an Electron Gas upon a Microwave Cavity

In the previous subsection a development of the complex conductivity of the plasma was derived and shown to be a function of the electron number density, distribution function, momentum transfer collision frequency and the frequency of the microwave field. In the present subsection the effect of this plasma conductivity upon the resonant frequency and quality of a microwave cavity is presented.

If the influence of the electron gas upon the fields of an empty microwave cavity can be considered small, first-order perturbation theory can be applied to obtain an expression comprising the changes in both resonant frequency and quality in terms of the plasma conductivity.³¹

$$\Delta \left(\frac{1}{Q} \right) - \frac{2 j \Delta \omega}{\omega_o} = \frac{1}{\omega_o \epsilon_o} \frac{\int [\sigma_r(r) + j \sigma_i(r)] E^2(r) dV}{\int E^2(r) dV} \quad (2-48)$$

where ω_o is the angular resonance frequency of the unfilled cavity, ϵ_o is the

permittivity of free space, dV is an elemental volume of the cavity, $E(\vec{r})$ is the electric field in the cavity and $\Delta \omega$ and $\Delta \left(\frac{1}{Q} \right)$ are the shift in angular resonant frequency and change in (cavity quality)⁻¹, respectively, due to the presence of the plasma.

The assumption that the plasma can be considered as a small perturbation is valid for electron densities $\ll 2.5 \times 10^{11} \text{ cm}^{-3}$ for microwave frequencies of about 5 Gc.³² Since the majority of the electron densities encountered in this experiment exceeded this upper limit, it was necessary to solve the electromagnetic boundary value problem without the aid of perturbation theory.

A very brief outline of the development of the expression relating the electron number density and the perturbed resonant frequency is presented. The interested reader can find a more detailed development in Appendix A.

If the E field within the microwave cavity is chosen such that it is perpendicular to any gradient in electron density, then

$$\nabla \cdot \vec{E} = 0 \quad (2-49)$$

and the time-independent Helmholtz equation

$$\nabla (\nabla \cdot \vec{E}) - \nabla^2 \vec{E} = \frac{\omega^2}{c^2} n^2 \vec{E} \quad (2-50)$$

simplifies to

$$\nabla^2 \vec{E} + \frac{\omega^2}{c^2} n^2 \vec{E} = 0 \quad (2-51)$$

where n is the refractive index of the plasma. For the particular case in which the plasma is situated in a long cylindrical tube, radial gradients in the electron density exist. If only a short length of plasma is placed within the cavity, the electron density along the axis can be considered uniform. If the cavity is excited in the TM_{010} mode, the electric and magnetic fields are given by

$$\vec{E} = E_z(r) \hat{z} \quad (2-52)$$

$$\vec{H} = H_\phi(r) \hat{\phi} \quad (2-53)$$

Using Maxwell's equations and Equations (2-51) through (2-53), it can be shown that the fields within the cavity satisfy the following relation.

$$\frac{\partial^2 E_z}{\partial x^2} + \frac{1}{x} \frac{\partial E_z}{\partial x} + n^2 E_z = 0 \quad (2-54)$$

$$H_\phi = -\frac{j}{\eta_0} \frac{\partial E_z}{\partial x} \quad (2-55)$$

where $x = r \frac{2\pi}{\lambda}$, n is the index of refraction and η_0 is the impedance of free space.

Equation (2-54) is Bessel's equation.³⁴ Therefore, the electric field must be of the form

$$E_z = C_1 J_0(nx) + C_2 Y_0(nx) \quad (2-56)$$

and, likewise, the magnetic field according to Equation (2-55) must be

$$H_{\phi} = \frac{jn}{\eta_0} \left[C_1 J_1(nx) + C_2 Y_1(nx) \right] \quad (2-57)$$

where J_m and Y_m are the m^{th} order Bessel functions of the first and second kind, respectively.

The solution of this problem entails matching boundary conditions for three concentric cylindrical regions. The innermost region $0 < r < b_1$ is occupied by the plasma and has a refractive index³⁵ of

$$n(r) = \left[1 - \left(\frac{\omega_p}{\omega} \right)^2 \right]^{1/2} \quad (2-58)$$

assuming $\frac{\nu}{\omega} \ll 1$ and the plasma frequency is defined as

$$\omega_p^2 = \frac{n_e(r) e^2}{m \epsilon_0} \quad (2-59)$$

The term $n_e(r)$ indicates that the electron density has radial dependence.

The annular region occupied by the glass of the discharge tube, $b_1 < r < b_2$, has an index of refraction n_g . The last annular region between the outer wall of the discharge tube and the inner wall of the microwave cavity, $b_2 < r < a$, is filled with air and has a refractive index of unity.

The fields in the regions defined by $b_2 < r < a$ and $b_1 < r < b_2$ are of the form expressed by Equations (2-56) and (2-57). The fields within the plasma are not as easily expressed due to the radial gradient in the electron density. Fuchs³⁶ found that it was necessary to assume fields of the form

$$E_z = x^0 \sum_{n=0}^{\infty} a_n x^n \quad (2-60)$$

and solve for the appropriate values of the a_m coefficients by the method of Froebinius.

After having matched the boundary conditions at the three interfaces, $r = b_1$, b_2 and a , for both E_z and H_ϕ , a rather complex expression relating n_e and the perturbed resonant frequency is obtained. The details of the derivation appear in Appendix A and the computerized values of the electron density versus the shift in cavity resonance frequency appear in Appendix B.

2.2.3 Microwave Noise Emitted by a Radiating Plasma

Not only is the plasma capable of absorbing microwave power but it is also an effective thermal radiator of electromagnetic power in the microwave portion of the frequency spectrum. If the plasma radiated like a black body, Planck's radiation law could be evoked to determine the electron temperature.³⁷

$$\rho(\nu, T) = \frac{8 \pi h \nu^3}{c^3} \frac{1}{e^{h\nu/kT} - 1} \quad (2-61)$$

where $\rho(\nu, T)$ is the radiation energy density per unit frequency interval, ν is the frequency, T is the temperature of the radiator, h is Planck's constant, k is Boltzmann's constant and c is the velocity of light in a vacuum.

However, a plasma does not act as a perfect black body radiator and the treatment is not as straightforward. The incoherent radiation emitted by a plasma is a result of the electronic motion under the influence of atomic and ionic fields. Kirchoff's law relates $P(\nu, T)$ the radiation intensity per unit frequency interval to the temperature of the radiator as³⁸

$$P_\nu(\nu, T) = A_\nu k T \quad (2-62)$$

where A_ν is the absorptivity of the plasma, defined as

$$A_\nu = \frac{P_{\text{absorbent}}}{P_{\text{incident}}} \quad (2-63)$$

In the case of a black body $A_\nu = 1$; however, for a plasma, A_ν is typically less than unity.

Parzen and Goldstein³⁹ treated the problem of the microwave noise radiated by a DC excited plasma situated in a section of waveguide. It was shown that the noise power due to the electron-current fluctuations can be separated into two parts: one is attributed to the electron temperature and the other to the direct current flowing through the discharge.

$$P(\omega, T) = \left[k T_r A + \frac{IVA}{N_e \nu_e} \cos^2 \theta \left(2 + \frac{\nu_e^2 - \omega^2}{\nu_e^2 + \omega^2} \right) \right] \quad (2-64)$$

where

I = current through discharge

V = voltage across discharge

N_e = total number of electrons

ν_e = electron collision frequency

ω = angular frequency of emitted noise

θ = angle between electric field and axis of discharge tube

Since the discharge is oriented perpendicularly to the electric field vector, the second term is negligible and Equation (2-64) reduces to Equation (2-62).

When the electron gas is in thermodynamic equilibrium with the radiation field and possesses a Maxwellian velocity distribution, the radiation temperature T_r and T_e are identical and the mean thermal energy of the electrons is given as

$$\langle u_e \rangle = \frac{3}{2} k T_e \quad (2-65)$$

However, when the distribution function departs from a Maxwellian, the relationship between radiation temperature and the electron temperature are ill-defined. Bekefi and Brown^{40,41} treat the particular low-frequency case for which $\hbar \omega / k T \ll 1$. The radiation temperature is defined in terms of the distribution function as

$$k T_r = - m \frac{\int_0^{\infty} \sigma(v) f v^5 dv}{\int_0^{\infty} \sigma(v) \frac{\partial f}{\partial v} v^4 dv} \quad (2-66)$$

where m is the mass of an electron, f is the velocity distribution function and σ is the total collision cross section for momentum transfer between the electrons and the other constituents of the plasma. Therefore, either a change in the electron mean energy or a change in the distribution function can result in a change in the radiation temperature. The apparatus which was used to measure the radiation temperature is discussed in detail in Chapter III.

III. EXPERIMENTAL APPARATUS AND TECHNIQUES

During the course of the investigation it became necessary to employ several different techniques to study in detail the properties of the electron gas, as well as those associated with the excited atoms over a current range of 0 to 100 ma and a pressure range from 12.5 to 25.5 m Torr. The state of the electron gas was probed by microwave techniques. A microwave cavity was used to obtain spatially resolved electron density measurements in the DC excited capillary xenon discharge. Waveguide techniques were employed to determine the plasma absorptivity and to measure the microwave noise power radiated by the plasma. These two experimental quantities yield information concerning the electron temperature, provided the energy distribution of the electrons is known. Correlations between the laser-induced behavior of the electron gas and the perturbation of the excited atomic populations were obtained by means of spectroscopic techniques. By monitoring the spontaneous emission radiated perpendicular to the axis of the discharge tube, information regarding the populations of various excited atomic states was obtained.

The above techniques were instrumental not only in examining the steady-state properties of xenon discharge but also in determining effects imposed upon these parameters by the intense laser radiation.

In order to observe the influence of lasering upon the parameters of the discharge, a motor-driven chopping wheel was employed to periodically spoil the Q of the laser cavity. However, since the effects of lasering are rather small, it was necessary to employ synchronous detection in order to increase the sensitivity of the diagnostic techniques. These techniques

for measuring the steady-state properties of the plasma as well as their laser-induced perturbations and the details pertaining to the design of the vacuum system and the xenon laser are the subject matter of this chapter.

3.1 Vacuum and Gas Filling System

Figure 1 schematically illustrates the vacuum system which was used in evacuating and filling the xenon laser tubes. The main manifold, the five bakeable Granville-Phillips valves, the three vacuum gauges and the copper foil trap were mounted on a transite table and comprised the bakeable portion of the vacuum system. A rotary vane oil-sealed fore pump and a three-stage water-cooled oil diffusion pump were used to evacuate the system to pressures below 10^{-7} Torr. Several vacuum gauges and an Octoil-S filled manometer furnished the system with the capability of operation over a broad range of measurable pressures. The oil manometer was applicable from 0.1 to 20 Torr, the RCA 1946 thermocouple gauge from 1 to 1000 m Torr, the RCA 1949 ionization gauge from 1 to 10^{-4} m Torr, and the Westinghouse 5966 Bayard-Alpert gauge at still lower pressures. The range of interest for this investigation was from 12.5 to 25.5 m Torr; therefore, an RCA 1946 thermocouple gauge, calibrated for xenon with a McLeod gauge, was used while filling the laser tubes.

In order to protect the system from oil vapors, copper foil and dry ice cold traps were employed to isolate the main manifold portion of the system. In the non-bakeable area all-metal Hoke valves were used except for the greased stopcock between the fore pump and the oil diffusion pump.

In order to safeguard the system in case of a loss of diffusion pump coolant or a vacuum failure, an electronic leak protect circuit was

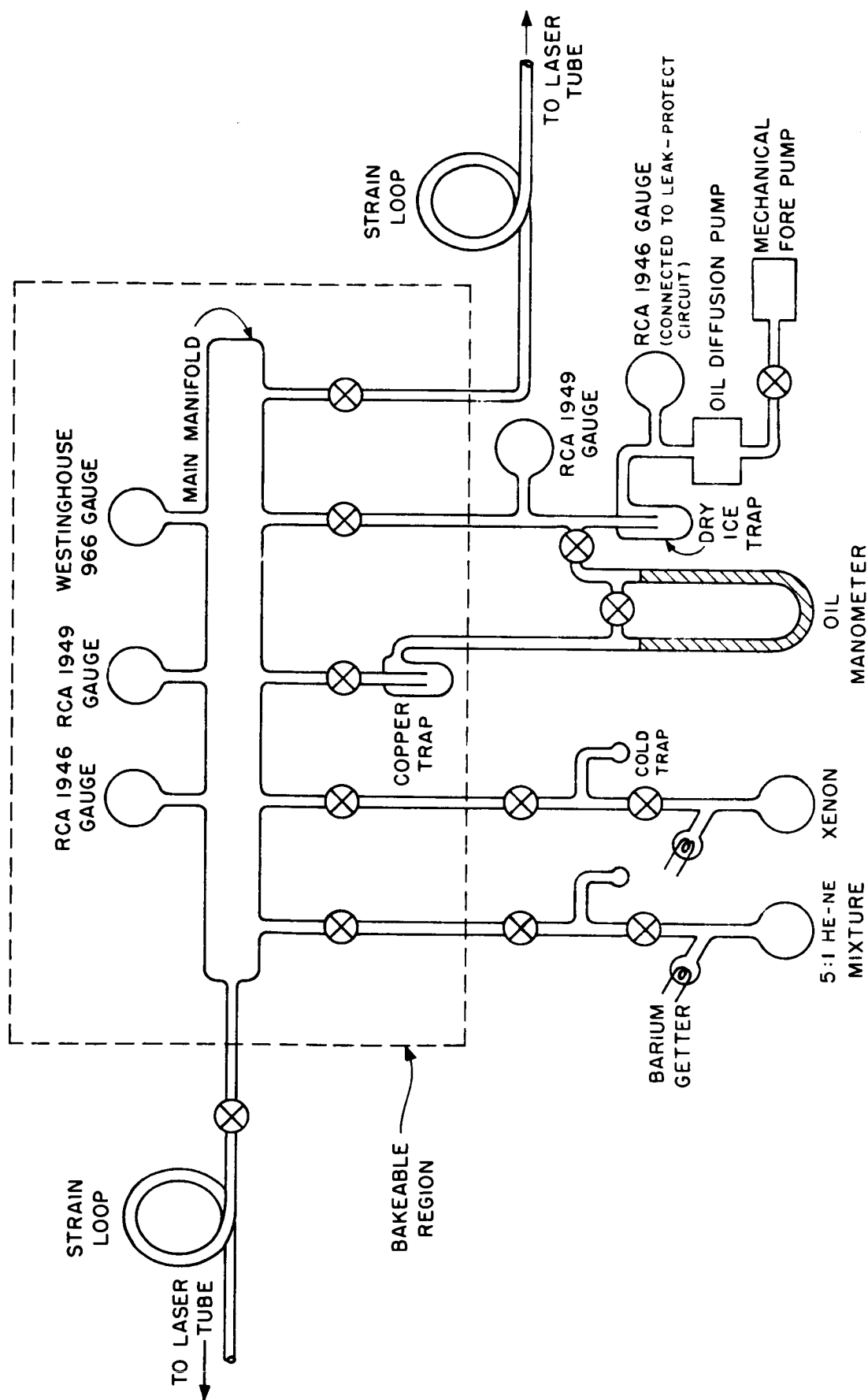


Figure 1. Vacuum and gas filling system.

incorporated into the vacuum system. Of the two gas bottles shown in Figure 1, only the xenon bottle was used in this experiment. Barium getters and cold traps were installed near the necks of the bottles to safeguard the gas purity.

Since the laser was operated at various xenon pressures, the laser tubes were permanently connected to the main manifold. A strain loop was provided to facilitate the necessary movement of the laser tubes during optical alignment.

3.2 Design of the Xenon Laser

The laser tube used in this experiment was of the conventional design.⁴² As shown in Figure 2, it was provided with quartz Brewster angle windows and employed an external mirror geometry. High-vacuum Torrseal epoxy was used to cement the quartz windows to the enlarged ends of the tube. In order to minimize the reflection loss for the plane parallel component of the laser radiation, the windows were oriented at the Brewster angle. Since the index of refraction of quartz at 3.51μ is 1.477, the Brewster angle, which equals the arc tan 1.477, is approximately 56° . Two spherical mirrors were employed: a 30 in. focal length aluminized mirror and a 2.15 m radius dielectric mirror coated for 99.9 per cent reflectance at 3.51μ .

The capillary portion of the tube consisted of a 35 cm length of 2 mm i.d., 1 mm wall quartz tubing. The narrow bore capillary provided increased gain for the 3.51μ transition and since the laser beam diameter and the capillary bore were of comparable size, for all practical purposes the entire plasma interacted with the laser radiation fields. The thin wall of the quartz tubing served to minimize the microwave power losses. However, in

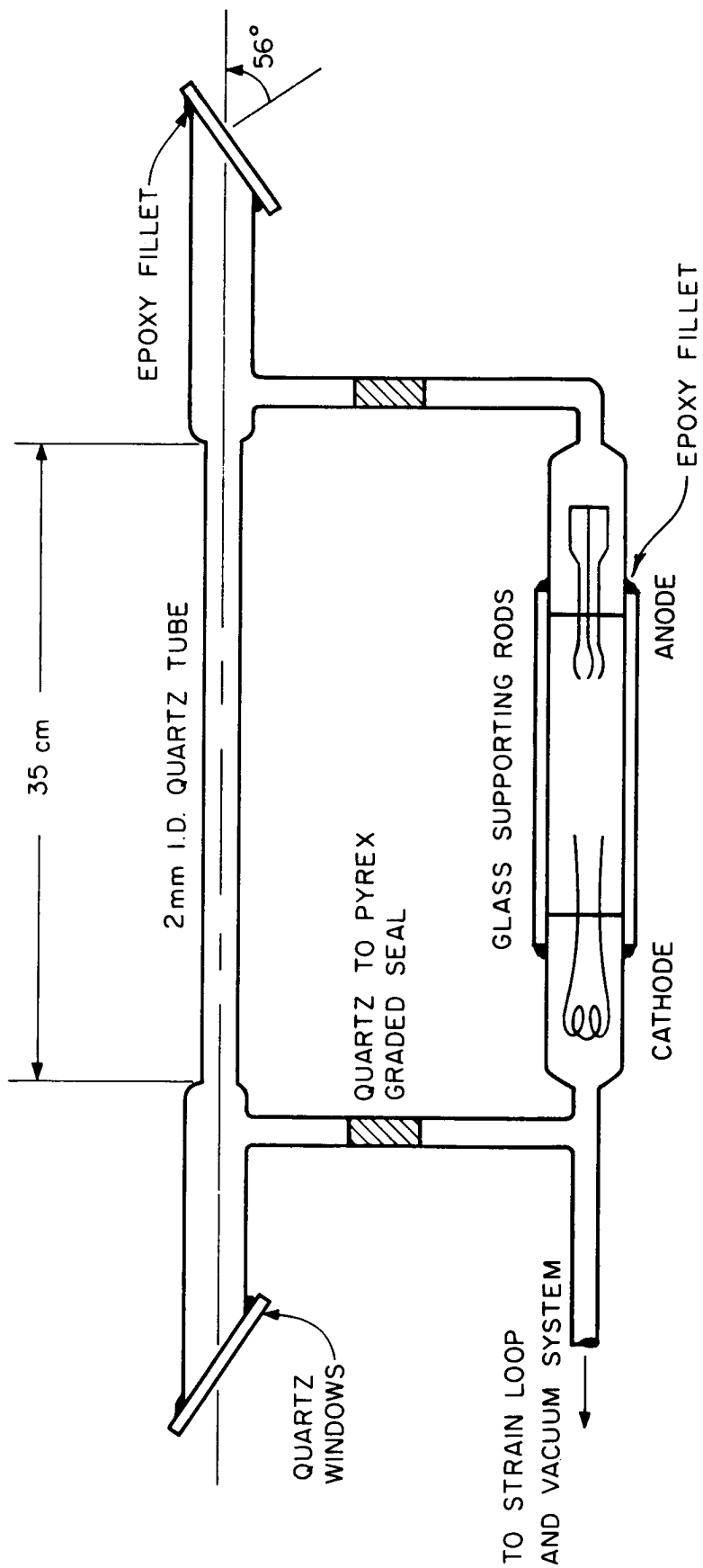


Figure 2. Design of xenon laser tube.

order to prevent the capillary portion of the discharge tube from bowing under the strain placed upon it by the weight of the electrodes, solid glass rods were epoxied between the two electrodes for rigidity. The laser was connected directly to the main manifold which provided a gas reservoir.

A hot cathode discharge was maintained using DC excitation, so that the active laser medium was the positive column of a xenon discharge. The cathode consisted of a lanthanum boride-coated, vacuum-fired, tantalum wire. The anode shown in Figure 2 was merely a conventional three-wire barium getter. Under some circumstances the laser tube was provided with two identical lanthanum boride-coated filaments in order to facilitate a reversal of the discharge polarity with respect to the xenon reservoir.

The discharge tube was supported on each end by means of a microscope stage which provided both vertical and horizontal degrees of freedom, necessary for the alignment of the discharge tube within the laser cavity. The mirror mounts were equipped with adjusting screws to aid in the mirror alignment and were provided with adjustable iris diaphragms to vary the mirror aperture.

The entire laser assembly was mounted upon a 14-foot steel I-beam for structural rigidity, as is shown in Figure 3. In order to minimize the effects of room vibration, shock absorbers were provided between the floor and the table and between tabletop and plywood board, and finally the I-beam was isolated from the plywood board by four partially inflated rubber inner tubes.

3.3 Electrical Circuitry for Monitoring Current Variations

Figure 4 schematically illustrates the circuitry used to supply power

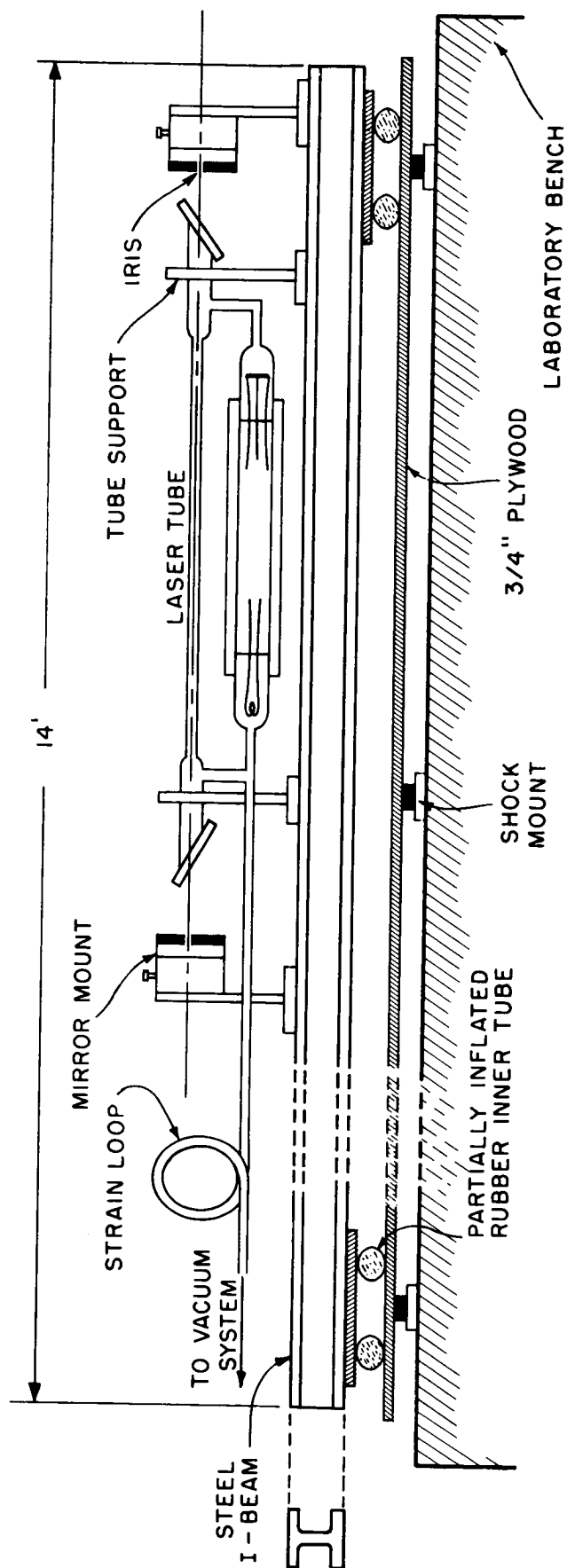


Figure 3. Overall view of the shock-mounted 3.51 μ laser assembly.

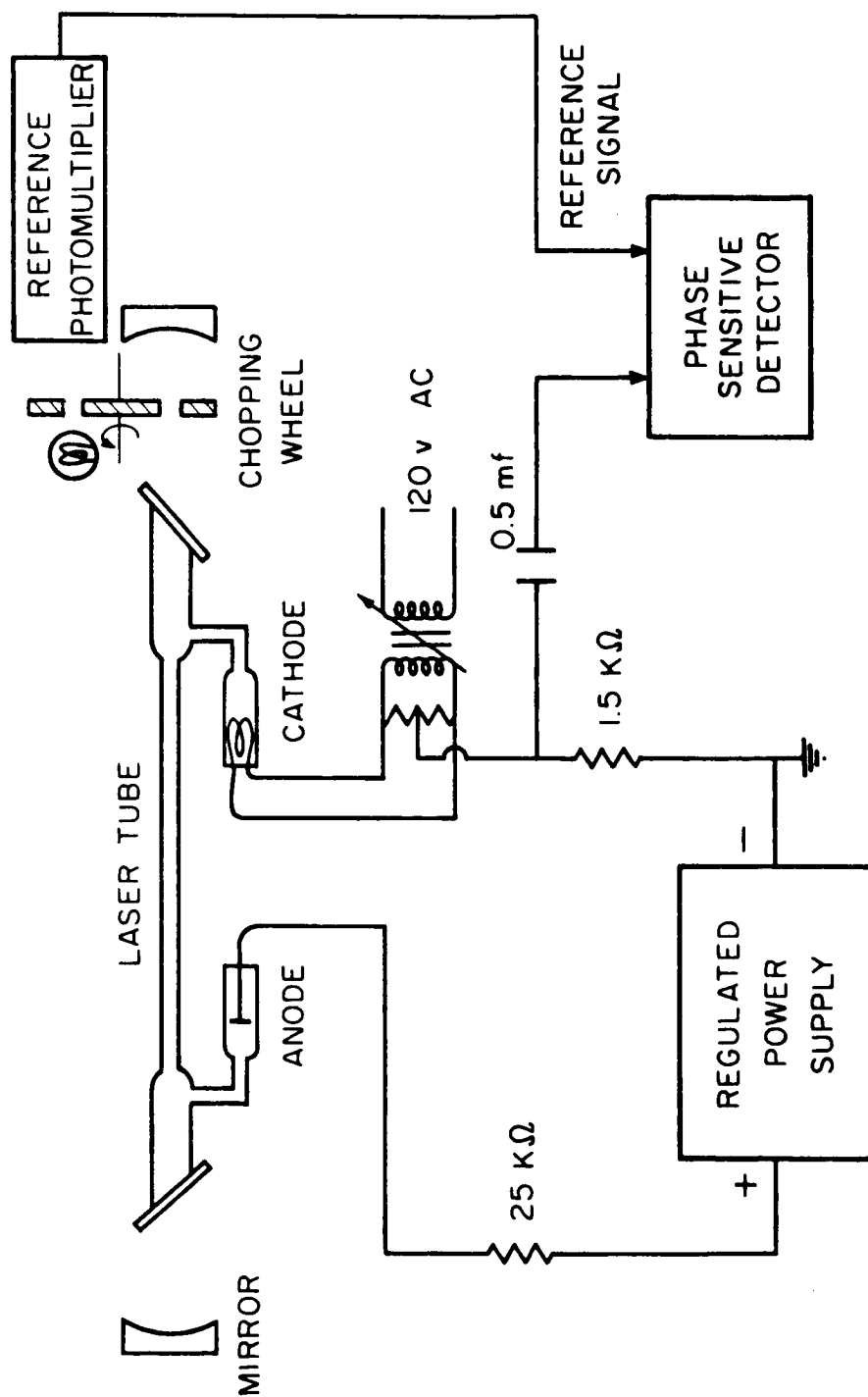


Figure 4. Schematic diagram of the circuit used to monitor laser-induced variations of the discharge current.

to the xenon discharge and to monitor the laser-induced current quenching. A $25\text{ k}\Omega$ load resistor was placed in series with a well regulated 0-5000 v, 0-100 ma DC power supply. A current of 8 amperes was passed through the filament of the cathode and a hum-bucking potentiometer was used to minimize the 60 cps ripple. In order to determine the influence of lasering upon the discharge current, the laser cavity was mechanically chopped at a 270 cps rate. Any current fluctuation was detected as a voltage change across the $1500\text{ }\Omega$ resistor in the cathode arm of the circuit. Since these voltage changes were typically $\sim 10^{-2}$ per cent, a 270 cps phase sensitive detector was employed, which was capable of measuring current changes as small as $\Delta I / I \sim 10^{-5}$ with reliability. A schematic circuit diagram of this detector is presented in Appendix C.

The 0.5 mfd capacitor served as a blocking capacitor for any DC current which might otherwise flow into the phase sensitive detector (PSD). The reference signal for the PSD was derived from the chopping wheel and was in phase synchronism with the chopped laser output. Having calibrated the meter deflection of the PSD with signals of known amplitude, the laser-induced current change was readily available.

3.4 Microwave Cavity Circuitry

The steady-state electron density was measured using a demountable C-band microwave cavity operating in the TM_{010} mode. The cylindrical cavity encircled a 13 mm length of plasma and had an inside diameter of 48 mm. The unfilled cavity had a resonant frequency of 4.942 kMc. When the discharge tube was placed along the cavity axis, a no-plasma cavity Q of ~ 2500 was obtained at a resonant frequency of 4.861 kMc.

The microwave cavity was mounted between four rods oriented parallel to the laser axis which permitted alignment of the discharge tube within the optical cavity without changing the position of the tube within the microwave cavity; furthermore, this means of support facilitated the movement of the microwave cavity to various positions along the tube. Thus, the plasma properties at various axial locations could be determined with good spatial resolution.

Care was taken to operate at microwave power levels sufficiently low ($\sim 10 \mu\text{w}$) to prevent any plasma heating. With the klystron pulsed on at a 270 cps rate, both the discharge current and the spontaneous emission were examined for 270 cps perturbations with a phase sensitive detector. Even at the maximum power levels used, the microwave cavity fields did not disturb the discharge within detectable limits.

During the measurement of the steady-state electron density, the chopping wheel was inoperative and the laser mirrors were blocked to prevent lasing. An FXR Test Oscillator was swept in frequency through the cavity passband by applying a periodic sawtooth modulation upon the reflector of the klystron. The shift in cavity frequency due to the plasma was measured with a conventional cylindrical cavity wavemeter over a DC current range of 0 to 100 ma for xenon reservoir pressures of 12.5, 18.5 and 25.5 m Torr.

To relate the measured resonant frequency shift of the microwave cavity to the electron density in the portion of the discharge within this cavity, a computerized solution of the fields within the TM_{010} cavity was required. The computer was programmed to treat the particular case of an inhomogeneous plasma situated in a cylindrical glass tube, which was oriented along the

axis of a TM_{010} microwave cavity. The derivation is presented in Appendix A and the tabulated values of electron density versus frequency shift appear in Appendix B.

The perturbation in electron number density due to lasering resulted in periodic shifts of the resonance frequency of the microwave cavity. These were much too small to be measured reliably with a conventional wave-meter. The development of a more sensitive diagnostic technique was required. The apparatus employed in this measurement is illustrated schematically in Figure 5 and essentially combines the sensitivity of synchronous detection with the spatial resolution and inherent accuracy of the microwave cavity technique. Without elaborate attempts to optimize the sensitivity of this system, changes in electron density as small as $\Delta n_e / n_e \approx 3 \times 10^{-5}$ were recorded, well within the requirements of this application.

With the test oscillator operating continuously and swept in frequency through the cavity passband, the crystal detector sampling the cavity power yields an output voltage which is a Lorentzian function of the input frequency, centered about the microwave cavity resonance as illustrated in curve A of Figure 6. However, a laser induced change in electron density shifts this resonance characteristic to either higher or lower frequencies and thereby changes the crystal detector voltage when the test oscillator is operating at a fixed frequency.

The crystal detector is Q times more sensitive to a given percentage shift in resonant frequency than to an equal percentage change in cavity Q .¹⁰ Thus, a variation in electron density and the resultant shift in the resonance characteristic produces a change in detector voltage that dominates

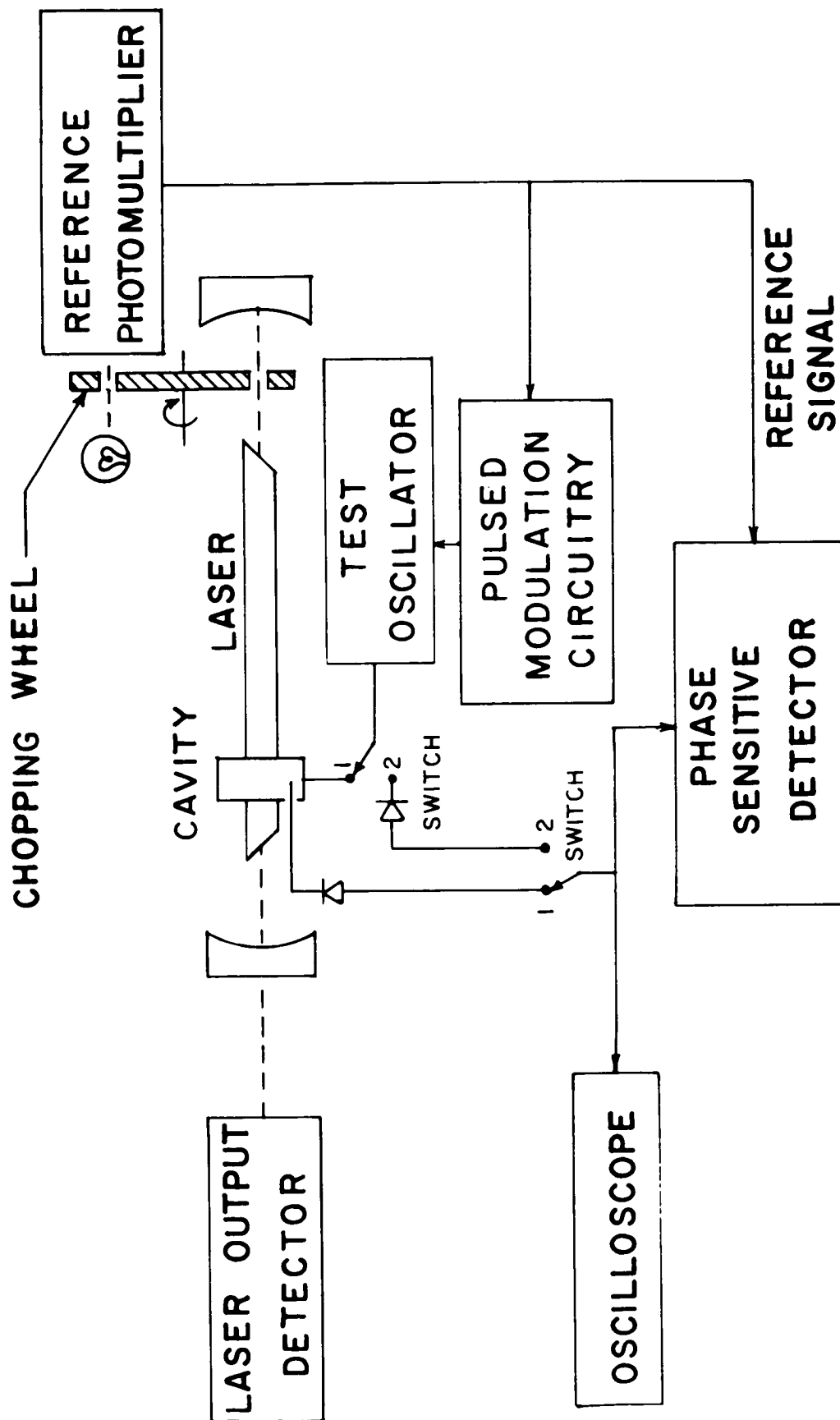


Figure 5. Schematic diagram of the microwave cavity apparatus used to measure laser-induced electron density perturbations.

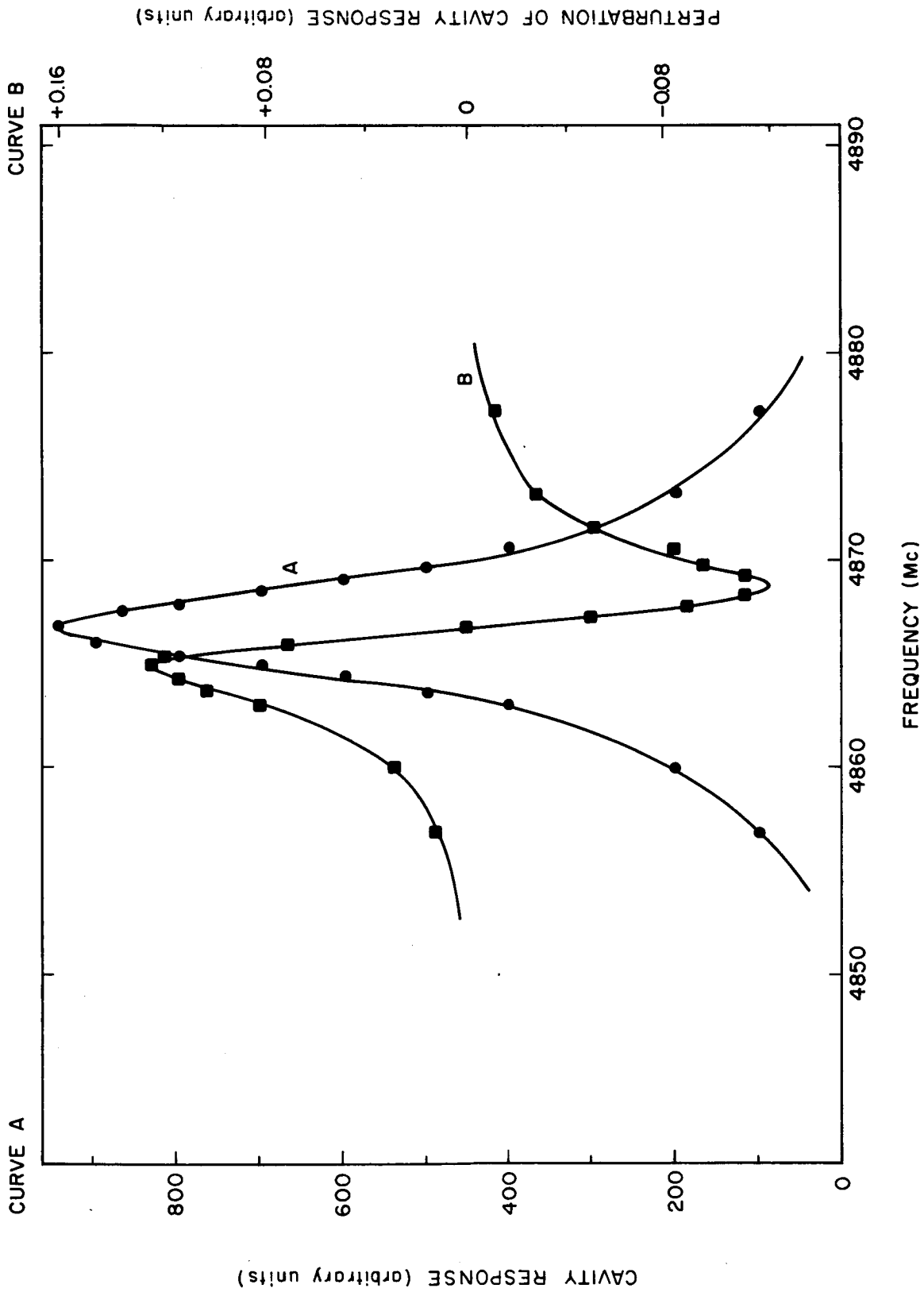


Figure 6. TM_{010} microwave cavity resonance characteristics for the cathode end of the discharge at a xenon pressure of 12.5 m Torr. Curve A, steady-state cavity response for the non-lasing plasma; Curve B, perturbation of the cavity response induced by lasing.

over contributions from Q variations. The phase sensitive detector, therefore, essentially "sees" only those variations caused by electron density changes. Under such conditions the phase sensitive detector indication is an odd function of the microwave input frequency. Curve B of Figure 6 illustrates that these conditions exist at the cathode for a current of 50 ma and a pressure of 12.5 m Torr.

All experimental points reported here have been recorded under similar conditions. The effects of Q changes are evident only where the electron density variations are small or where the cavity Q is severely degraded. Under these circumstances the sign of Δn_e and ΔQ can still be inferred unambiguously, since for a pure frequency shift, the phase sensitive detector indication is an odd function of the microwave input frequency, whereas an even function exists if only the cavity Q changes. An example of a case in which the effects of both Δn_e and ΔQ can be seen is illustrated by Figure 7. At a DC discharge current of 50 ma and for a pressure of 25.5 m Torr, the Q of the cavity at the center of the tube is significantly degraded, as illustrated by Curve A, due to the combined effects of large steady-state electron densities and electron collisions with the neutrals and the ions. Curve B, which depicts the laser-induced perturbation of the cavity fields, is clearly the superposition of odd and even functions of the microwave frequency. In this particular case, lasering increases the cavity Q and causes the cavity resonance to shift to higher frequencies, which is indicative of a positive Δn_e .

If the 270 cps shift in the cavity resonance characteristic is exactly compensated by an equal and opposite shift in the microwave source frequency,

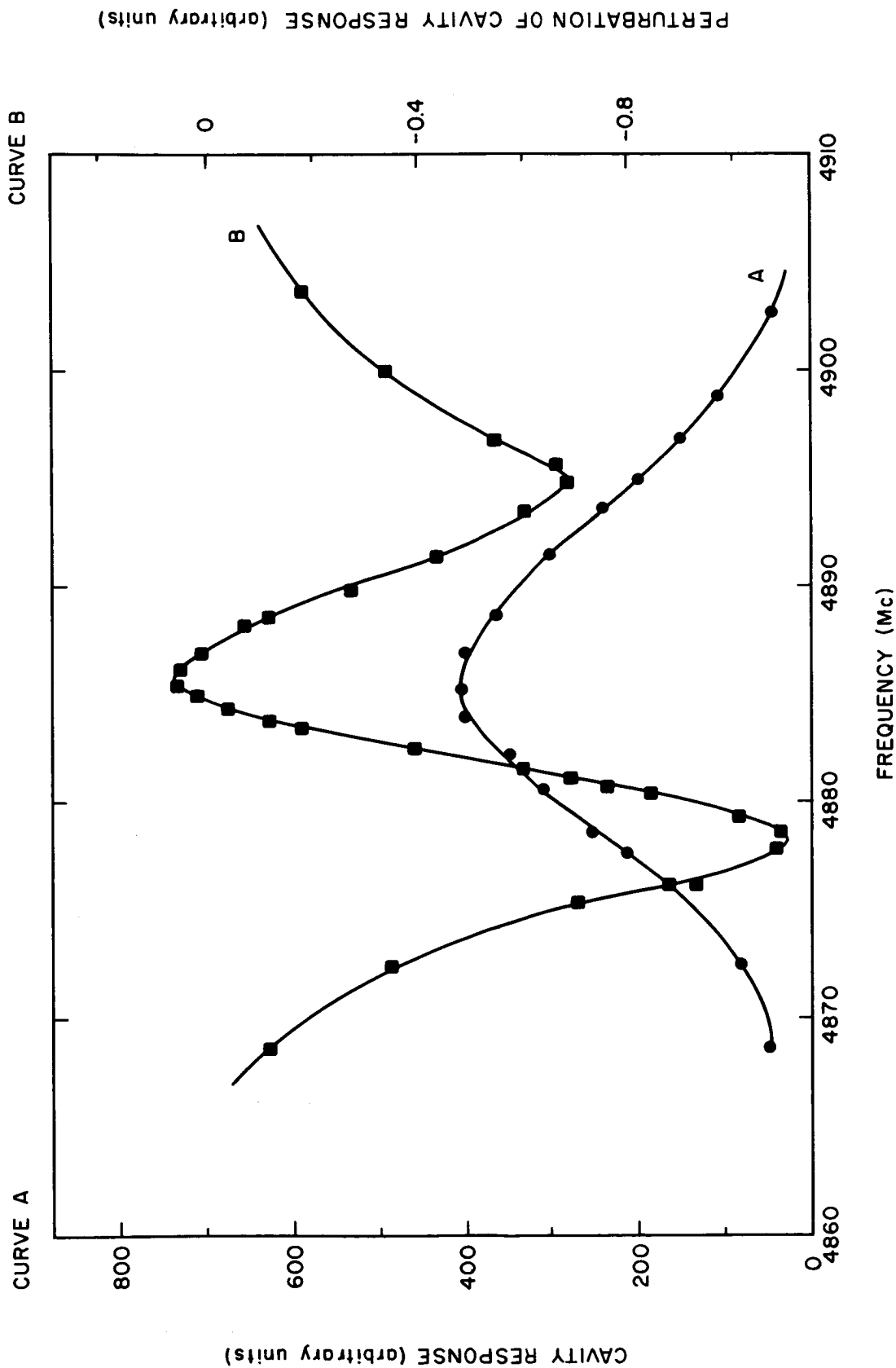


Figure 7. TM₀₁₀ microwave cavity resonance characteristics for the center of the discharge at a xenon pressure of 25.5 m Torr. Curve A, steady-state cavity response for the non-lasing plasma; Curve B, perturbation of the cavity response induced by laser.

no net change in crystal voltage occurs. The resultant null in the phase sensitive detector voltage at the proper frequency modulation constitutes a very accurate method of determining the microwave cavity resonance shift by comparing it to a measurable microwave source frequency shift. This is accomplished by modulating the klystron repeller voltage with a 270 cps square wave of known amplitude, synchronized to the chopped laser output. As shown in Figure 5, the reference signal triggers a voltage pulse network producing a square wave of adjustable amplitude. This pulsed modulation circuitry consists of a Tek 162 waveform generator and a Tek 161 pulse generator in tandem. With both switches in position 1, an appropriate square wave level can be found to produce the desired null.

To insure that the microwave power level is not also amplitude modulated at a 270 cps rate and, hence, spuriously contributing to the synchronous detector reading, the switches are placed in position 2 and the steady-state reflector voltage is adjusted for a phase sensitive detector null. A reflector voltage can always be found for which the klystron power level is equal for the two slightly displaced frequencies. For the klystron used in this experiment, a frequency change of 180 cps per millivolt of reflector voltage was measured. Thus, a simple measurement of the square wave amplitude required for complete cavity frequency compensation was sufficient to determine the very small laser-induced changes in electron density with great precision.

3.5 Plasma Emissivity Measurements

In order to determine the steady-state electron temperature and its laser-induced variations, it was necessary to measure the emissivity and

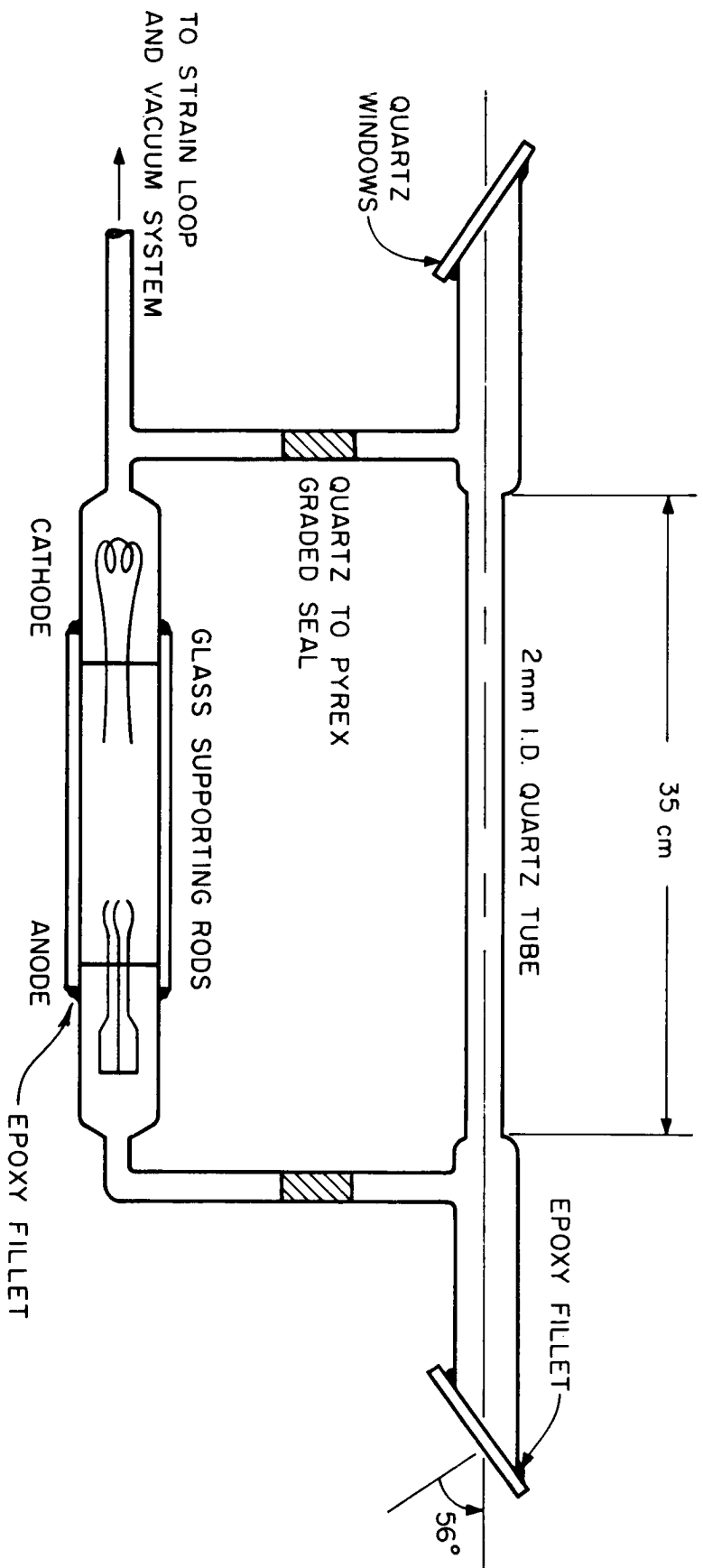


Figure 2. Design of xenon laser tube.

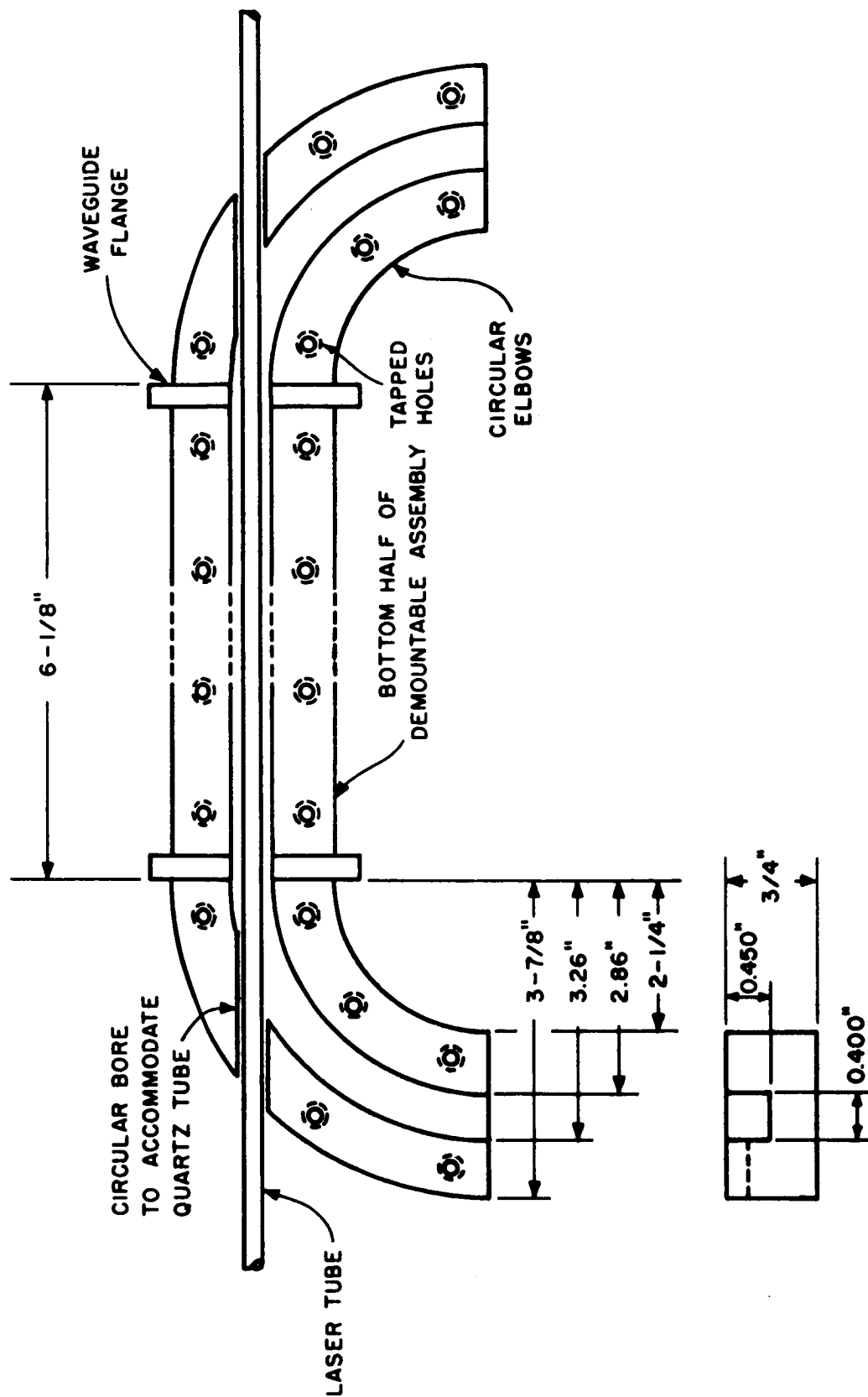


Figure 8. Bottom half of demountable section of X-band waveguide, showing position of laser tube within the guide assembly.

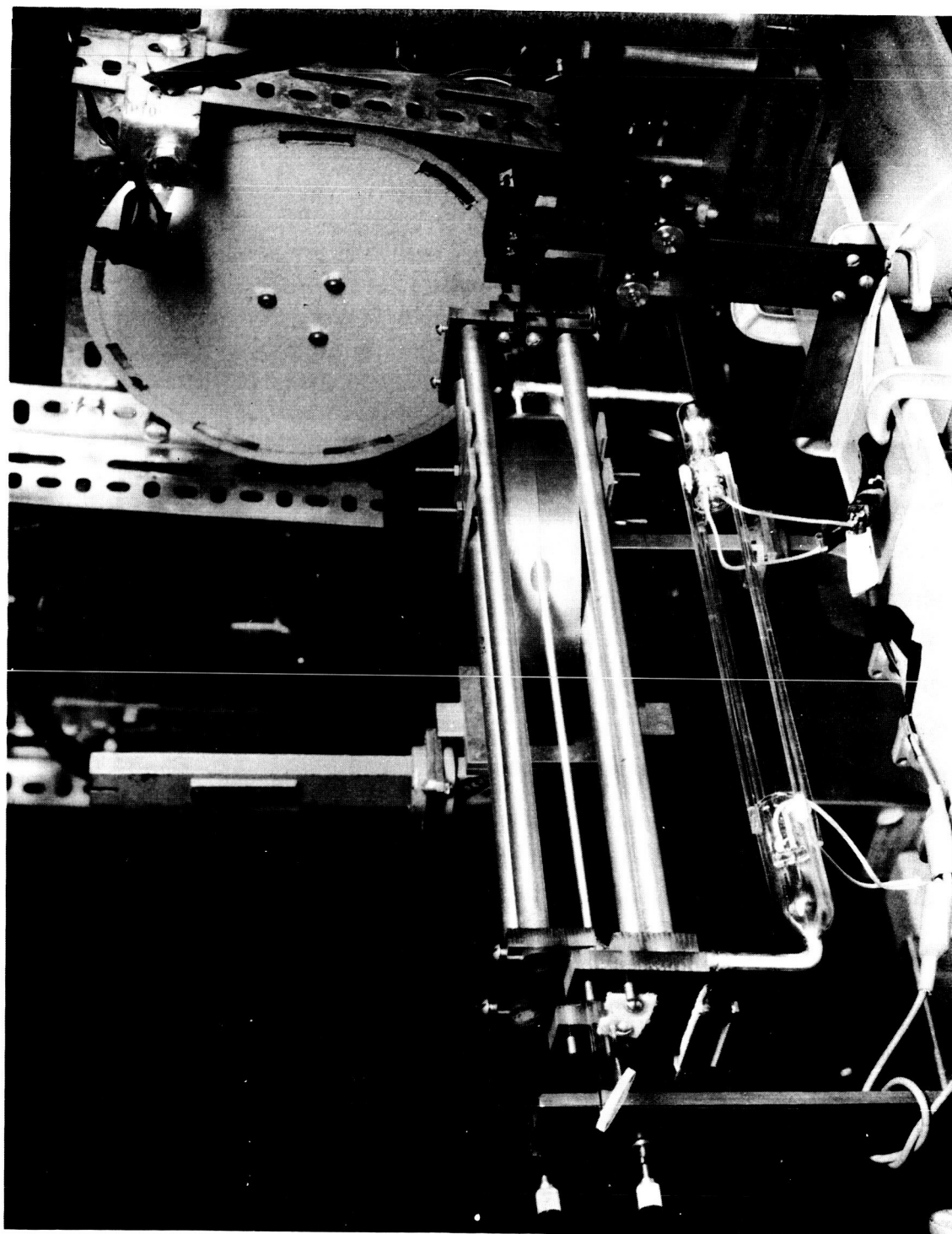


Figure 9. Assembled view of the demountable waveguide section and the associated supporting structure.

The apparatus used in the plasma emissivity studies is illustrated schematically in Figure 10. To determine the absorptivity of the steady-state plasma, the microwave switch is placed in position 1 and the mirrors are covered to prevent lasering. With the chopping wheel operative, the reference photomultiplier supplies a 270 cps square wave signal to an electronic pulsing system comprised of a Tek 162 waveform generator and a Tek 161 pulse generator in tandem. A 270 cps square wave was placed upon the reflector of an X-13 klystron in order to operate it in a pulsed "on" mode at a frequency of 8684 Mc.

To insure that the microwave power was not disturbing the plasma, both the discharge current and the spontaneous light emission were monitored with a phase sensitive detector for any microwave dependent variations. The voltage standing wave ratio was measured employing a conventional X-band slotted line and a calibrated crystal detector. Since the experiment was performed at very low power levels, high-gain AC amplifiers were used. This required that the klystron be turned on and off periodically. The ratio of the standing wave maximum -to-minimum was measured with a Hewlett-Packard precision attenuator. Standing wave ratios resulting from a double traversal of the plasma were observed by the insertion of a sliding short at the end of the demountable section of the waveguide.

The effects of lasering upon the emissivity of the plasma were studied with only minor modification of the microwave system. The slotted line was now replaced by a four-port ferrite circulator; the input power entered port 1, and exited port 2 toward the plasma; the signal leaving the plasma after a double traversal entered port 2 and was detected at port 3 by a crystal

detector; port 4 was terminated in a matched load. With the klystron now operating c.w. at 8684 Mc, the laser mirrors uncovered and the chopping wheel operative, the crystal detector output at port 3 was sent directly into the phase sensitive detector. Laser-induced changes in the plasma emissivity of $\Delta\epsilon/\epsilon \approx 5 \times 10^{-4}$ were readily available from the calibrated meter deflection of the synchronous detector. As in the steady-state case, these measurements were performed over a current range from 0-100 ma and at pressures of 12.5, 18.5 and 25.5 m Torr.

3.6 Microwave Noise Power Measurements

The schematic diagram of Figure 10 with the microwave switch in position 2 shows the experimental apparatus used to measure the noise power radiated by the steady-state plasma. During the microwave noise measurement, a standard noise source was used for comparison purposes, and both mirrors were covered to prevent lasering. Both the signal from the standard noise source and that radiated from the test plasma were chopped at a 270 cps rate. The signal from the standard noise source was 180° out of phase with that of the plasma and its amplitude could be adjusted using a precision attenuator. Both signals entered the same arm of a balanced mixer via different entrance ports of a calibrated 3 db direction coupler. The plasma signal suffered a 3.1 db attenuation and the standard noise source signal a 3.5 db attenuation upon passing through the directional coupler. The superimposed signals were heterodyned in frequency with an X-13 local oscillator operating at a frequency of 8624 Mc, which is 60 Mc below the frequency at which the emissivity measurements were taken. The beat frequency was amplified by a General Radio 60 Mc i.f. strip and sent into a phase sensitive detector. When the amplitude

of the signal from the standard noise source was adjusted for a null PSD meter deflection, the two signals leaving the directional coupler were of equal magnitude.

The 270 cps modulation of the noise radiated from the test plasma was made possible through the use of a Philco 1N3093 crystal diode switch. When properly biased, this diode could be operated in either an "open" or "closed" mode. A negative 11-volt bias resulted in a 33 db mismatch whereas a positive 2.5 v bias introduced only a 2.0 db attenuation at a frequency of 8684 Mc. The 270 cps chopped signal from the reference photomultiplier served several functions; not only did it provide a reference signal for the phase sensitive detector, but it also controlled the switching mode of the crystal diode switch and the pulsed operation of the standard noise source. A schematic of the crystal diode biasing circuit can be found in Appendix C. When the diode switch was operated in the "closed" mode, it acted as an additional source of microwave noise and had to be corrected for in the calculation of the plasma radiation temperature.

Measurements of the change in radiated noise power induced by lasering were made by slightly modifying the microwave circuit shown in Figure 10. The 3 db directional coupler and the crystal diode switch were replaced by a calibrated 10 db directional coupler. The signal from the plasma arm was sent into the low-loss arm of the directional coupler. With the laser mirrors uncovered and the optical cavity mechanically chopped at a 270 cps rate, the noise power radiated by the plasma is weakly modulated at a rate synchronized with the chopped laser output. Once again the amplitude of the chopped signal is compared with a similarly modulated signal from the standard noise source

by means of the phase sensitive detector. Changes as small as

$\Delta T_{\text{rad}}/T_{\text{rad}} \approx 5 \times 10^{-4}$ were obtainable. These measurements were also carried out over a current range of 0-100 ma at pressures of 12.5, 18.5 and 25.5 m Torr.

Figure 11 is a photograph of the microwave apparatus employed in the emissivity and noise power measurements.

3.7 Spectroscopic System

With the chopping wheel inoperative the steady-state intensity of the spontaneous emission radiated perpendicular to the axis of the tube (sidelight) was monitored using a Hilger-Watts grating monochromator in conjunction with a photomultiplier. Depending upon the wavelength of the transition involved, either an RCA 7102 or a 931A photomultiplier was used. In order to determine the spatial dependence of the sidelight intensity, measurements were taken at various points along the discharge tube with the aid of a quartz fiber light pipe.

The apparatus employed for investigating the effects of lasering upon the excited state populations in xenon is illustrated in Figure 12. Normalized changes in sidelight intensity of 10^{-4} were obtained using phase sensitive detection. For optically thin portions of the discharge, the intensity of the spontaneous emission is proportional to the population of the upper level of the transition.⁴³ Therefore, the sidelight is a convenient means of monitoring the population of the excited atoms.

The 3.51μ ($5 d_{33} \rightarrow 6 p_{22}$) laser output was monitored using a Hilger prism spectrometer in conjunction with an indium antimonide (InSb) photovoltaic cell operating at 77°K . The output of the InSb detector was fed into a transistorized low-noise amplifier whose circuit is presented in Appendix C.

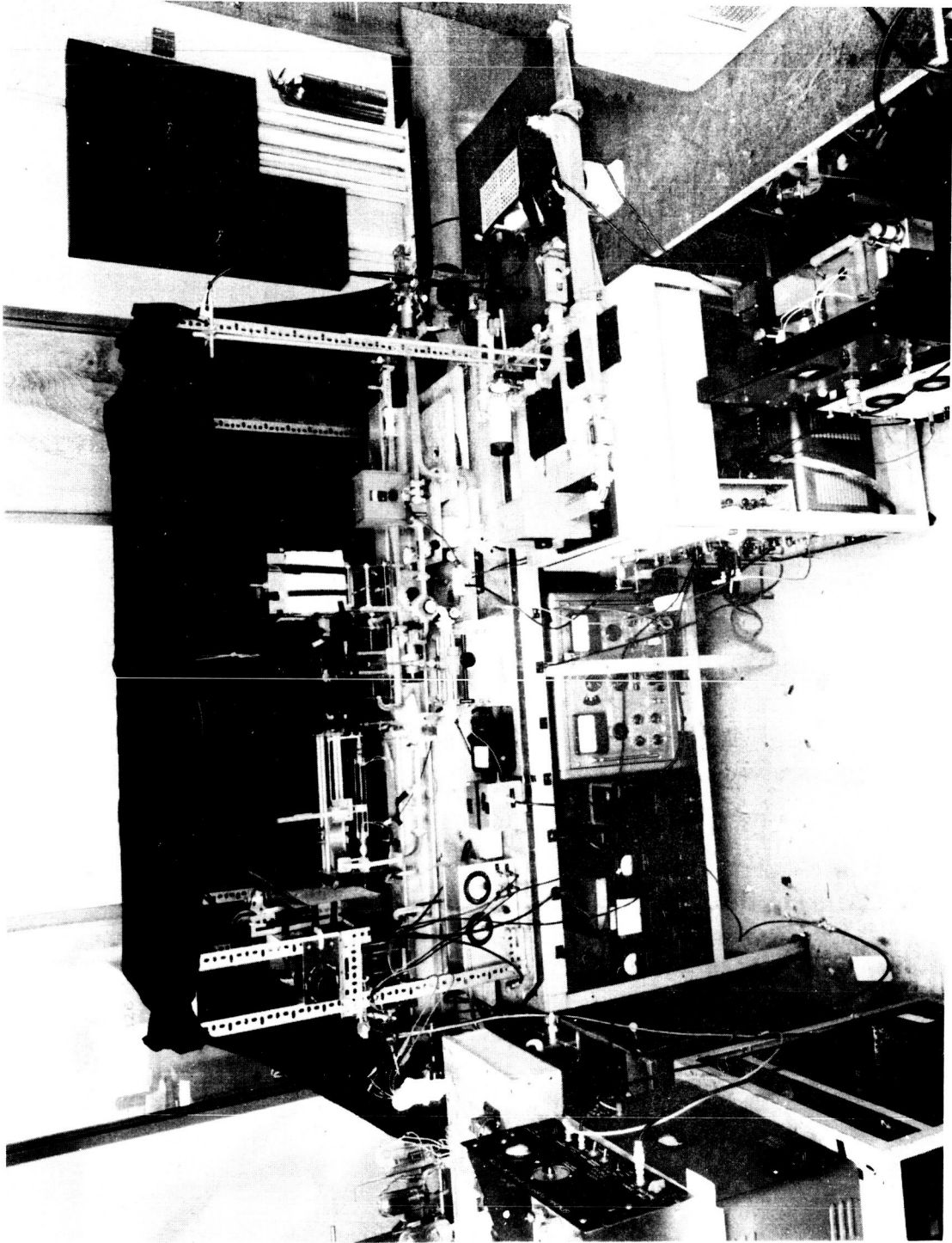


Figure 11. Photograph of experimental system used to measure the electron temperature of the xenon discharge.

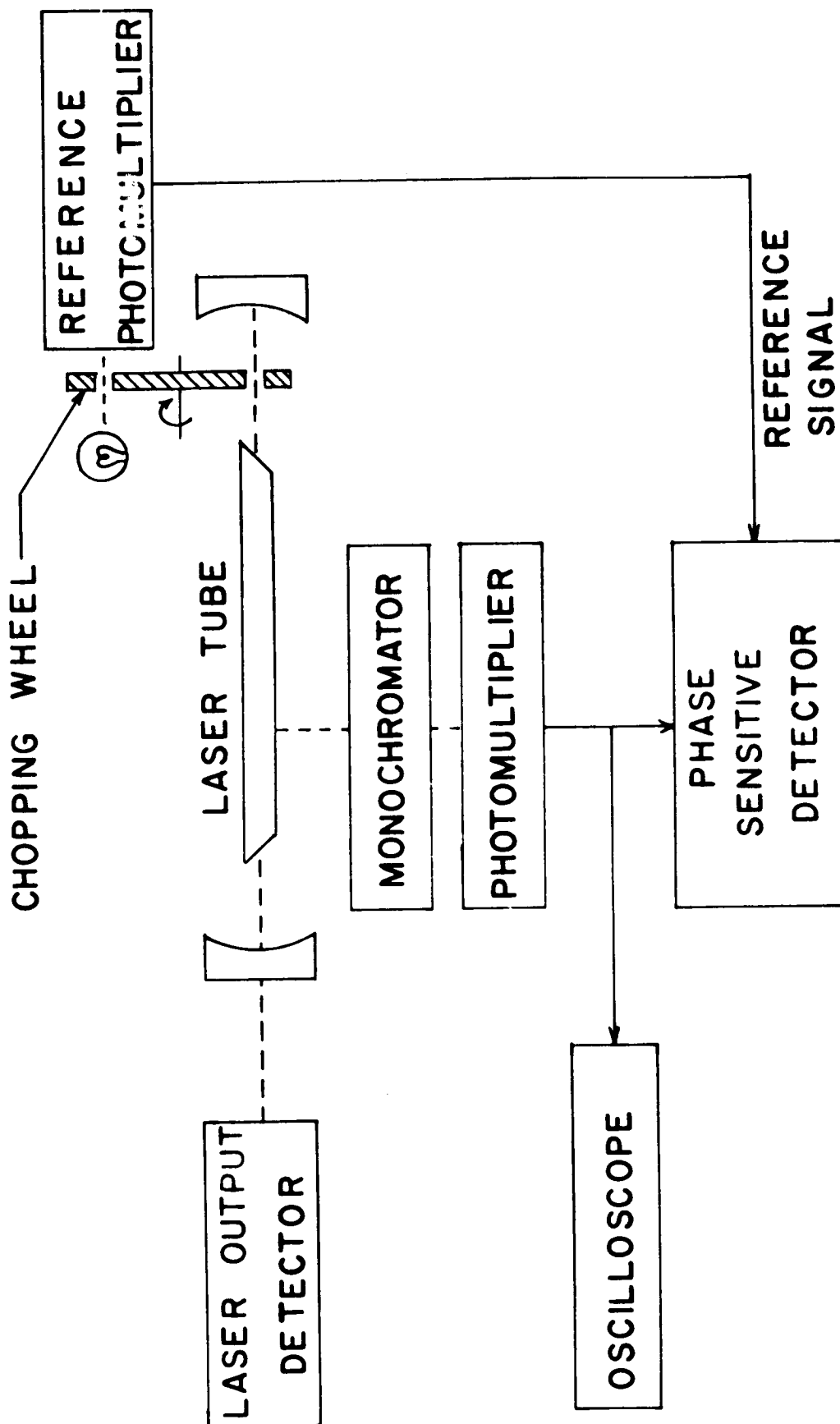


Figure 12. Schematic diagram of the spectroscopic apparatus used to monitor the laser-induced intensity variations of the spontaneous emission.

IV. EXPERIMENTAL OBSERVATIONS AND RESULTS

In this chapter the observations and results of a broad range of microwave, spectroscopic and electronic experiments are discussed in detail. The material is presented in three parts. The first deals with the steady-state properties of the xenon laser discharge. The current, spatial and pressure dependence of such quantities as electron density, electron temperature, neutral gas density, the population of atoms in the various excited states and local population inversion of the laser transition are presented over a current range of 0 to 100 ma and at pressures of 12.5, 18.5 and 25.5 m Torr.

The following section deals with effects of lasering upon the electron gas parameters (current, density and temperature). On the basis of the perturbation of the electron gas, a model is proposed to account for the observed current quenching and the related variations in the electron density and temperature. The model suggests that cumulative (stepwise) processes within the lasering discharge are of considerable importance. The decreased electron density and the corresponding increase in electron temperature at low currents is attributed primarily to decreased electronic ionization from the $5d_{3/2}$ state during lasering. On the other hand, it is suggested that increased ionization from the xenon metastables during lasering becomes more important at higher currents and accounts for an enhanced electron density and a temperature decrease.

In the final section of this chapter spectroscopic observations of the laser-induced sidelight variations are presented as confirming evidence of the proposed model. Excitation from the $6s$ metastables is shown to become

increasingly more important as the steady-state electron and metastable densities increase. In fact, it is demonstrated that in the region near the anode, such processes can completely destroy the local inverted population.

4.1 Characteristics of the Xenon Laser Discharge

The pure xenon laser discharges studied experimentally were produced in a narrow-bore capillary over a reservoir pressure range of 12.5 to 25.5 m Torr. Under such conditions a longitudinal gradient of the discharge properties was established due to electrophoretic effects within the inter-electrode volume. This variation was quite apparent from a visual examination of the color of the discharge, which exhibited a distinct gradation along the tube. Spectral line intensity measurements shown in Figure 13 experimentally confirmed that an axial inhomogeneity was established in the discharge. At all four currents the 9923 \AA transition exhibited a marked increase in sidelight intensity toward the anode, indicating an increase in the $6 p_{22}$ population in this region. The contributions to the laser output are directly dependent upon the local population inversion in the xenon discharge. A thorough understanding of this axial gradient is essential in order to identify the mechanisms responsible for lasering and to determine the effects of the optical laser fields upon the plasma medium.

Spatially resolved electron density measurements were obtained as a function of the discharge current, using a demountable TM_{010} microwave cavity as was discussed in the previous chapter. Figure 14(a) shows that for each of the three xenon pressures, a longitudinal gradient in the electron density was established. For constant discharge current, the electron

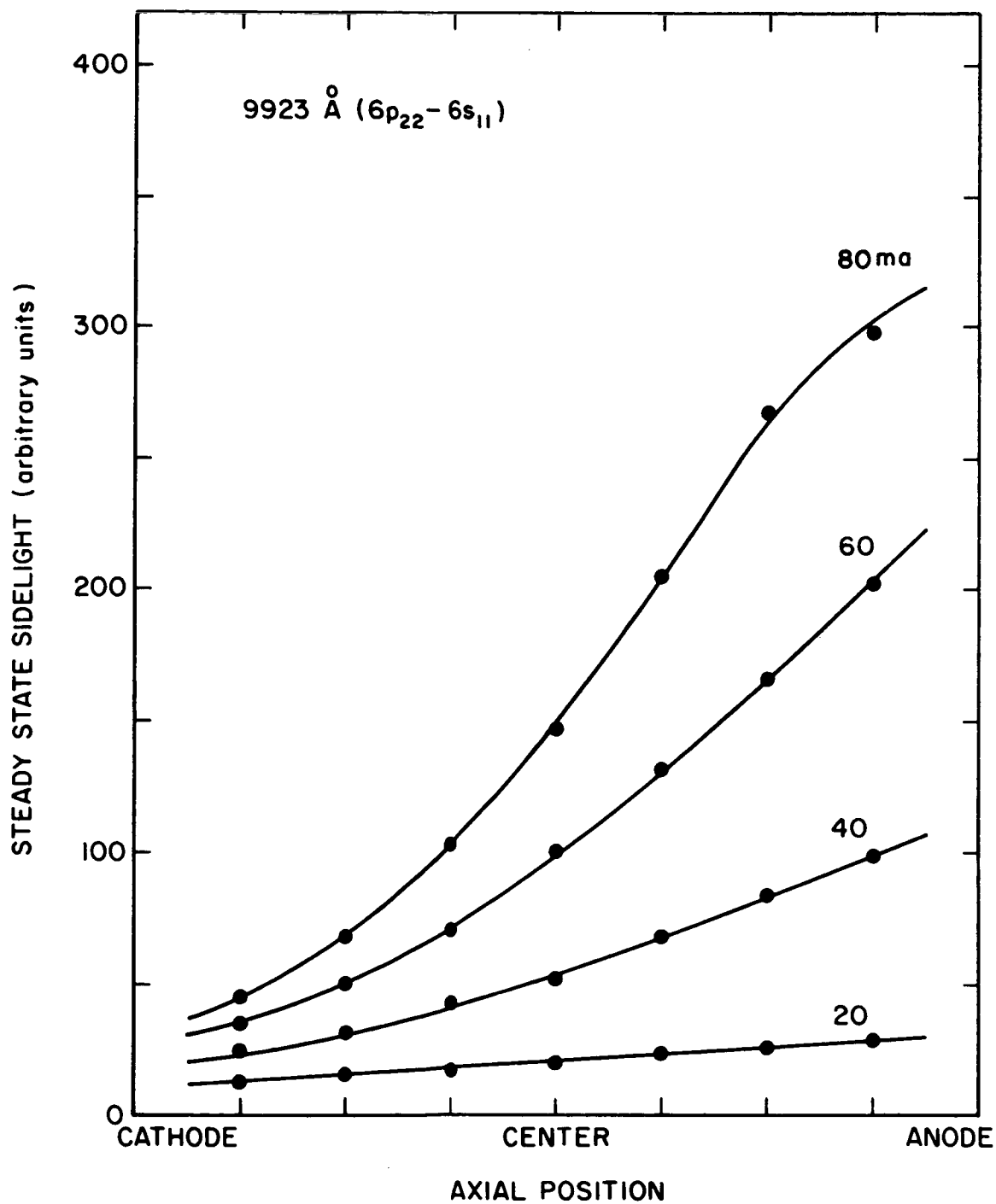


Figure 13. Spatial dependence of the steady-state 9923 Å spontaneous emission intensity at various values of discharge current at 12.5 m Torr.

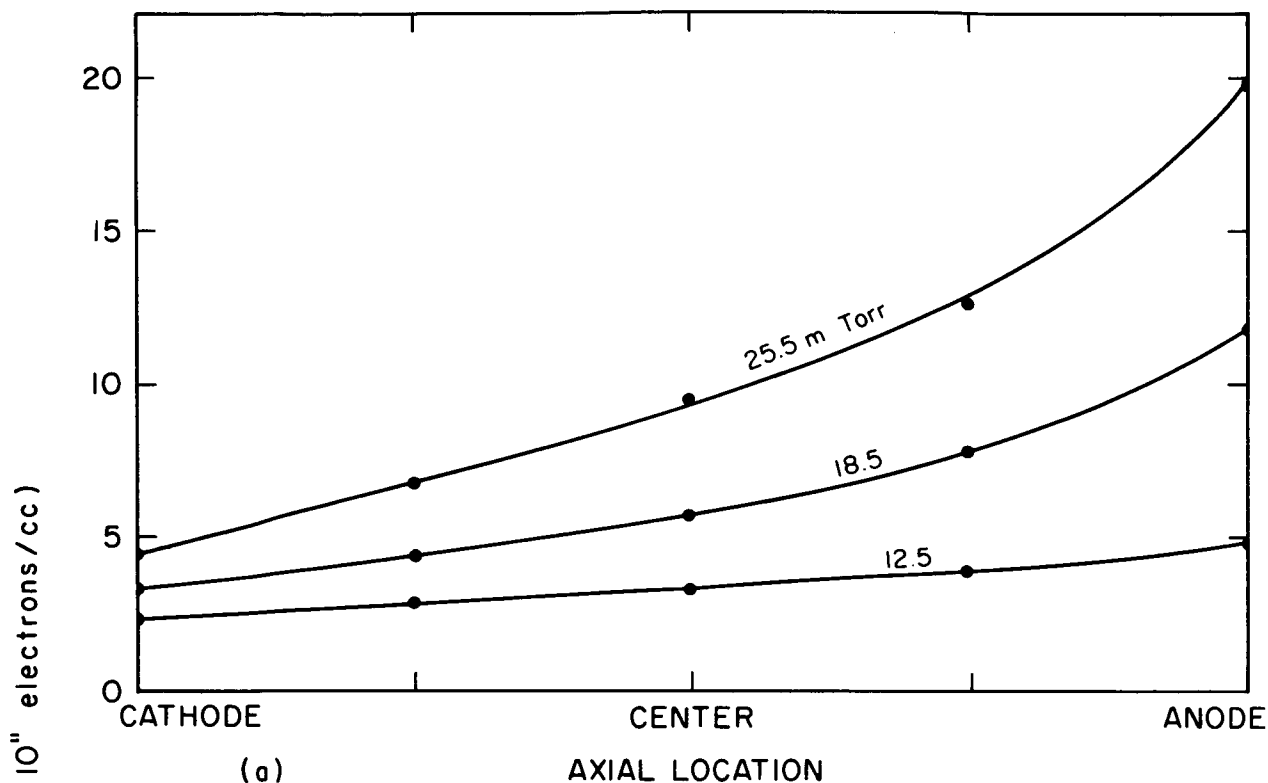


Figure 14(a). Spatial dependence of the steady-state electron density at a discharge current of 50 ma for various xenon pressures.

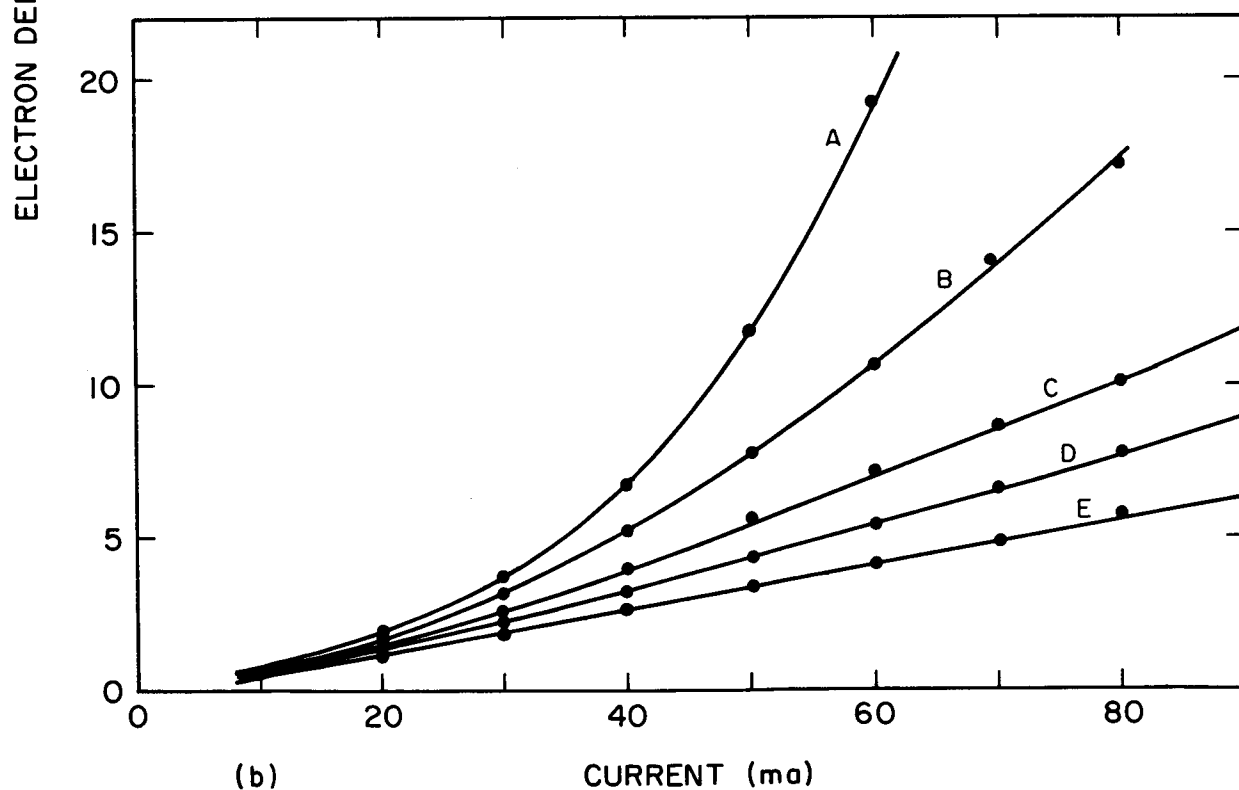


Figure 14(b). Current dependence of the steady-state electron density at a xenon pressure of 18.5 m Torr at various axial locations. Curve A, anode; Curve B, between anode and center; Curve C, center; Curve D, between center and cathode; Curve E, cathode.

concentration is greatest at the anode end of the capillary. This gradient appears linear at the cathode, but departs significantly from linearity and increases more rapidly toward the anode. Similar variations were observed for discharge currents other than 50 ma, with measured axial electron densities generally lying between $8 \times 10^{10} \text{ cm}^{-3}$ and $2 \times 10^{12} \text{ cm}^{-3}$.

In Figure 14(a) increasing the xenon pressure yields an increased electron density for the same current and axial position. This is probably because a larger number of neutral atoms are available for ionization at higher pressures. Therefore, it may be inferred that the observed axial gradients in electron density are accompanied by similar gradients in neutral xenon pressure. Such anode-directed inhomogeneities in electron and neutral concentrations have been reported by other investigators^{44,45} as well and are a consequence of a net electronic momentum transfer to the neutral gas.

Langmuir⁴⁶ and Druyvesteyn⁴⁷ have theoretically analyzed such gradients in a positive column of a DC discharge and have attributed them to electrophoretic phenomena. More recently Leiby⁴⁸ has suggested the existence of additional volume forces which can contribute to an anode-directed neutral gas flow.

Since both electrons and ions experience equal and opposite forces due to the applied electric field, the time rate of momentum increase must be equal but opposite in sign for each species, i.e.,

$$\vec{F}_{\pm} = q_{\pm} \vec{E} = \frac{d}{dt} (\vec{p}_{\pm}) \quad (4-1)$$

The rate at which momentum is transferred to the neutral gas by electronic and ionic elastic collisions is related to their respective neutral collision frequencies ν_{\pm} .

$$\frac{dp_{\pm}}{dt} = G_{\pm} p_{\pm} \nu_{\pm} \quad (4-2)$$

G_{\pm} is the proportion of the momentum which is transferred to a neutral per collision and p_j is just the linear momentum of the j^{th} constituent of the plasma. The collision frequency can be expressed as the product of Q_{\pm} , the cross section for momentum transfer, $v_{\pm \text{ rel.}}$, the relative velocity of the collision partners and N_n , the neutral density. Therefore,

$$\frac{dp_{\pm}}{dt} = G_{\pm} p_{\pm} N_n Q_{\pm} v_{\pm \text{ rel.}} \quad (4-3)$$

which indicates that if Q_{\pm} increases with p_{\pm} , the rate at which the neutrals are receiving momentum from the charged species of the plasma increases faster than p_{\pm} .

In the steady state, a condition must be reached for which the momentum loss rate and the momentum gain rate are equal for each species. Since it has already been established that the rate of momentum gain from the applied field is the same for both electrons and ions, then the rate at which they lose momentum must also be equal. In an infinite plasma, the main momentum loss mechanism is that involving the neutrals. Therefore, the electrons and ions collisionally transfer momentum to the neutral gas at the same rate, so that neither species delivers more momentum to the neutrals than the other.

However, in a closed tube, this balance can be disrupted by the preferential loss of ion momentum to the walls.

Electronic wall potentials tend to equalize the rates at which electrons and ions arrive at the wall, and since the mass of the ion is vastly greater than that of the electron, more axial momentum is lost to the walls by the ions than by the electrons. As a consequence of this inequality in wall loss rates, a net axial momentum is imparted to the neutral gas by the electrons. The resultant neutral gas flow towards the anode, designated⁴⁸ as "anaphoresis," establishes an anode-directed pressure gradient in discharge tubes which are constructed with no gas return paths. Upon reversal of the discharge polarity, it was observed that measured electron densities were still greater towards the anode. However, since the gas reservoir was appended to the anode in this configuration, the electron density gradient was considerably smaller because of a reduced pressure differential. Thus, the observed longitudinal variations in discharge properties were the result of an anode-directed gas flow within the closed tube.

The anaphoretic nonuniformity observed in the xenon laser discharges provided a broad range of discharge conditions with a single gas fill. That is, the effects of increased pressure could be studied by simply observing quantities closer to the anode. Thus, for the range of variables considered experimentally, the effect upon electron density of moving towards the anode was equivalent to increasing the gas pressure for the same axial location. Figure 14(b) shows the current dependence of the steady-state electron number density at a pressure of 18.5 m Torr, with axial location as a parameter. The uppermost curve A represents the anode location, whereas the lowermost

curve E represents the cathode. Curves B, C and D represent data recorded at equally spaced intermediate axial locations separated by 8 cm. At the low-pressure cathode extreme, a linear increase of electron number density is seen, whereas a significant departure from linearity is observed at large currents for the high-pressure anode situation. This rapid increase in electron density could result from the anaphoretic pressure differential, which has been shown to increase with discharge current.^{17,20}

Insofar as the gas pressure near the cathode is essentially independent of discharge current, a linear increase with increasing current is quite reasonable. On the other hand, since the neutral gas pressure near the anode increases with discharge current, the electron density might be expected to increase with current at a greater than linear rate. However, cumulative ionization due to a large metastable population may also contribute to the observed current dependence.

At low currents, the ionization proceeds primarily by direct electron impact from the ground state and the electron density is expected to linearly increase with discharge current. However, as the electron density rises, the rate at which excited states are produced also increases. As these states, in turn, populate the long-lived 6 s xenon metastables, ionization via electron impact with the metastables becomes exceedingly more probable.



The metastable contribution to the electron production rate can be expressed in terms of N_{6s} and n_e , the metastable and electron densities, respectively.

$$\frac{dn_e}{dt} \underset{\text{by metastables}}{=} n_e N_{6s} \langle \sigma v \rangle_{6s}^i \quad (4-5)$$

The term $\langle \sigma v \rangle_{6s}^i$ is the velocity averaged product of the relative velocity v and the collisional cross section σ for ionization to occur from the 6 s level. Ionization from the metastable levels requires ~ 8.5 eV less energy than from the ground state. In the steady state, the electron production and loss rates must be equal, and since less energy need be expended to balance the loss rate when metastable ionization becomes important, a decrease in the electron temperature is expected in this region.

The steady-state measurements of the electron temperature in xenon, which assumed a Maxwellian velocity distribution, indicated that the temperatures typically ranged between 8,000 and 10,000 °K, which is reasonable on the basis of the low ionization potential of xenon. It should be pointed out that the Maxwellian velocity distribution for the electrons in a low-pressure narrow-bore xenon discharge has been experimentally verified by Wada and Heil⁴⁹ by means of an electron energy spectrometer. The electron temperatures displayed a noticeable decrease in the current range where the effects of cumulative ionization were expected to be significant. Cumulative ionization involving metastable levels has also been observed and reported in other noble gas discharges.^{50,51} Although it is likely that both effects contribute to this behavior, experimental evidence to be presented demonstrates that cumulative processes play an important role in excitation as well as ionization.

The onset of cumulative processes signifies that collisional reactions detrimental to laser population inversion have become important. This is

illustrated in Figure 15, where laser output is presented as a function of discharge current for three xenon pressures. At 18.5 m Torr, the laser output peaks at a discharge current of 53 ma. Referring to Figure 14(b), it is seen that above this current the electron density dependence is distinctly nonlinear towards the anode. A similar correlation was observed for higher and lower pressures, indicating that the collisional mechanisms responsible for cumulative ionization might also contribute to the destruction of population inversions.

This relationship can be understood by considering the processes responsible for the creation of population inversions. Figure 16 is a simplified energy level diagram for xenon,⁵² showing the 3.51μ ($5d_{33} \rightarrow 6p_{22}$) laser transition. Since the neutral xenon ground state consists of a $(5p)^6$ closed shell, the $5p^5$ (ms) and $5p^5$ (nd) states ($m > 5$; $n > 4$) are preferred for direct electron impact excitation⁵³ on the basis of electric dipole selection rules. Thus, the $5d_{33}$ level in xenon is electronically pumped from the ground state, whereas the $6p_{22}$ level is populated primarily through multiple radiative cascade from higher-lying s and d levels. Furthermore, from Tables 1 and 2,⁵³ the calculated lifetimes of the $5d_{33}$ and $6p_{22}$ levels are 135×10^{-8} sec and 4.4×10^{-8} sec, respectively; these calculations were performed using the Bates-Damgaard approximation.⁵⁴

Resonant trapping of ultraviolet emission to the ground state^{19,20} further prolongs the lifetime of the 5d levels. It is through this selective electronic pumping and favorable lifetime ratio that unsaturated gains of up to 70 db/m have been observed⁵⁵ for the strongly allowed 3.51μ transition in xenon. However, as the discharge current is increased, the 6s

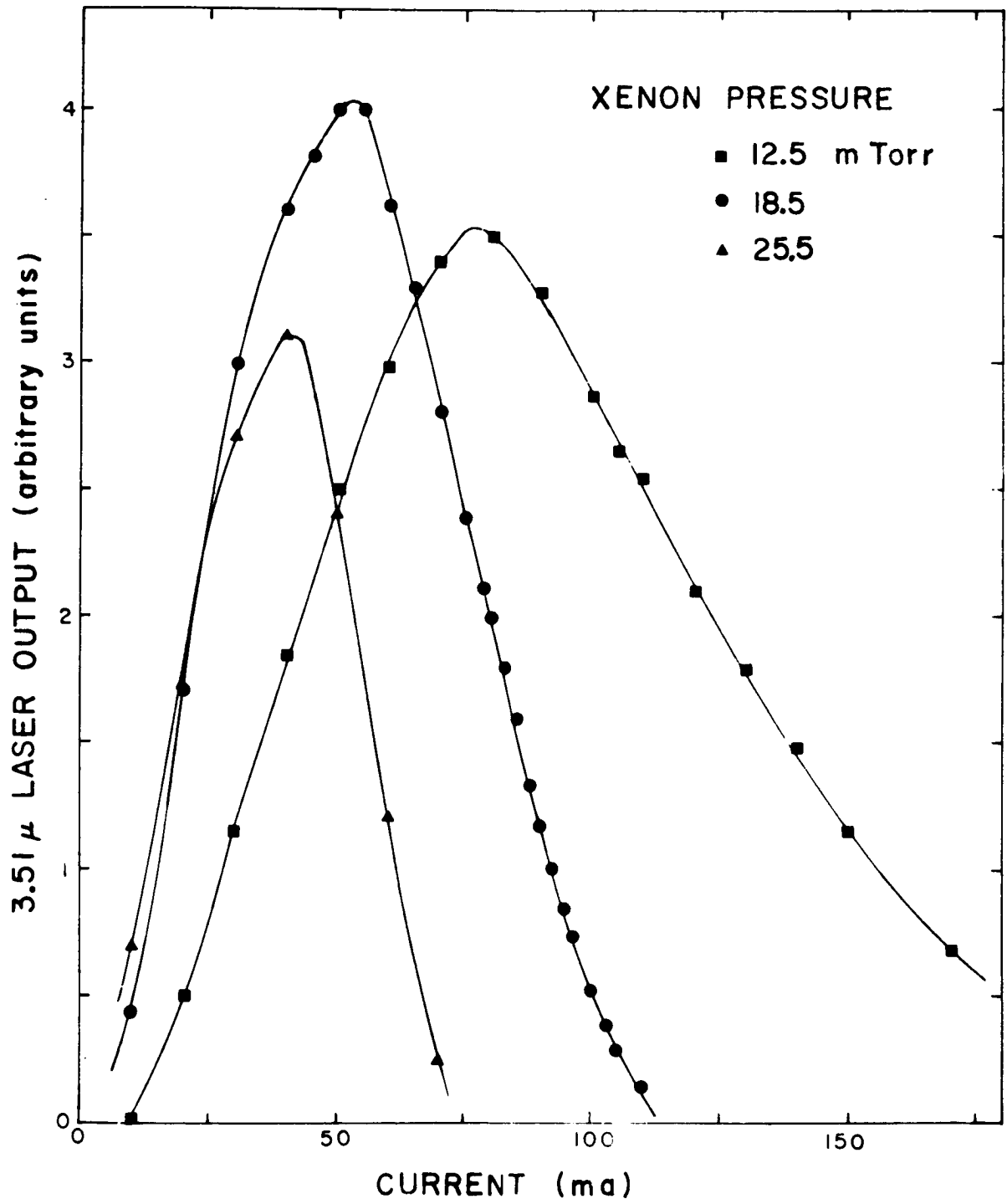


Figure 15. Current dependence of the 3.51 μ laser output for various xenon pressures.

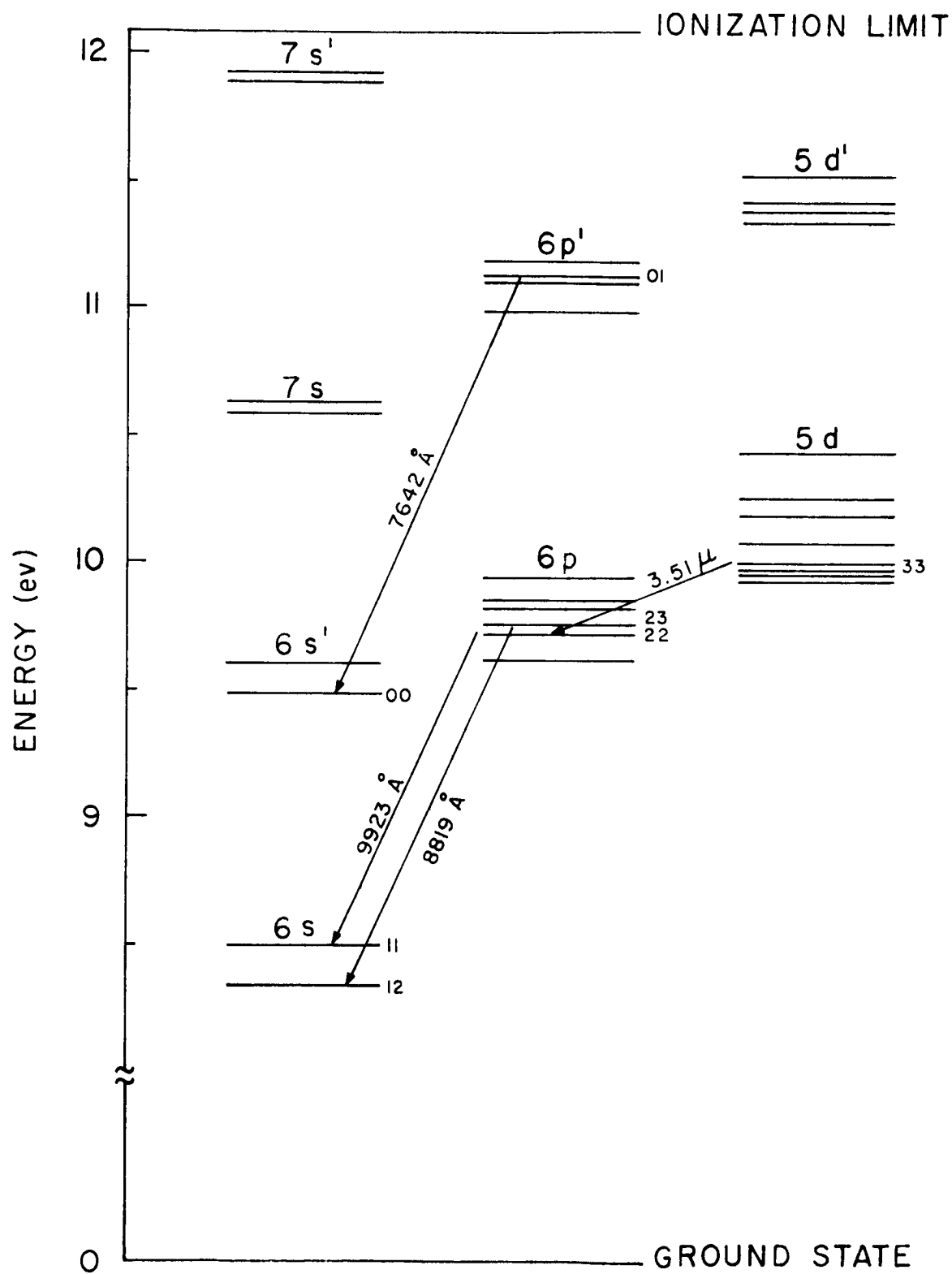


Figure 16. Simplified energy level diagram of the xenon system.

TABLE 1

ESTIMATED LIFETIMES OF THE 5d STATES OF XENON
USING THE BATES-DAMGAARD APPROXIMATION

Spectroscopic Notation		Estimated Lifetime
Racah	Systematic	
$5d \left[\begin{smallmatrix} 2 & 1/2 \end{smallmatrix} \right]_3^0$	$5d_{23}$	$72 \times 10^{-8} \text{ sec}$
$5d \left[\begin{smallmatrix} 2 & 1/2 \end{smallmatrix} \right]_2^0$	$5d_{22}$	91
$5d \left[\begin{smallmatrix} 1 & 1/2 \end{smallmatrix} \right]_1^0$	$5d_{11}$	24
$5d \left[\begin{smallmatrix} 1 & 1/2 \end{smallmatrix} \right]_2^0$	$5d_{12}$	238
$5d \left[\begin{smallmatrix} 3 & 1/2 \end{smallmatrix} \right]_3^0$	$5d_{33}$	135
$5d \left[\begin{smallmatrix} 3 & 1/2 \end{smallmatrix} \right]_4^0$	$5d_{34}$	537
$5d \left[\begin{smallmatrix} 1/2 \end{smallmatrix} \right]_1^0$	$5d_{01}$	275
$5d \left[\begin{smallmatrix} 1/2 \end{smallmatrix} \right]_1^0$	$5d_{00}$	236

TABLE 2

ESTIMATED LIFETIMES OF THE 6p STATES OF XENON
 USING THE BATES-DAMGAARD APPROXIMATION

Spectroscopic Notation		Estimated Lifetime
Racah	Systematic	
6p [1/2] ₀	6p ₀₀	2.7×10^{-8} sec
6p [3/2] ₂	6p ₁₂	2.7
6p [3/2] ₁	6p ₁₁	3.4
6p [5/2] ₃	6p ₂₃	3.2
6p [5/2] ₂	6p ₂₂	4.4
6p [1/2] ₁	6p ₁₁	4.6

metastables become more populous and begin to affect the laser population inversion. Spontaneous emission from the 6p levels to the metastables becomes radiatively trapped, and electronic collisions can excite the metastables directly into the 6p states.



In particular, these processes serve to populate the 6p₂₂ lower laser level and degrade the inversion, causing a decreased laser output at higher currents.

Enhanced electronic production due to cumulative ionization is surely accompanied by a cumulative excitation of xenon energy levels, particularly from the long-lived 6s metastables. Thus, it is consistent that evidence of cumulative ionization occurs for the same discharge conditions at which a decreased laser output is observed. For each pressure investigated, the peak laser output occurred at a discharge current corresponding to an anode electron density of $\sim 10^{12} \text{ cm}^{-3}$. This appears to be the electron density at which cumulative effects commence, contributing to a degraded laser output and possibly to the nonlinear dependence of electron density upon discharge current. Spectroscopic evidence to be presented further indicates that these cumulative processes become dominant at high electron number densities. In the following sections the effects of the laser fields upon these steady-state conditions will be presented, and an increased understanding of the collisional processes will follow from these studies.

4.2 The Effects of Lasering upon the Electron Gas

It has been established both theoretically and experimentally that the onset of lasering can dramatically alter excited state populations within the active laser medium through radiative and collisional relaxation processes.^{1,2,3,4,5} These changes occur even when the active medium is not within an optical cavity but is irradiated by resonant laser fields. In addition, the somewhat remarkable observation has been made^{6,7,8,9} that lasering in He-Ne mixtures can also influence the discharge current flowing through the He-Ne gas discharge. These observations have been confirmed here for the 6328 Å, 1.15 μ and 3.39 μ transitions in neon with current quenchings of up to 2 per cent having been observed.⁸ The present investigation is concerned with similar observations using the 3.51 μ laser transition in xenon, which indicate that the quenching phenomenon is not peculiar to the He-Ne system but is, in fact, the consequence of electronic collisional processes which occur within all gas discharges. Spatially resolved measurements of the effects of lasering upon the electron density and temperature are presented and are shown to be consistent with the observed discharge current behavior.

4.2.1 Laser-Induced Current Quenching

The first experimental evidence⁶ that laser fields could affect the state of the electron gas was the observed decrease in the discharge current during lasering. In xenon at a pressure of 18.5 m Torr, Figure 17 illustrates the change in discharge current due to lasering. Similar curves were obtained at the other pressures investigated. The quenching generally follows the laser output, and in this case reaches a maximum quenching of ~ 14 μa at 65 ma (~ 0.02 per cent quenching). This current quenching in xenon is notably

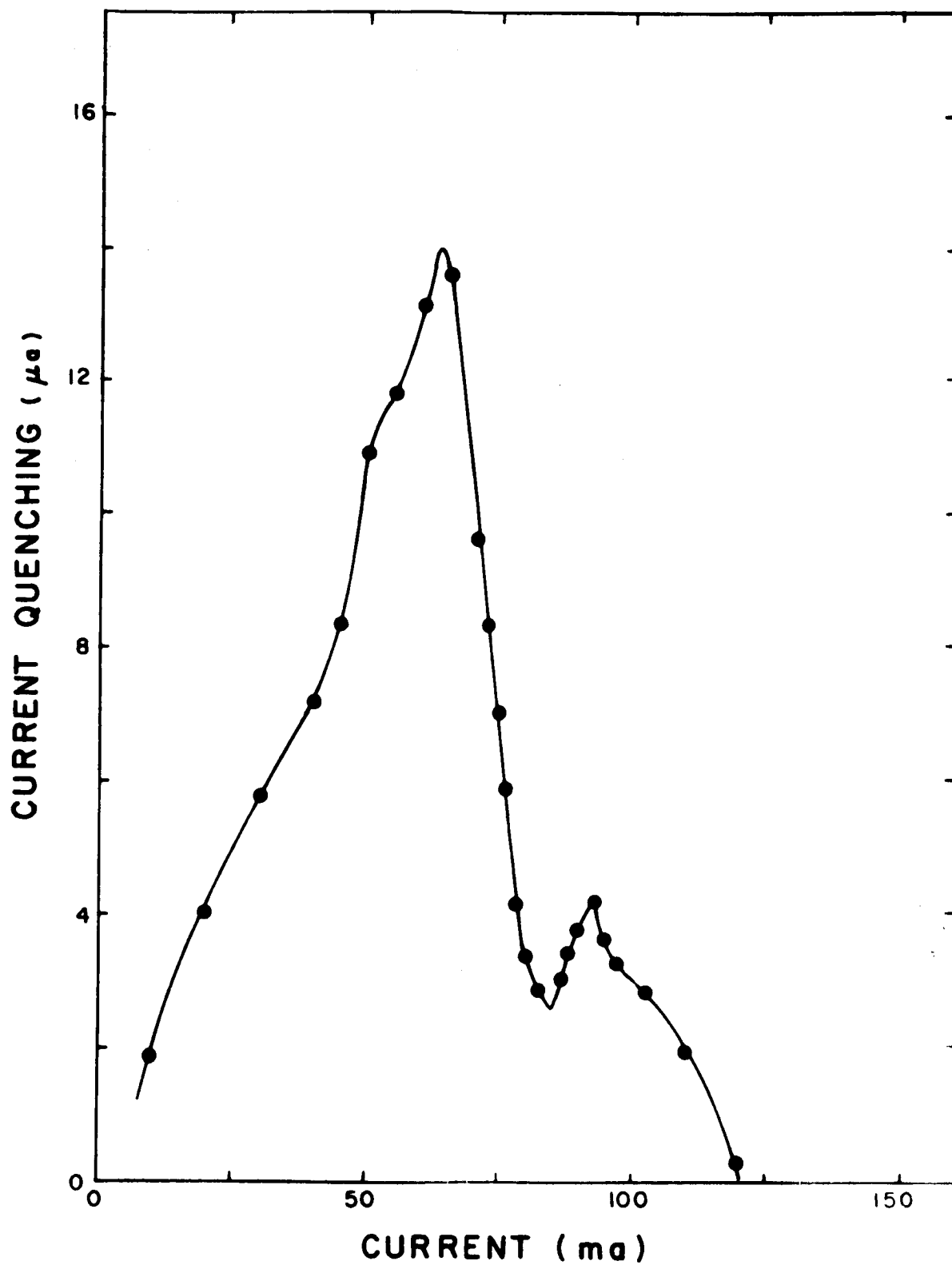


Figure 17. Current dependence of the laser-induced quenching of the discharge current at a xenon pressure of 18.5 m Torr.

smaller than the 2 per cent observed in the He-Ne mixtures. Furthermore, a distinct dip or minimum in the current quenching characteristic was observed consistently beyond the peak quenching. As seen in Figure 17, this minimum is quite pronounced, and for this pressure occurs at a current of 85 ma. This feature of the current quenching indicates that several counteracting effects of lasering possibly compete for dominance within the discharge tube.

It must be recalled that due to anaphoretic effects the discharge is not axially homogeneous, so that physical processes important at one end of the tube could be completely overwhelmed by competing processes at the other. Since the discharge current is a spatially integrated quantity, it reflects only the net result of this competition along the tube length. Furthermore, the current is composed of contributions from local electron number densities and drift velocities. That is,

$$I = n_e e v_d A \quad (4-8)$$

where I is the total discharge current, A is the cross-sectional area and n_e , v_d and e are the electronic density, drift velocity and charge, respectively. Thus, for a particular current the laser-induced current quenching is also an integrated quantity dependent upon the spatially resolved values of electron density and drift velocity changes due to lasering. In order to determine the specific nature of these electronic perturbations, it is necessary to have spatially resolved measurements of the electron parameters.

4.2.2 Laser-Induced Electron Density Perturbation

As was discussed in the previous chapter, the small changes incurred by the electron density were measured through the use of a demountable TM₀₁₀

microwave cavity and a phase sensitive detector. The microwave cavity provided the required spatial resolution and the phase sensitive detector furnished the high sensitivity necessary to measure the small shifts in resonant frequency brought about by lasering.

The solution of the electromagnetic boundary value problem, discussed in Appendix A, reveals that these shifts are proportional to changes in electron number density. Three pressures were investigated, and since the demountable cavity could be moved along the length of the discharge tube, data at several tube locations were also obtained. Figure 18 shows typical electron density changes due to lasering for three axial tube locations at a xenon pressure of 25.5 m Torr. Positive values of Δn_e represent enhancements, whereas negative values represent depletions.

These curves demonstrate conclusively that quenching of the laser discharge current is, in fact, partially due to a decrease in electron number density during lasering. As the discharge current is increased, the electron density depletion reaches a maximum of between 1.0 and $2.0 \times 10^9 \text{ cm}^{-3}$ for each axial location. In the high-pressure anode limit, this peak occurs for lower discharge currents, and a spike due to spurious laser oscillations is often observed. However, this disturbance is not troublesome, and in almost every case the peak depletion is found to correspond to an electron density of $\sim 5 \times 10^{11} \text{ cm}^{-3}$. Thus, the maximum electron density decrease lies between 0.2 and 0.4 per cent, substantially greater than the peak current quenching of 0.02 per cent. Presuming that the electron density changes at the center of the tube approximately represent an average variation along the tube length, the electron density variation of Figure 19 may be compared with the current quenching of Figure 17 at the same pressure. It is seen that the

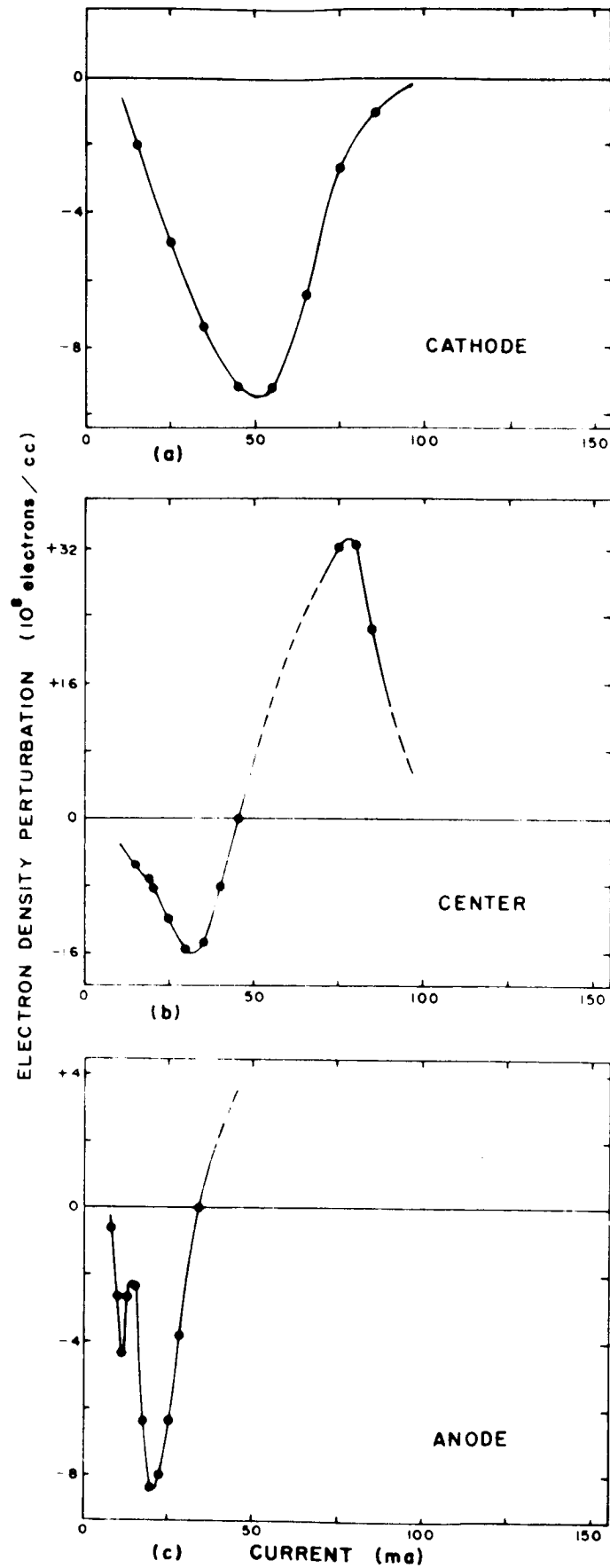


Figure 18. Current dependence of the electron density perturbation due to lasering at a xenon pressure of 25.5 m Torr at various locations along the discharge.

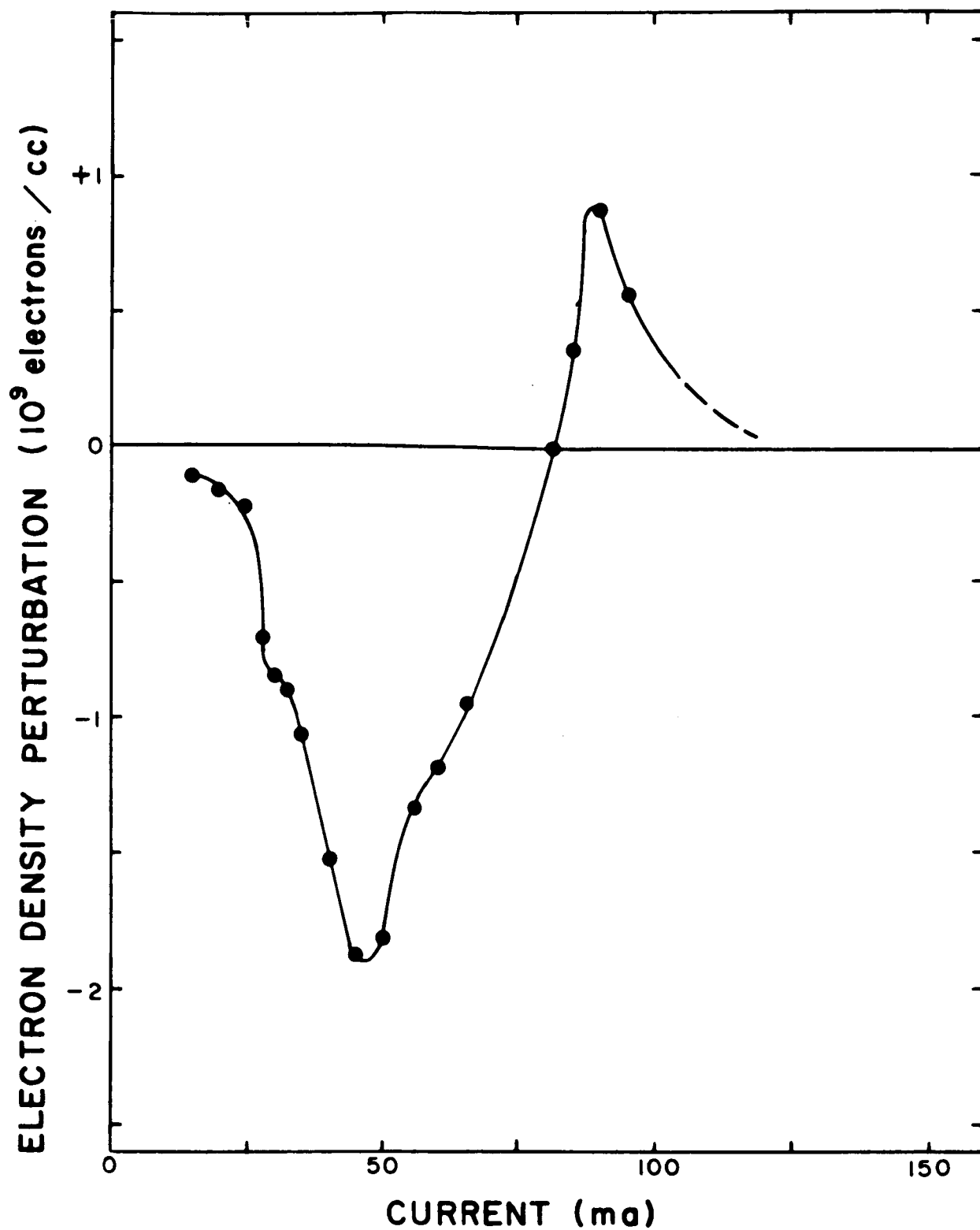


Figure 19. Current dependence of the laser-induced electron density perturbation at a xenon pressure of 18.5 m Torr at the center of the discharge.

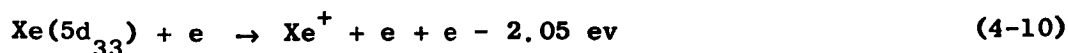
peak value of the density depletion occurs about 20 ma prior to the peak value of the current quenching. This indicates that although the current quenching is certainly closely related to the electron density depletion, the change in current cannot be completely explained without also considering the drift velocity change, since

$$\frac{\Delta I}{I} = \frac{\Delta n_e}{n_e} + \frac{\Delta v_d}{v_d} \quad (4-9)$$

A remarkable feature of the electron density change is that for electron densities in excess of $\sim 8 \times 10^{11} \text{ cm}^{-3}$, the electron concentration is actually enhanced due to lasering as seen in curves (b) and (c) of Figure 18. This change in the polarity of Δn_e indicates the dominance of a different physical process at these higher densities. This enhancement of the electron density may account for the anomalous dip in the current quenching curve of Figure 17, since both occur over the same current range. At the anode this electron density enhancement occurs at lower discharge currents due to the axial inhomogeneities in the steady-state plasma. Consequently, the effects of lasering upon the electron gas at one end of the laser may be entirely different than those at the other end.

It is clear that the physical processes resulting in enhancements and depletions of electron density during lasering must involve the gas of the excited atoms. The intense laser fields interact strongly with the resonant laser transition in the active medium, and through a net stimulated emission they drastically alter both the upper and lower laser level populations. This is the primary, first-order effect of lasering upon the active material,

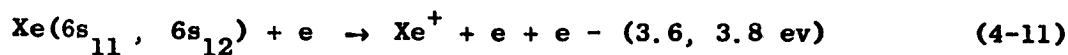
and any further effects must necessarily originate from this fundamental interaction. In particular, within a gaseous laser medium, various collisional reactions with the laser levels can couple this disturbance to the electron gas and to other excited atoms. Thus, the decrease in electron density due to lasering must be primarily associated with the marked decrease in upper laser level population. The reaction proposed to account for the decreased electron production is



and is similar to that suggested^{4,8,9} to explain observed discharge current decreases in He-Ne lasers. It is apparent that insofar as the $\text{Xe}(5d_{33})$ population contributes to electron production through this cumulative ionization process, its net conversion into $\text{Xe}(6p_{22})$ states during lasering serves to decrease ionization from the $\text{Xe}(5d_{33})$ level. Providing that the conversion products are not more rapidly ionized than the $\text{Xe}(5d_{33})$, then a net decrease in electron production through cumulative ionization is the result. With electron production thus inhibited, the tube voltage must increase to attempt to maintain the same discharge current. Thus, the tube impedance is effectively increased by lasering, and electron density and current flow are decreased.

In xenon for electron densities below $\sim 8 \times 10^{11} \text{ cm}^{-3}$, decreased electron production from the $5d_{33}$ level appears to dominate over other processes. Since in depopulating the $5d_{33}$ state the stimulated emission of 3.51μ radiation increases the energy required for ionization from 2.05 to 2.41 ev, fewer

electrons are energetically capable of ionizing an atom in the $6p_{22}$ state. Furthermore, the $6p_{22}$ lower laser level rapidly radiates to the 6s metastables with a calculated lifetime of 4.4×10^{-8} sec, so that the effective de-excitation due to lasering is from the $5d_{33}$ to the 6s levels, a change of ~ 1.7 ev. Despite the fact that ionization from the $6p_{22}$ or 6s levels might be more probable, the lower energy requirement apparently favors greater ionization from the $5d_{33}$ level for these discharge conditions. The situation is reversed, however, at higher currents or pressures ($n_e > 10^{12} \text{ cm}^{-3}$). As seen in Figures 17(b), 17(c) and 18, the electron density increases due to lasering; for these discharge conditions, increased ionization from the enhanced $6p_{22}$ and 6s metastables overcomes the reduced $5d_{33}$ ionization, resulting in a net increase in electron production. Since the metastables are long-lived and more populous at these higher electron densities, it is likely that the cumulative process is predominantly



although the $6p_{22}$ and $6s'$ levels are known to contribute to a lesser extent. Spectroscopic observations presented in the following section confirm the existence of such cumulative processes involving the 6s levels. Moreover, it should be noted that significant cumulative ionization occurs in a region where $n_e > 10^{12} \text{ cm}^{-3}$. In Figure 14(b), the electron density departs from linearity in approximately the same density range.

4.2.3 Laser-Induced Electron Temperature Variation

Since the electron density is quite definitely dependent upon lasering, it is only reasonable to expect the electron mean energy to also display some

laser dependence. At low electron densities when the net ionization is reduced by lasering due to reaction (4-10), fewer electrons experience inelastic ionizing collisions with the upper laser level. That is, approximately 10^9 fewer electrons per cm^3 lose the 2.05 ev kinetic energy of reaction (4-10) during lasering. Consequently, the electron gas retains more kinetic energy due to the stimulated cascade of lasering. Moreover, the increase in tube voltage further tends to increase electron energy. Conversely, at higher electron densities some 10^9 more electrons per cm^3 lose the ~ 3.7 ev of reaction (4-11) in contributing to the enhanced electron production. Thus, on the basis of this model, the mean electron energy would be expected to increase during electron density depletion, and decrease during the enhancement. Furthermore, at the transition point where $\Delta n_e = 0$, the greater energy lost to increased metastable ionization should generally tend to overwhelm the smaller energy saved through decreased $5d_{33}$ ionization.

The behavior expected upon the basis of the proposed cumulative ionization model is confirmed experimentally by radiometric measurements. It has been shown³⁹ that when the angle between the electric field vector in the waveguide and the axis of the discharge tube are perpendicular, Kirchhoff's radiation law for gaseous discharges can be expressed simply as

$$P_{\text{rad.}} = k T_{\text{rad.}} \epsilon \quad (4-12)$$

where

$P_{\text{rad.}}$ = noise power radiated from the discharge into the waveguide
per unit frequency interval

k = Boltzmann's constant

$T_{\text{rad.}}$ = temperature of the radiator

ϵ = emissivity of the radiator

It has been experimentally verified that the steady-state electron velocity distribution is Maxwellian for low-pressure, narrow-bore, xenon discharges.⁴⁹ However, as soon as the discharge begins to laser, the distribution function instantaneously departs from a Maxwellian due to the highly selective sinks and sources of electron energy associated with the laser levels. However, the large electron-electron collision frequency quickly redistributes the electron energies and re-establishes a Maxwellian distribution of a slightly different electron temperature.

Therefore, the incremental change in electron temperature due to lasering can be expressed as

$$\frac{\Delta T_e}{T_e} = \frac{\Delta P_{\text{rad.}}}{P_{\text{rad.}}} - \frac{\Delta \epsilon}{\epsilon} \quad (4-13)$$

Over the current range of interest, both the emissivity and the noise power were influenced by the onset of lasering. In general, the behavior of the laser-induced electron temperature perturbations is consistent with that proposed on the basis of the cumulative ionization model. Figure 20 is a plot of the electron temperature perturbation as a function of discharge current at the center of the tube for a xenon pressure of 18.5 m Torr.

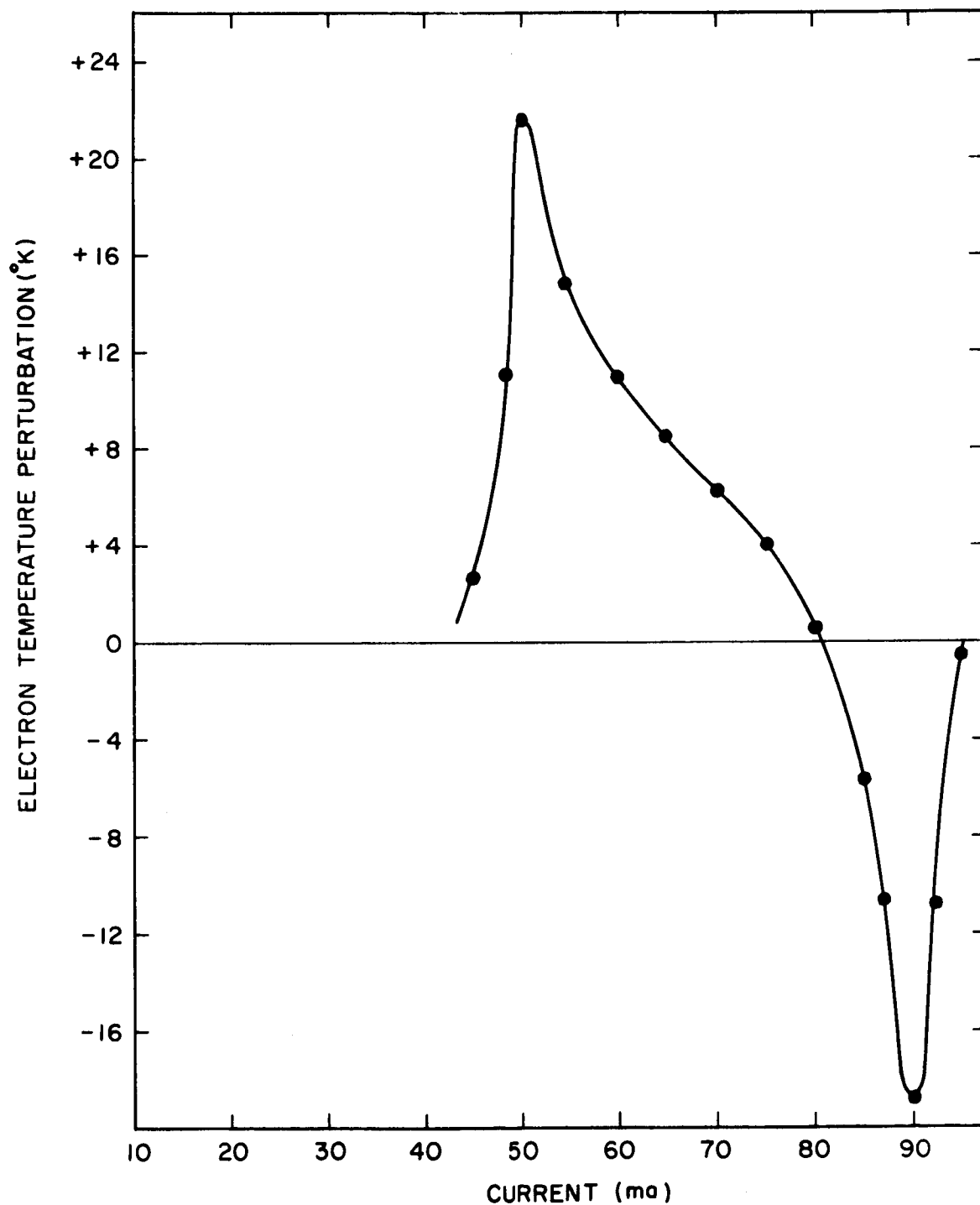


Figure 20. Current dependence of the electron temperature variations due to lasering at the center of the discharge for a xenon pressure of 18.5 m Torr.

If ΔT_e is compared with Δn_e of Figure 19, it is quite apparent that the electron temperature is enhanced when the density is depleted by lasering and decreased when the electron density is enhanced. In fact, the peak variations occur at about the same values of the discharge current. This same functional relation between ΔT_e and Δn_e occurs at other pressures and tube positions.

However, the fact that both Δn_e and ΔT_e change polarity at practically the same current indicates that decreased ionization from the upper laser level is not the only mechanism contributing to a laser-induced increase in the electron energy. Purely on the basis of reactions (4-10) and (4-11), the laser-induced electron temperature change would be expected to reverse polarity considerably sooner than observed. It is suggested that super-elastic collisions with the xenon metastables may in part account for the observed behavior of the electron temperature during lasering.

Additional support of the electron temperature measurements is furnished by the experimentally observed changes in the plasma-filled cavity Q due to lasering. When the contributions of the competing reactions, (4-10) and (4-11), approximately nullify one another, the net change in electron density is very small and a good qualitative indication of the change ΔQ is available. Since the loaded Q is inversely proportional to the microwave losses, the plasma contribution to the Q varies inversely as the real part of its microwave conductivity.⁵⁶ Thus, if electron-neutral collisions are more important than electron-ion collisions and $v_m^2 \ll \omega^2$,

$$Q \propto (\sigma_{\text{REAL}})^{-1} \propto (n_e v_m)^{-1} \quad (4-14)$$

where ν_m is the total electron-neutral collision frequency for momentum transfer and ω is the angular frequency of the applied microwave signal. Incrementally, this relation may be expressed as

$$(\Delta Q/Q) = - (\Delta n_e/n_e) - (\Delta \nu_m/\nu_m) \quad (4-15)$$

so that for small electron density changes, the percentage changes in Q and ν_m should be approximately equal and opposite. For these conditions, the collision frequency is an increasing function of electron energy, so that an increase in Q signifies a decrease in mean electron energy. In general, for the pressures and axial positions investigated, the currents for which ΔQ turned positive were about 5 ma less than those for which $\Delta n_e = 0$.

Further confirmation of the measurements of ΔT_e are supplied by the calculated change in electron drift velocity due to lasering. The drift velocity v_d is a monotonically increasing function of mean electron energy,^{57,58,59} and its changes can be computed using Equation (4-1).

Taking increments, this becomes

$$(\Delta v_d/v_d) = (\Delta I/I) - (\Delta n_e/n_e) \quad (4-16)$$

Since current is a spatially integrated quantity, however, electron density measurements must be taken at some average position along the discharge tube. This location was determined by graphical integration of the measured axial electron density gradient shown in Figure 14(a), and for a pressure of 18.5 m Torr was found to be 4.0 cm from the geometric center towards the anode.

Using these measured values of $\Delta I/I$ and $\Delta n_e/n_e$, drift velocity changes were computed and are presented in Table 3. The drift velocity and, hence, the electron temperature increase with lasering up to about 60 ma. For larger currents the electron temperature is decreased by lasering. Thus, both the change in Q measurements and the computed drift velocity variations are in good qualitative agreement with the radiometric observations and confirm the predictions of the cumulative ionization model.

Electronic collisions with excited xenon atoms transfer the initial laser-induced perturbation to both the electron number density and to the average electron energy. These changes in the state of the electron gas can further influence excited state populations through additional electron collisions with both ground state and excited xenon atoms. Hence, collisional as well as radiative processes can distribute the initial perturbation to excited levels; The following section describes these interactions experimentally and presents further evidence of the cumulative process.

4.3 Effects of Lasering upon the Excited Atomic State Populations

The population of an excited state is dependent upon the processes which create the state and the relaxation mechanisms which destroy it. In a multi-level energy system, these reactions for each level are intricately interconnected; every source is accompanied by a loss from some other state. Thus, the selective conversion of the upper laser level into the lower during lasering affects the populations of all states dependent even indirectly upon the laser levels. In a gaseous discharge, these source and relaxation processes are generally either radiative or collisional, or some combination of the two.

TABLE 3

EXPERIMENTALLY OBSERVED LASER-INDUCED CURRENT
 AND ELECTRON DENSITY DECREASES
 AND COMPUTED CHANGES IN ELECTRON DRIFT VELOCITY
 AT A XENON PRESSURE OF 18.5 m Torr
 WITH ALL QUANTITIES EXPRESSED AS A PERCENTAGE OF THEIR NON-LASERING VALUES

Current		Laser-Induced Perturbations		
I (ma)	$\frac{\Delta I}{I} \%$	$\frac{\Delta n_e}{n_e} \%$	$\frac{\Delta v_d}{v_d} \%$	
20	$- 2.08 \times 10^{-2}$	$- 1.97 \times 10^{-1}$	$+ 1.86 \times 10^{-1}$	
30	- 2.30	- 5.64	+ 5.41	
40	- 2.16	- 3.30	+ 3.08	
45	- 2.08	- 2.62	+ 2.41	
50	- 2.05	- 1.90	+ 1.69	
55	- 2.10	- 0.75	+ 0.54	
60	- 2.43	- 0.23	- 0.01	
65	- 1.97	~ 0	- 0.20	

Thus, the investigation of excited state population adjustments to lasering is in reality the study of the complex radiative and collisional coupling of energy levels within the excited state gas.

Since the primary effect of lasering is the stimulated radiative emission from upper to lower laser level, changes in spontaneous emission from these levels are termed as primary radiative perturbations and are generally the strongest of all line intensity perturbations. Similarly, the subsequent transmission of these changes to other energy levels through spontaneous radiative emission is designated as a secondary radiative process. Various types of collisions between perturbed species can also couple the disturbance to other energy levels; this group includes both electron-atom and atom-atom collisions. In general, these perturbations are noticeably smaller than those due to radiative processes. In the low-pressure xenon discharges studied here, both primary and secondary radiative processes are evident, and the effects of electronic collisions with neutral and excited xenon atoms are seen. However, because of the low pressures and the massive nature of the xenon atom, no evidence of collisional mixing due to atom-atom collisions^{2,4,60} was observed.

The spectral variations investigated here provided a great wealth of data concerning excited state populations, but only a few representative line intensity changes will be presented for purposes of illustration. For each discharge line discussed, many others were observed to display the same behavior. Figure 21 presents intensity changes due to lasering for three spectral lines, together with the corresponding changes in electron density. These quantities were measured as a function of current at the center of the

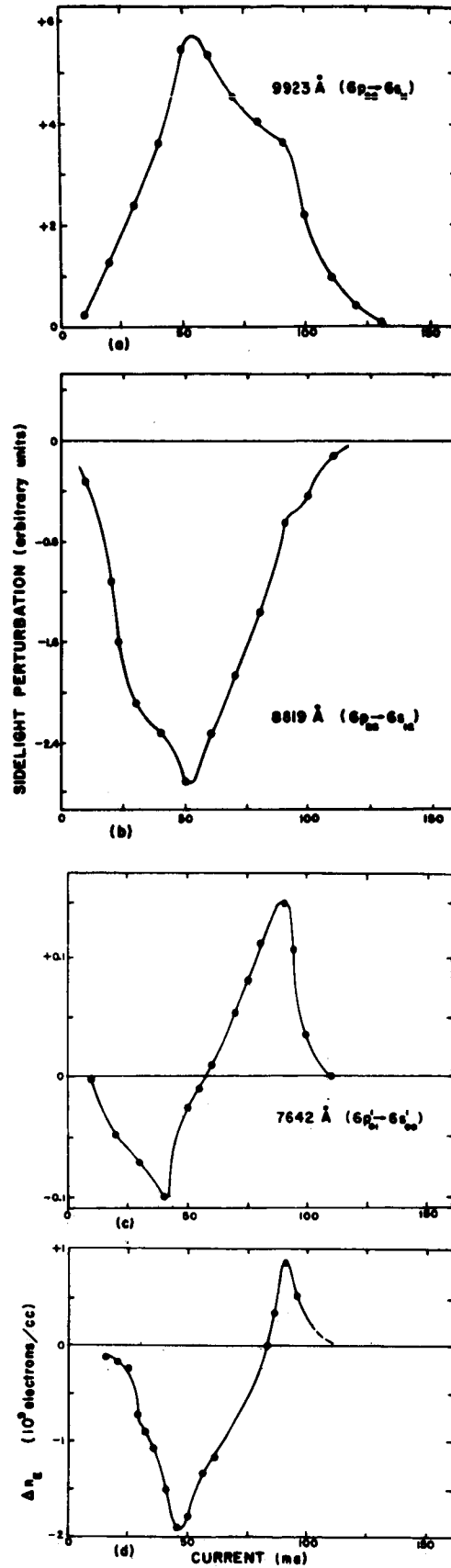


Figure 21. Comparison of the current dependence displayed by the laser-induced perturbations of the sidelight and the electron density at the center of the discharge for a xenon pressure of 18.5 m Torr.

discharge tube at a xenon pressure of 18.5 m Torr. Positive values signify enhancements, and negative values denote quenchings. The 9923 \AA ($6p_{22} \rightarrow 6s_{11}$) variation of curve (a) represents a primary radiative perturbation, since this transition originates on the lower laser level. This enhancement is caused by stimulated emission from the $5d_{33}$ state into the $6p_{22}$, and follows the laser output of Figure 15 quite closely up to its peak at 53 ma. This is consistent with the optical maser theory of Lamb⁶¹ which states that the radiative perturbation of the population of the laser levels is proportional to the radiation field intensity.

However, for currents beyond the peak of the laser output, it is apparent that stimulated emission from the $5d_{33}$ level is not the only mechanism contributing to the enhanced $6p_{22}$ population. In this region, cumulative effects involving the 6s metastables become important. Beyond 80 ma, curve (d) of Figure 21 shows the results of increased ionization from the 6s metastables during lasing. The secondary peak in the 9923 \AA sidelight enhancement at ~ 90 ma indicates that the increased ionization is accompanied by increased excitation from the xenon metastables into the 6p states. Both the electron density increase and the secondary enhancement of the 9923 \AA sidelight occur over the same current range. As would be expected, exactly the same behavior is exhibited by the 9045 \AA ($6p_{22} \rightarrow 6s_{12}$) xenon transition which also begins on the lower laser level of the 3.51μ laser.

The 8819 \AA ($6p_{23} \rightarrow 6s_{12}$) transition of curve (b) is representative of a secondary radiative perturbation in which the decrease in upper laser level population is radiatively coupled to an allowed lower-lying level, which in this case is the $6p_{23}$ level. In accordance with the $j-l$ coupling selection

rules, the only quantum mechanically allowed decay routes for atoms in the $5d_{33}$ state are to either the $6p_{22}$ or the $6p_{23}$ level.¹³ As shown in Table 4, spontaneous emission to the $6p_{22}$ level is 20 times more probable than to the $6p_{23}$ state; nevertheless, it is sufficiently strong that any changes in the $5d_{33}$ level are reflected in the population of the $6p_{23}$ state. Consequently, the depletion of the $5d_{33}$ level during lasering decreases the $6p_{23}$ population. Hence, the 8819 Å emission is quenched in accordance with the laser field strengths. At low currents, the laser-induced variations of electron and metastable density are of the opposite polarity, so that changes due to cumulative excitation should be small. Above 80 ma, however, increased excitation from the 6s metastables begins to compete with the secondary radiative process causing a distinct decrease in the sidelight quenching. This again coincides with the peak of the electron number density enhancement which has been attributed to increased ionization of the 6s metastables.

The 7642 Å ($6p'_{01} \rightarrow 6s'_{00}$) transition of curve (c) originates on a level which lies above both laser levels and is not optically connected to either the laser levels or the 6s metastables. Nonetheless, this line is also affected due to 3.51 μ laser action, even though the connection to the laser level perturbation is clearly nonradiative. The obvious similarity between this sidelight variation and the electron density changes of curve (d) indicates that electronic collisions are responsible. The 6s' metastables are the most likely collision partners, since they are long-lived and are radiatively coupled to the 6p', but not the 6p, levels. It is also possible that radiative cascade from perturbed higher-lying levels could contribute to this disturbance. For each of the discharge lines illustrated in Figure 21, evidence is seen of cumulative excitation into the 6p and 6p' levels

TABLE 4

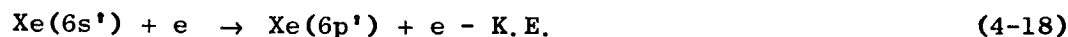
RELATIVE LINE STRENGTHS OF THE ($5d \rightarrow 6p$) TRANSITIONS IN XENON
USING THE $j-l$ COUPLING SCHEME OF RACAH

Lower Level	Upper Level							
	$5d[1/2]_0^0$	$5d[1/2]_1^0$	$5d[3/2]_1^0$	$5d[3/2]_2^0$	$5d[5/2]_2^0$	$5d[5/2]_3^0$	$5d[7/2]_3^0$	$5d[7/2]_4^0$
$6p[1/2]_0$		50	50					
$6p[1/2]_1$	50	100	25	125				
$6p[3/2]_1$	10	5	5	80	16	189		
$6p[3/2]_2$		25	16	144	21	294		
$6p[5/2]_2$		10	9	1	84	6	400	
$6p[5/2]_3$				14	6	120	20	540

through the reactions²⁴



and



Population enhancement of 6p and 6p' levels at ~ 90 ma coincides with electron number density enhancement, and the deleterious effect of metastable excitation into the 6p₂₂ level is reflected in a reduced population inversion and laser output above ~ 55 ma.

At higher metastable and electron densities, this 6p₂₂ electronic pumping in conjunction with the trapping of radiation from the 6p₂₂ level is sufficient to completely destroy the population inversion and extinguish laser action. This effect is illustrated in Figure 22, in which the 9923 Å (6p₂₂ → 6s₁₁) laser-induced sidelight variation at the anode is presented as a function of discharge current for xenon pressures of 12.5, 18.5 and 25.5 m Torr. As expected for low currents, the 9923 Å sidelight variation followed the laser output shown in Figure 15. However, for discharge currents corresponding to $n_e > 2 \times 10^{12} \text{ cm}^{-3}$, the sidelight intensity was actually diminished by laser action for each pressure investigated, indicating that the lower laser level was depopulated due to lasering! This behavior implied that the inverted population had been destroyed and the 3.51 μ transition was absorptive under these conditions.

The problem was resolved by monitoring the spontaneous emission of the 3.51 μ transition along the side of the tube in the vicinity of the anode.

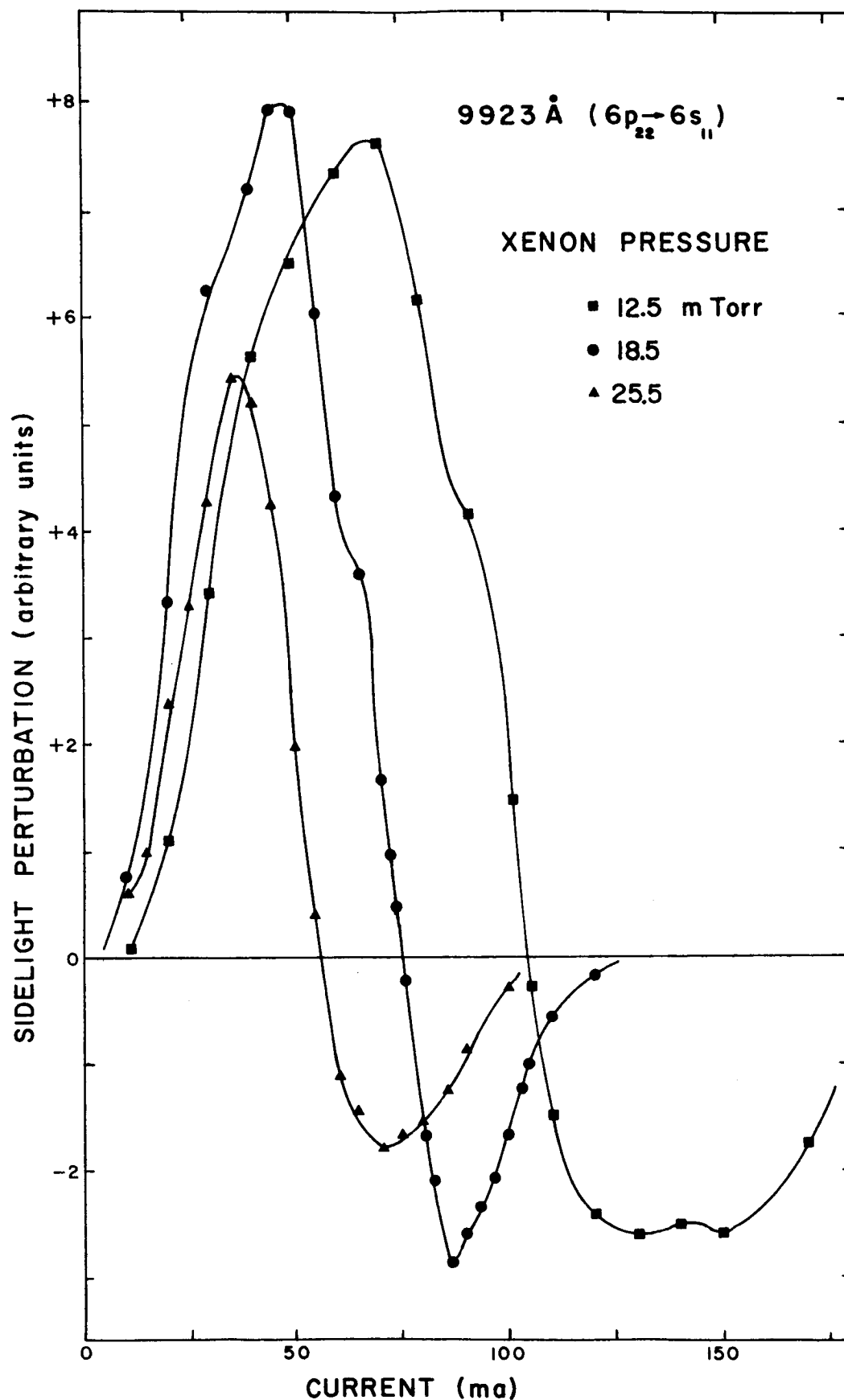


Figure 22. Current dependence of the laser-induced perturbation of the 9923 \AA sidelight at the anode end of the discharge for various pressures.

In regions where the 9923 Å sidelight exhibited a laser-induced enhancement, the spontaneous emission from the $5d_{33}$ level was quenched by lasering, denoting a depopulation of the upper laser level via induced emission. Therefore, under these conditions, the anode portion of the discharge was contributing to the laser output. However, at higher currents where the 9923 Å sidelight was strongly quenched, the spontaneous emission from the $5d_{33}$ level was enhanced, indicating that the 3.51μ transition was now absorptive and actually detrimental to the laser output. Therefore, although the majority of the xenon discharge is contributing to the laser output, the anode portion for high currents acts as an absorptive loss within the optical cavity. Under these conditions, electronic excitation from the 6s metastables not only contributes to increased ionization, but also populates the 6p levels to such an extent that the laser inversion is destroyed.

The absorption of 3.51μ laser radiation at the anode provides a useful check upon the validity of cumulative excitation and ionization processes. Since this absorption constitutes precisely the opposite perturbation of the laser levels that a net stimulated emission does, a reversal in the sign of laser-induced disturbances would be expected in this range. This effect is illustrated by the spectral variations at the anode presented in Figure 23 for a pressure of 18.5 m Torr. In curve (b), the laser-induced behavior of the 8819 Å ($6p_{23} \rightarrow 6s_{12}$) transition is normal for currents below 75 ma, displaying an initial quenching due to decreased spontaneous emission from the $5d_{33}$ level, followed by a sidelight enhancement at ~ 65 ma. This same enhancement is displayed by the 9923 Å sidelight in curve (a) and is attributed to an increased electronic excitation from the 6s metastables which for these

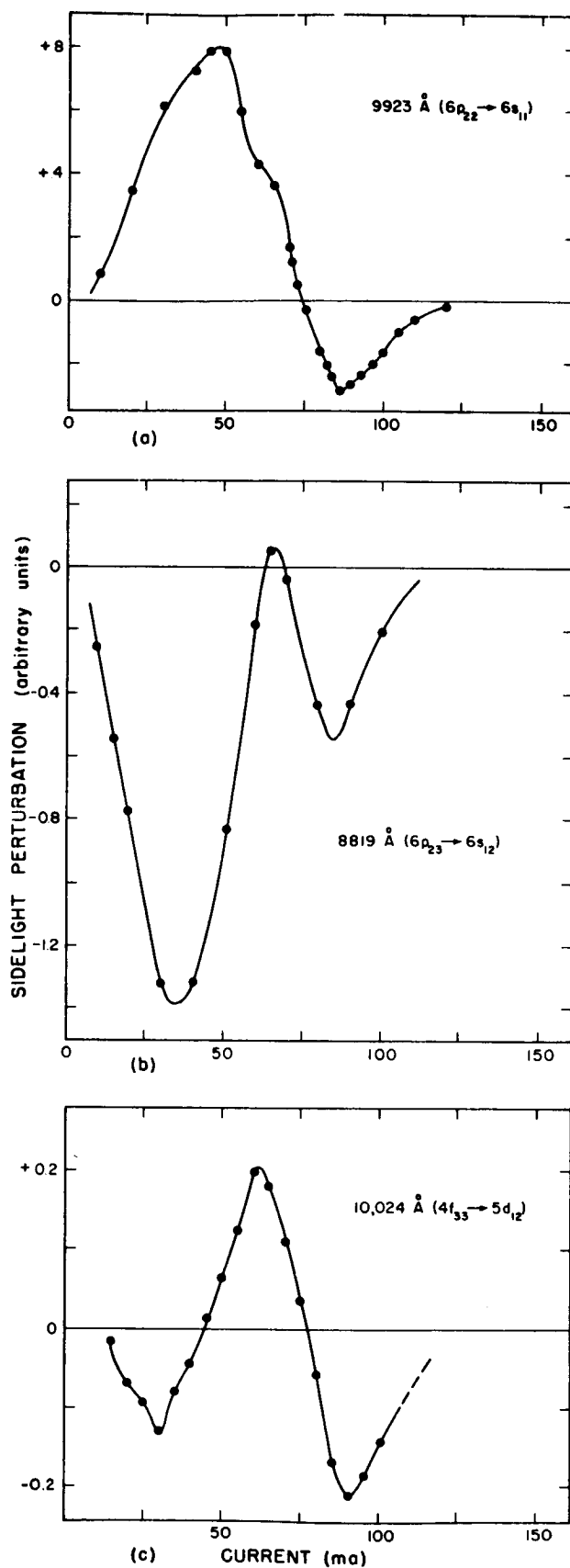
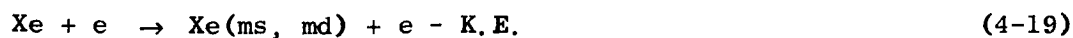


Figure 23. Comparison of the current dependence displayed by the laser-induced sidelight perturbations at the anode end of the discharge for a xenon pressure of 18.5 m Torr.

conditions are increased during lasering. However, when absorption of the laser radiation occurs above ~ 75 ma, the 8819 \AA sidelight perturbation reverses polarity and attains a peak quenching at ~ 90 ma, indicating that the absorptive destruction of $6p_{22}$ states has decreased the 6s metastable populations resulting in decreased excitation from the 6s metastables.

Since excitation from the metastable levels has been shown to accompany electron production from these levels, the measured electron density changes might also be expected to display a similar behavior. Although numerical values of Δn_e were unavailable beyond ~ 40 ma for this pressure at the anode, it was observed that the electron density increased due to lasering between 50 and 70 ma and appeared to decrease beyond this current. The intensity variation of the $10,024 \text{ \AA}$ ($4f_{33} \rightarrow 5d_{12}$) sidelight, typical of changes in all lines originating on levels above the $5d_{33}$, supports the proposal that the electron density is decreased by lasering for high discharge currents at the anode. High-lying levels are populated primarily by electron impact with atoms either in the ground state or in metastable states. Even when direct excitation from the ground state and the metastable states is improbable, these levels are populated by radiative cascade from higher-lying levels. Thus, most high-lying states are populated either directly by electron impact, or indirectly through a subsequent radiative decay process. Therefore, reactions of the type



and



in addition to metastable excitation cause the populations of highly excited levels to be sensitive to the state of the electron gas. As a consequence, spontaneous emission originating from these levels has been observed to display the same perturbations as the electron density over a broad range of discharge conditions. Thus, the 10,024 Å sidelight in curve (c) is quenched for low currents and attains a peak enhancement at ~ 65 ma. Evidence of cumulative excitation is also seen on the 9923 Å and 8819 Å curves of Figure 23 at this same current. At higher currents, the 10,024 Å emission is again quenched, attaining a peak quenching at ~ 90 ma where laser absorption is known to be a maximum. Thus, it may be inferred that the electron density decreases due to lasering at these high currents as a result of the net absorption of 3.51μ radiation at the anode.

The spectroscopic observations, thus, confirm and extend the conclusions formulated on the basis of spatially resolved electron density measurements. Furthermore, the laser-induced perturbations of certain discharge line intensities can be used to determine the nature of electron density variations where microwave cavity methods are unreliable.

V. SUMMARY AND CONCLUSIONS

This investigation has experimentally determined the effects of lasering upon both the state of the electron gas and the excited atomic state populations in a DC excited xenon discharge situated in a high-gain optical cavity. The radiative and collisional processes responsible for various laser-induced perturbations of the electron gas and excited state parameters have been identified. Although these particular experiments were performed upon a low-pressure 3.51 μ xenon laser, the general nature of the conclusions drawn are applicable to all gas lasers.

Spatially resolved microwave experiments were undertaken to investigate the properties of the electron gas; spectroscopic investigations yielded information regarding the excited atomic state populations of the gas discharge. In order to measure the small effects of lasering upon the plasma parameters, several plasma diagnostic techniques of high sensitivity were developed which incorporated the property of spatial resolution, the inherent sensitivity of synchronous detection and the precision of a null type measurement.

Microwave cavity measurements reveal that local electron densities can either be increased or decreased due to lasering by approximately 10^9 cm^{-3} , depending upon local discharge conditions. Radiometric measurements indicate that the electron temperature is also affected by lasering; the observed behavior of ΔT_e is in good qualitative agreement with the temperature variations predicted on the basis of observed cavity Q changes and computed values of the drift velocity variation. It is suggested that the observed laser dependent behavior of the electron gas parameters is primarily due to cumulative

ionization processes involving the upper laser level and the 6s metastables. Atoms excited to these levels serve as sources for electron production and when their number is changed by lasering, the density and energy of the electron gas is correspondingly altered.

There is also some evidence of superelastic collisions between electrons and xenon metastables which do not directly alter the electron density but which are an effective source of electron energy. The variations in the state of the electron gas are reflected in the discharge current flowing through the laser tube and account for the observed current quenching due to lasering. The laser-induced current changes represent a longitudinal average of local variations in electron properties along the tube. The specific nature of these electronic perturbations and the identity of the competing physical processes involved is provided by spatially resolved microwave and spectroscopic experiments.

The laser output itself is also a longitudinally integrated quantity, dependent upon contributions from local population inversions. Due to the establishment of anaphoretic gradients within the xenon discharge tube, these inversions were not uniform along the tube length. Spatially resolved spectroscopic observations demonstrated that even though the laser was oscillating, the anode portion of the discharge tube was actually absorbing the laser radiation under certain circumstances. Thus, to insure optimum lasering conditions along the entire length of the discharge, spectroscopic checks should be made, and a gas return loop should be employed if necessary to prevent electrophoretic gradients in discharge properties.

Spectroscopic observations of the effects of lasering provide insight into the mechanisms responsible for the creation and destruction of excited atomic state populations. The relative importance of the collisional and radiative processes which determine the excited state populations are dependent upon steady-state conditions; it is demonstrated that the effects of lasering can be completely reversed for different discharge conditions. In general, the spectral perturbation is largest for the primary radiative mechanisms, and decreases in magnitude as the disturbance is transmitted by secondary collisional processes. The population of the high-lying states is shown to be strongly dependent upon the electron density. Any variation in electron production is reflected by a similar variation in the population of these states. Excitation of xenon metastables into the 6p states is shown experimentally to be a significant process at high discharge currents, and largely accounts for the degradation of laser output through collisional pumping of the lower laser level.

Collisional mixing^{2,4,60} of excited state populations which was prevalent in He-Ne mixtures was not observed in the xenon discharges; this is most likely due to the lower xenon pressures used and the greater mass of the xenon atoms, since the rate at which such collisions occur is proportional to the densities of the collision partners and their relative velocity. Furthermore, the laser-induced perturbations of the sidelight intensity were not large enough to be utilized in such applications as infrared laser interferometry.⁶² This was due to the relatively weak laser output power resulting from the combined effects of the single mode operation, the narrow doppler width and the short discharge length. However, the pure xenon discharges

offered an advantage over the He-Ne mixtures in that electron-atom collisional processes could be studied conveniently in the absence of such overpowering effects as the helium metastable pumping of neon upper laser levels.

The state of the electron gas is noticeably altered by lasering in low-pressure xenon discharges. Since excited state populations and current flow are strongly dependent upon electronic properties, the entire character of the gaseous discharge is affected by the lasering process. The relationship of any reaction or parameter to the electron gas can be deduced by monitoring an appropriate discharge variable and analyzing the effects of lasering upon it. With a knowledge of laser-induced changes in the state of the electron gas, it should be possible to identify a variety of collisional and radiative processes and to determine numerical values for cross sections and radiative decay rates. Such an approach might find particular application in the analysis and optimization of new laser systems. A further advantage lies in the spatial resolution provided by the small diameter of the perturbing laser beam; spatially resolved studies of the propagation of this disturbance within the test plasma can also be conducted. Temporally resolved investigations of the time lag between cause and effect could be undertaken using a Q-switched optical cavity or a rotating mirror system. Moreover, the medium under study is not required to be located within the laser cavity, nor are these investigations especially limited to gaseous plasmas.

APPENDIX A

ELECTRON DENSITY MEASUREMENTS USING A TM_{010} MICROWAVE CAVITY

The cavity development based upon first-order perturbation theory assumes that the influence of the electron gas can be considered as a small perturbation upon the fields of the empty cavity.³¹ For microwave frequencies in the C-band range, this requires the electron densities $\ll 2.5 \times 10^{11}$. In general, the majority of the electron densities encountered are in excess of this limit, rendering the assumptions of the perturbation development invalid. In order to relate the cavity frequency shift to the electron density of the plasma, a solution of an electromagnetic boundary value problem is required.

The fundamental relationship between the electric and magnetic fields is given by Maxwell's equations

$$\nabla \times \vec{H} = \vec{J} + \frac{\partial \vec{D}}{\partial t} \quad (A-1)$$

$$\nabla \times \vec{E} = - \frac{\partial \vec{B}}{\partial t} \quad (A-2)$$

$$\nabla \cdot \vec{D} = 0 \quad (A-3)$$

$$\nabla \cdot \vec{B} = 0 \quad (A-4)$$

Due to the charge neutrality of the plasma, the net volume charge density is zero. The conductivity, permittivity and permeability of the plasma medium can be expressed in terms of the field quantities.

$$\vec{J} = \sigma \vec{E} \quad (A-5)$$

$$\vec{D} = \epsilon \vec{E} \quad (A-6)$$

$$\vec{B} = \mu \vec{H} \quad (A-7)$$

Using Maxwell's equations and incorporating the sinusoidal time dependence of the fields, the following relation describing the electric field is obtained.

$$\nabla(\nabla \cdot \vec{E}) - \nabla^2 \vec{E} = \frac{\omega^2}{c^2} n^2 \vec{E} \quad (A-8)$$

where n is the complex index of refraction of the medium and ω is the angular frequency.

Taking the divergence of Equation (A-1) results in

$$\vec{E} \cdot \nabla n^2 + n^2 (\nabla \cdot \vec{E}) = 0 \quad (A-9)$$

It is apparent that in order for the divergence of \vec{E} to vanish, the microwave cavity must be excited in a mode in which the \vec{E} field has no component along the direction of a refractive index gradient.

The xenon plasma under study is enclosed in a cylindrical tube and is expected to have a radial electron density gradient. Therefore, the cavity must be excited in a mode for which $E_r = 0$. If a very small length of plasma is inserted into the cavity, the density can be treated as axially uniform to

a first approximation; in the vicinity of the anode this approximation is rather crude. The TM_{010} cavity mode is ideally suited for such conditions, since its fields are described by

$$\vec{E} = E_z \hat{z} \quad (A-10)$$

$$\vec{H} = H_\phi \hat{\phi} \quad (A-11)$$

With the above considerations, the fields can be shown to satisfy the following conditions

$$\frac{\partial^2 E_z}{\partial r^2} + \frac{1}{r} \frac{\partial E_z}{\partial r} + \frac{\omega^2 n^2}{c^2} E_z = 0 \quad (A-12)$$

$$H_\phi = -\frac{j}{\omega \eta_o^2 \epsilon_o} \frac{\partial E_z}{\partial r} \quad (A-13)$$

where η_o is the impedance of free space. Performing a transformation of variables from r to x where

$$x = \frac{2\pi}{\lambda} r = \frac{\omega}{c} r \quad (A-14)$$

Equations (A-12) and (A-13) reduce to

$$\frac{\partial^2 E_z}{\partial x^2} + \frac{1}{x} \frac{\partial E_z}{\partial x} + n^2 E_z = 0 \quad (A-15)$$

$$H_{\phi} = - \frac{j}{\eta_0} \frac{\partial E_z}{\partial x} \quad (\text{A-16})$$

Equation (A-15) is the Bessel equation of zeroth order in terms of the parameter nx . Therefore,

$$E_z = C J_0(nx) + D Y_0(nx) \quad (\text{A-17})$$

and

$$H_{\phi} = + \frac{jn}{\eta_0} [C J_1(nx) + D Y_1(nx)] \quad (\text{A-18})$$

where J_m and Y_m denote the m^{th} order Bessel functions of the first and second kind.

In this particular situation, the fields in three concentric cylindrical regions must be calculated and the boundary conditions upon the tangential components of the E and H fields satisfied at the three interfaces. The regions occupied by the plasma, glass and air are illustrated in Figure 24.

In the region between the outside wall of the glass tubing and the inside wall of the cavity, $b_2 < r < a$, the refractive index is unity and the fields are described by

$$E_z = C_1 J_0(x) + C_2 Y_0(x) \quad (\text{A-19})$$

$$H_{\phi} = \frac{j}{\eta_0} [C_1 J_1(x) + C_2 Y_1(x)] \quad (\text{A-20})$$

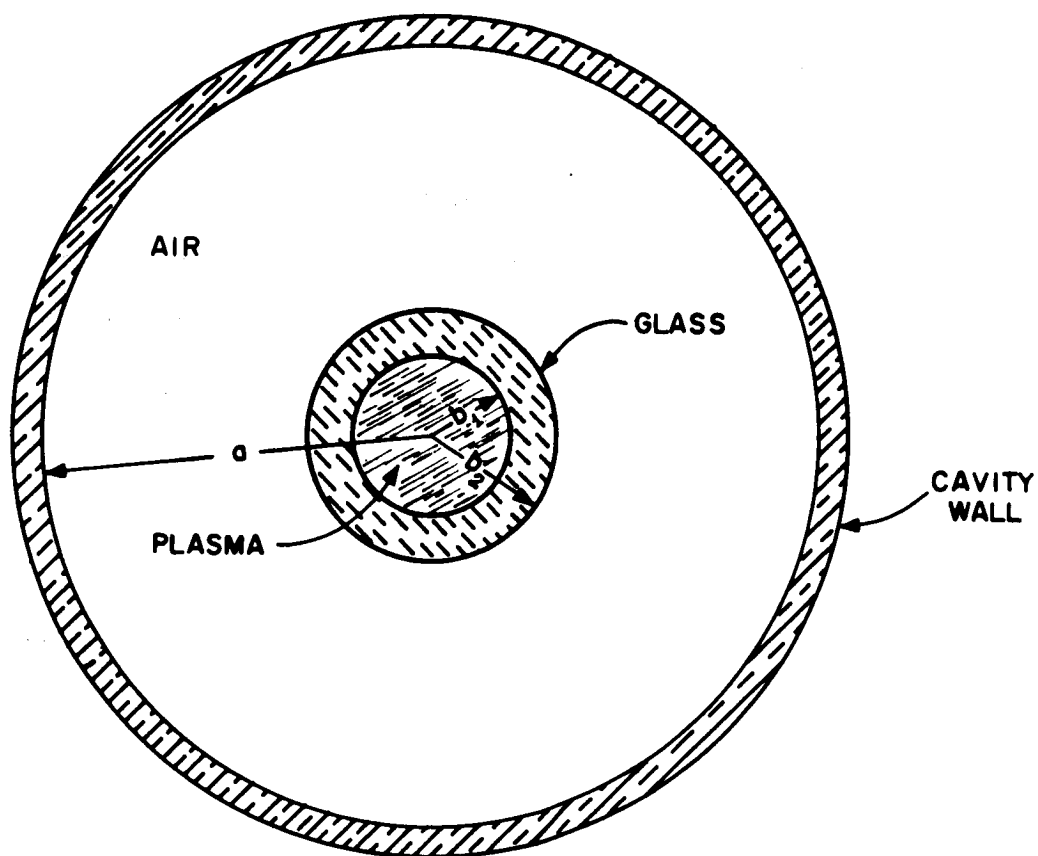


Figure 24. Cross-sectional view of the plasma-filled, quartz discharge tube within the TM_{010} microwave cavity.

In the region filled with glass, $b_1 < r < b_2$, the index of refraction is denoted by n_g and the fields are

$$E_z = C_3 J_0(n_g x) + C_4 Y_0(n_g x) \quad (A-21)$$

$$H_\phi = \frac{j}{\eta_0} n_g [C_3 J_1(n_g x) + C_4 Y_1(n_g x)] \quad (A-22)$$

The fields within the plasma filled region, $0 < r < b_1$, are not as easily expressed in terms of Bessel functions, since the index of refraction is no longer constant due to the radial gradients in the electron density established by the ambipolar diffusional losses. Approximating the radial profile of the electron density by a parabola, the index of refraction of the plasma can be expressed as

$$n^2(r) = n^2(0) (1 + k^2 r^2) \quad (A-23)$$

At the inside wall of the discharge tube, the electron density must vanish. Therefore,

$$n^2(b_1) = 1 = n^2(0) (1 + k^2 b_1^2) \quad (A-24)$$

and

$$k^2 = \frac{1 - n^2(0)}{n^2(0) b_1^2} \quad (A-25)$$

Expressing the index of refraction in terms of the x coordinates

$$n^2(x) = n^2(0) + \frac{1}{B_1^2} [1 - n^2(0)] x^2 \quad (\text{A-26})$$

where $B_1 = \frac{\omega}{c} b_1$.

The parameter $n(0)$ is the refractive index of the medium on the axis and is related to $n_e(0)$, the electron density on the axis, by³⁵

$$n(0) \approx \left[1 - \left(\frac{\omega_{p_0}}{\omega} \right)^2 \right]^{1/2} \quad \text{for } \nu^2 \ll \omega^2 \quad (\text{A-27})$$

where the plasma frequency is defined as

$$\omega_{p_0}^2 = \frac{n_e(0) e^2}{m \epsilon_0} \quad (\text{A-28})$$

ϵ_0 is the permittivity of free space, e is the electronic charge and m is the mass of an electron.

Equation (A-15) in the plasma region takes the form

$$\frac{\partial^2 E_z}{\partial x^2} + \frac{1}{x} \frac{\partial E_z}{\partial x} + [n^2(0) + k^2 n^2(0) x^2] E_z = 0 \quad (\text{A-29})$$

It was shown by Fuchs³⁶ that such equations have solutions of the form

$$E_z = x^\rho \sum_{m=0}^{\infty} a_m x^m \quad (\text{A-30})$$

where $a_0 \neq 0$ and ρ is a constant.

Substituting (A-30) into (A-29), the indicial equation is found.

$$\rho (\rho - 1) a_0 + \rho a_0 = 0 \quad (\text{A-31})$$

shows that, in this case, $\rho = 0$. The coefficients a_m are only nonzero if m is an even integer. a_m is of the form

$$a_m = 0 \quad \text{for } m = \text{odd integer and for } m < 0 \quad (\text{A-32})$$

$$a_m = - \frac{n^2(0)}{m^2} [a_{m-2} + k^2 a_{m-4}] \quad \text{for } m = \text{even integer} \quad (\text{A-33})$$

The first few nonzero coefficients are

$$a_0 \neq 0 \quad (\text{A-34})$$

$$a_2 = - \frac{n^2(0)}{4} a_0 \quad (\text{A-35})$$

$$a_4 = \frac{n^2(0)}{16} \left[\frac{n^2(0)}{4} - k^2 \right] a_0 \quad (\text{A-36})$$

$$a_6 = + \frac{n^4(0)}{36} \left[\frac{5}{16} k^2 - \frac{n^2(0)}{64} \right] a_0 \quad (\text{A-37})$$

Therefore, in the region of the plasma, i.e., $0 < r < b_1$

$$E_z = a_0 \left\{ 1 - \frac{n^2(0)}{4} x^2 + \frac{n^2(0)}{16} \left[\frac{n^2(0)}{4} - k^2 \right] x^4 + \dots \right\} \quad (\text{A-38})$$

$$H_{\phi} = \frac{j n^2(0)}{\eta_0} a_0 \left\{ \frac{x}{2} - \frac{1}{4} \left[\frac{n^2(0)}{4} - k^2 \right] x^3 + \frac{n^2(0)}{6} \left[\frac{5k^2}{16} - \frac{n^2(0)}{64} \right] x^5 + \dots \right\} \quad (A-39)$$

Now that the fields in all three regions have been determined, the arbitrary coefficients can be evaluated by applying the boundary conditions. The interfaces a , b_2 and b_1 in r -space become A , B_2 and B_1 in x -space, i.e.,

$$A = \frac{\omega}{c} a \quad (A-40)$$

$$B_2 = \frac{\omega}{c} b_2 \quad (A-41)$$

$$B_1 = \frac{\omega}{c} b_1 \quad (A-42)$$

The frequency ω can be expressed in terms of frequency shift $\Delta\omega$ and the no-plasma resonance frequency by

$$\Delta\omega = \omega - \omega_0 \quad (A-43)$$

At $x = A$, $E_z = 0$; therefore,

$$E_z^{\text{air}} = C_1 [J_0(x) + \alpha Y_0(x)] \quad (A-44)$$

and

$$H_{\phi}^{\text{air}} = \frac{j}{\eta_0} C_1 [J_1(x) + \alpha Y_1(x)] \quad (A-45)$$

where

$$\alpha = - \frac{J_o(A)}{Y_o(A)} \quad (A-46)$$

At the air-glass interface $x = B_2$, the E_z and H_ϕ fields must be equal in both the glass and the air. From Equations (A-19), (A-20), (A-44) and (A-45), the fields in the glass are found to be

$$E_z^{\text{glass}} = C_3 [J_o(n_g x) + \beta Y_o(n_g x)] \quad (A-47)$$

$$H_\phi^{\text{glass}} = \frac{j n_g}{\eta_o} C_3 [J_1(n_g x) + \beta Y_1(n_g x)] \quad (A-48)$$

where

$$\beta = \frac{n_g J_1(n_g B_2) - \gamma J_o(n_g B_2)}{\gamma Y_o(n_g B_2) - n_g Y_1(n_g B_2)} \quad (A-49)$$

where

$$\gamma = \frac{J_1(B_2) + \alpha Y_1(B_2)}{J_o(B_2) + \alpha Y_o(B_2)} \quad (A-50)$$

At the plasma-glass interface $x = B_1$, a rather complex equation for the refractive index is arrived at upon applying the boundary conditions to Equations (A-38), (A-39), (A-47) and (A-48).

$$\begin{aligned}
& \frac{n^2(0)}{2} \left\{ 1 - \frac{B_1^2}{2} \left[\frac{n^2(0)}{4} - k^2 \right] - \frac{B_1^4 n^2(0)}{48} \left[5k^2 - \frac{n^2(0)}{4} \right] \right. \\
& \quad \left. + \frac{B_1^6 n^2(0)}{64} \left[\frac{7}{18} n^2(0) k^2 - \frac{n^4(0)}{144} - k^4 \right] + \frac{B_1^8 n^4(0)}{46,080} \left[89k^4 - \frac{15}{2} n^2(0) k^2 + \frac{n^4(0)}{16} \right] \right\} \\
& = \delta \left\{ 1 - \frac{B_1^2 n^2(0)}{4} + \frac{B_1^4 n^2(0)}{16} \left[\frac{n^2(0)}{4} - k^2 \right] + \frac{B_1^6 n^4(0)}{144} \left[\frac{5k^2}{4} - \frac{n^2(0)}{16} \right] \right. \\
& \quad \left. - \frac{B_1^8 n^4(0)}{1024} \left[\frac{7}{18} n^2(0) k^2 - \frac{n^4(0)}{144} - k^4 \right] - \frac{B_1^{10} n^6(0)}{921,600} \left[89k^4 - \frac{15}{2} n^2(0) k^2 + \frac{n^4(0)}{16} \right] \right\} \\
& \hspace{25em} (A-51)
\end{aligned}$$

where

$$\delta = \frac{n_g}{B_1} \frac{[J_1(n_g B_1) + \beta Y_0(n_g B_1)]}{[J_0(n_g B_1) + \beta Y_0(n_g B_1)]} \quad (A-52)$$

A computer solution of Equation (A-51) in conjunction with the equations defining the various parameters in terms of measurable quantities yields the electron density of the plasma as a function of the plasma-induced cavity frequency shift.

APPENDIX B

COMPUTERIZED VALUES OF THE ELECTRON DENSITY
AS A FUNCTION OF SHIFT IN MICROWAVE CAVITY FREQUENCY

In the previous appendix, a development of the electromagnetic fields within the plasma filled region of a TM_{010} microwave cavity was presented. The results of the computerized solution of Equation (A-51) relating the electron density to the resonant frequency shift appear in Table 5.

TABLE 5

COMPUTER SOLUTION OF THE RELATIONSHIP BETWEEN THE ELECTRON DENSITY
AND THE RESONANT FREQUENCY SHIFT OF THE TM_{010} MICROWAVE CAVITY

Frequency Shift (Mc)	Electron Density (cm^{-3})	Frequency Shift (Mc)	Electron Density (cm^{-3})
1	3.37×10^{10}	26	8.91×10^{11}
2	6.47	27	9.26
3	1.01×10^{11}	28	9.61
4	1.35	29	9.97
5	1.69	30	1.03×10^{12}
6	2.02	31	1.07
7	2.36	32	1.10
8	2.70	33	1.14
9	3.04	34	1.17
10	3.38	35	1.21
11	3.73	36	1.24
12	4.07	37	1.28
13	4.41	38	1.32
14	4.75	39	1.35
15	5.10	40	1.39
16	5.44	41	1.42
17	5.78	42	1.46
18	6.13	43	1.50
19	6.48	44	1.53
20	6.82	45	1.57
21	7.17	46	1.60
22	7.52	47	1.64
23	7.86	48	1.68
24	8.21	49	1.71
25	8.56	50	1.75

APPENDIX C

PERTINENT ELECTRONIC CIRCUIT DIAGRAMS

The schematic circuit diagrams of the various electronic equipment designed for this experiment appear in this appendix. Figure 25 is the schematic of the phase sensitive detector used to monitor the laser-induced changes in the plasma parameters. Figure 26 is the schematic of the circuit used to bias the crystal of the microwave diode switch. Figure 27 is the schematic circuit diagram of the transistorized amplifier used in conjunction with the InSb detector.

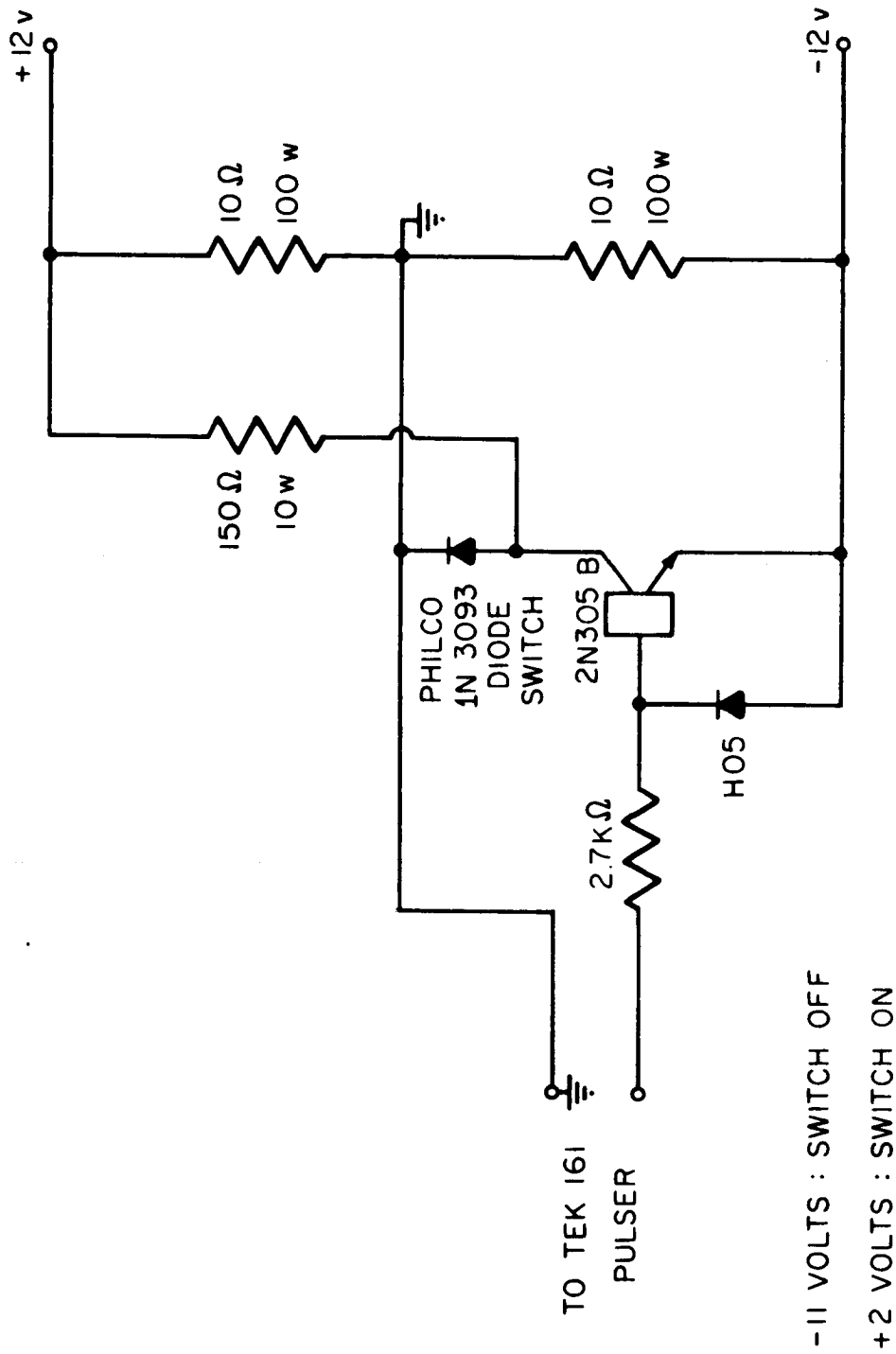


Figure 26. Schematic circuit diagram of the biasing supply for the diode switch.

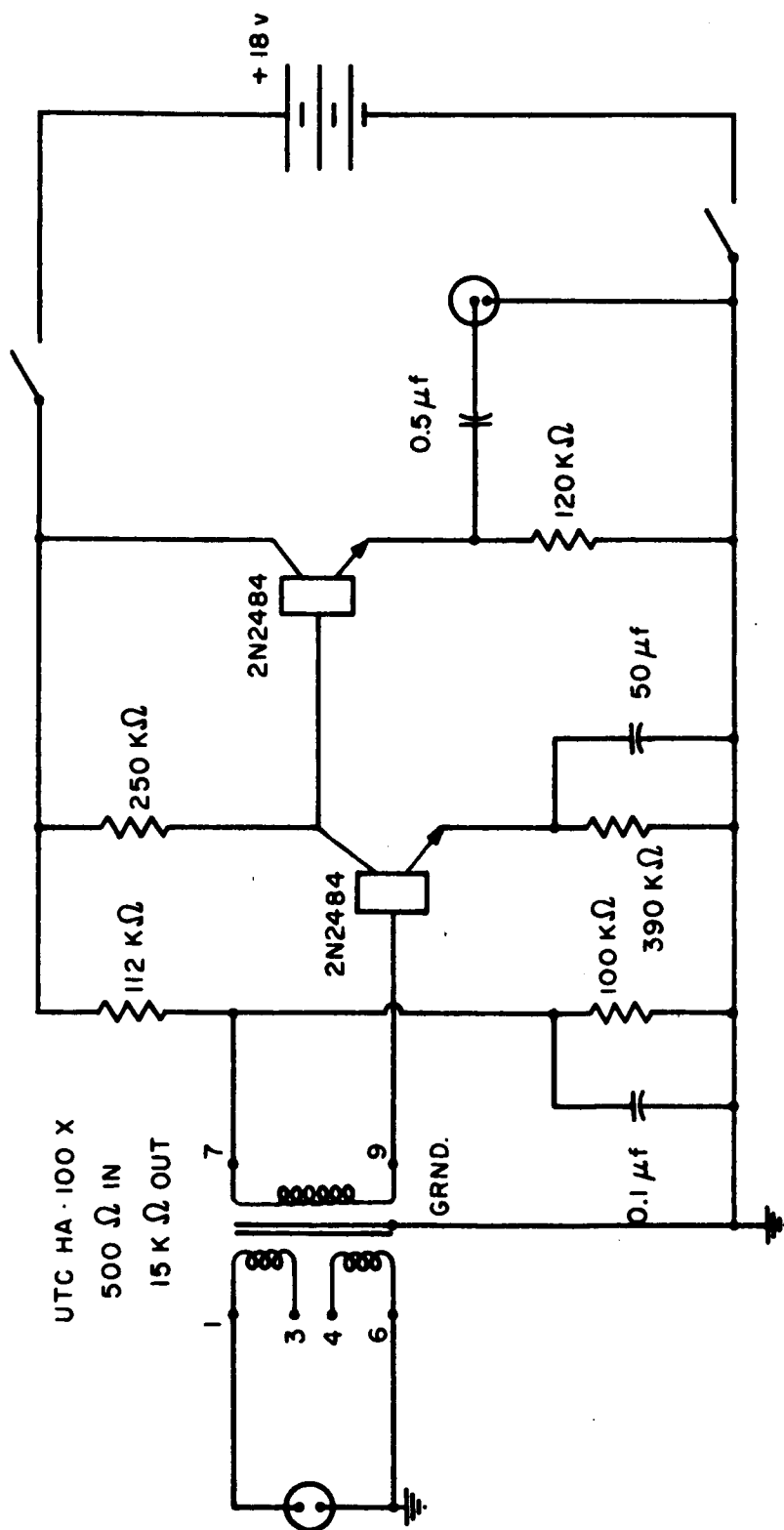


Figure 27. Schematic circuit diagram of the low-noise transistorized amplifier for the InSb detector.

LIST OF REFERENCES

1. White, A. D. and Rigden, J. D., "The Effect of Super Radiance at 3.39μ on the Visible Transitions in the He-Ne Maser," Appl. Phys. Letters, Vol. 2, 1963, p. 211.
2. Parks, J. H. and Javan, A., "Collision-Induced Transitions within Excited Levels of Neon," Phys. Rev., Vol. 139, 1965, p. A1351.
3. Waksberg, A. L. and Carswell, A. I., "Optical Resonator Effects on the Population Distribution in He-Ne Gas Lasers Determined from Sidelight Measurements," Appl. Phys. Letters, Vol. 6, 1965, p. 137.
4. Weaver, L. A. and Freiberg, R. J., "Laser-Induced Perturbations of Excited State Populations in a He-Ne Discharge," J. Appl. Phys., Vol. 37, 1966, p. 1528.
5. Freiberg, R. J. and Weaver, L. A., "The Effects of Lasering upon the Electron Gas and Excited State Populations in Xenon Discharges," to be published in J. Appl. Phys., 1966.
6. Garscadden, A., Bletzinger, P. and Friar, E. M., "Moving Striations in a He-Ne Laser," J. Appl. Phys., Vol. 35, 1964, p. 3432.
7. Schiffner, G. and Seifert, F., "On the Dependence of He-Ne Laser Discharge Current on Laser Action," Proc. IEEE, Vol. 53, 1965, p. 1657.
8. Weaver, L. A. and Goldstein, L., "Spectroscopic and Microwave Investigation of Lasering Plasmas," Contract No. AF 19(628)-3307, Scientific Report No. 4, February 1966.
9. Garscadden, A. and Adams, S. L., "Current Changes Due to Lasing Action," Proc. IEEE, Vol. 54, 1966, p. 427.
10. Weaver, L. A. and Freiberg, R. J., "Electron Density Measurements in an Afterglow Plasma using a Frequency-Compensated Microwave Cavity Technique," to be published.
11. Racah, G., "A New Type of Vector Coupling in the Complex Spectrum," Phys. Rev., Vol. 61, 1942, p. 537(L).

LIST OF REFERENCES - (continued)

12. American Institute of Physics Handbook, Sec. 7, McGraw-Hill Book Co., Inc., New York, 1957, p. 77.
13. Faust, W. L. and McFarlane, R. A., "Line Strengths for Noble-Gas Maser Transitions; Calculations of Gain/Inversion at Various Wavelengths," J. Appl. Phys., Vol. 35, 1964, p. 2010.
14. Weaver, L. A. and Freiberg, R. J., "Radiative Decay Patterns and Collisional Processes in a He-Ne Discharge," paper presented at the Eighteenth Annual Gaseous Electronics Conference, Minneapolis, Minnesota, October 20-22, 1965.
15. Einstein, A., "Zur Quanten Theorie der Strahlung," Phys. Zeit., Vol. 18, 1917, p. 121.
16. Jordan, E. C., Electromagnetic Waves and Radiating Systems, Prentice-Hall, Inc., Englewood Cliffs, New Jersey, 1950, p. 291.
17. Mitchell, A. C. and Zemansky, M. W., Resonance Radiation and Excited Atoms, Macmillan Co., New York, 1934, p. 99.
18. Birnbaum, G., Optical Masers, Academic Press, New York and London, 1964, p. 9.
19. Holstein, T., "Imprisonment of Resonance Radiation in Gases. II," Phys. Rev., Vol. 83, 1951, p. 1159.
20. Bennett, W. R., Jr., "Gaseous Optical Masers," Appl. Opt. Suppl. Opt. Masers, Vol. 2S, 1962, p. 24.
21. Loeb, L. B., Basic Processes of Gaseous Electronics, University of California Press, Berkeley and Los Angeles, 1961, p. 185.
22. Kennard, E. H., Kinetic Theory of Gases, McGraw-Hill Book Company, Inc., New York and London, 1938, p. 29.
23. Margenau, H., "Conduction and Dispersion of Ionized Gases at High Frequencies," Phys. Rev., Vol. 59, 1946, p. 508.
24. Jancel, R. and Kahan, T., "Theorie Non Maxwellienne des Plasmas Homogenes et Anisotropes," Nuovo Cimento, Vol. 12, 1954, p. 573.
25. Bayet, M., Delcroix, J. L. and Denisse, J. F., "Theorie Cinetique des Plasmas Homogenes Faiblement Ionises, I," J. Phys. Radium, Vol. 15, 1954, p. 795.

LIST OF REFERENCES - (continued)

26. Gurevich, A. V., "On the Effect of Radio Waves on the Properties of Plasma (Ionosphere)," Soviet Physics - J.E.T.P., Vol. 3, 1957, p. 895.
27. Chapman, S. and Cowling, T. G., The Mathematical Theory of Non-Uniform Gases, Cambridge University Press, London, 1952.
28. Allis, W. P., "Motion of Ions and Electrons," in Handbuch der Physik, (S. Flugge, Ed.), Springer-Verlag, Berlin, Germany, Vol. 2, 1957, p. 383.
29. Brown, S. C., Basic Data of Plasma Physics, John Wiley and Sons, Inc., New York, 1959, p. 24.
30. Molmud, P., "Langevin Equation and AC Conductivity of Non-Maxwellian Plasmas," Phys. Rev., Vol. 114, 1959, p. 29.
31. Slater, J. C., "Microwave Electronics," Rev. Mod. Phys., Vol. 18, 1946, p. 480.
32. Oskam, H. J., "Microwave Interaction of Disintegrating Gaseous Discharge Plasmas," Philips Res. Rep., Vol. 13, 1958, p. 401.
33. Jackson, J. D., Classical Electrodynamics, John Wiley and Sons, Inc., New York, 1962, p. 241.
34. Abramowitz, M. and Stegun, I. A., Handbook of Mathematical Functions, National Bureau of Standards, Applied Mathematics Series, 1965, p. 358.
35. Rose, D. J. and Clark, M., Jr., Plasmas and Controlled Fusion, John Wiley and Sons, Inc., New York, 1961, p. 186.
36. Sokolnikoff, I. S. and Radheffer, R. M., Mathematics of Physics and Modern Engineering, McGraw-Hill Book Company, Inc., New York, 1958, p. 160.
37. Schiff, L. I., Quantum Mechanics, McGraw-Hill Book Company, Inc., New York, 1955, p. 262.
38. Bekefi, G., Hirschfield, J. L. and Brown, S. C., "Incoherent Radiation from Plasmas," Phys. Rev., Vol. 116, 1959, p. 1051.
39. Parzen, P. and Goldstein, L., "Current Fluctuations in the Direct Current Gas Discharge Plasmas," Phys. Rev., Vol. 82, 1951, p. 724.

LIST OF REFERENCES - (continued)

40. Bekefi, G. and Brown, S. C., "Microwave Measurements of the Radiation Temperature of Plasmas," J. Appl. Phys., Vol. 32, 1961, p. 25.
41. Bekefi, G., Hirschfield, J. L. and Brown, S. C., "Kirchhoff's Radiation Law for Plasmas with Non-Maxwellian Distributions," Phys. Fluids, Vol. 4, 1961, p. 173.
42. Brangaccio, D. J., "Construction of a Gaseous Optical Maser using Brewster Angle Windows," Rev. Sci. Instr., Vol. 33, 1962, p. 921.
43. Condon, E. U. and Shortley, G. H., The Theory of Atomic Spectra, Cambridge University Press, New York, 1964, p. 98.
44. Nord, A., Contract No. AF 61(052)-895, Scientific Report No. 1, 1966.
45. Cairns, R. B. and Emeleus, K. G., "The Longitudinal Pressure Gradient in Discharge Tubes," Proc. Phys. Soc. (London), Vol. 71, 1958, p. 694.
46. Langmuir, I., J. Franklin Inst., Vol. 196, 1923, p. 751.
47. Druyvesteyn, M. J., Physica, Vol. 2, 1935, p. 255.
48. Leiby, C. C., Jr., Phys. Fluids, 1966, to be published.
49. Wada, J. Y. and Heil, H., "Electron Energy Spectra in Neon, Xenon and Helium-Neon Laser Discharges," Q. E., Vol. 1, 1965, p. 327.
50. Meissner, K. S. and Miller, W. F., "Influence of Irradiation on the Characteristic of a Glow Discharge in Pure Rare Gases," Phys. Rev., Vol. 92, 1953, p. 896.
51. Labuda, E. F. and Gordan, E. I., "Microwave Determination of Electron Energy and Density in He-Ne Discharges," J. Appl. Phys., Vol. 35, 1964, p. 1647.
52. Moore, C. E., Atomic Energy Levels, Vol. III, Circular of National Bureau of Standards, Vol. 467, 1958, p. 113.
53. Clark, P. O., Huback, R. A. and Wada, J. Y., "Investigation of the DC-Excited Xenon Laser," JPL Contract No. 950803, Hughes Research Laboratories, Malibu, 1965.
54. Bates, D. R. and Damgaard, A., "The Calculation of the Absolute Strengths of Spectral Lines," Phil. Trans. Proc. Roy. Soc. (London), Vol. A242, 1950, p. 101.

LIST OF REFERENCES - (continued)

55. Clark, P. O., "Investigation of the Operating Characteristics of the 3.51 μ Xenon Laser," Q. E., Vol. 1, 1965, p. 109.
56. Brown, S. C., Basic Data of Plasma Physics, John Wiley and Sons, Inc., New York, 1959, p. 7.
57. Cobine, J. D., Gaseous Conductors, Dover Publications, Inc., New York, 1958, p. 44.
58. Pack, J. L., Voshall, R. E. and Phelps, A. J., "Drift Velocities of Slow Electrons in Krypton, Xenon, Deuterium, Carbon Monoxide, Carbon Dioxide, Water Vapor, Nitrous Oxide and Ammonia," Phys. Rev., Vol. 127, 1962, p. 2084.
59. Wagner, K. H., "Mittlere Energien und Driftgeschwindigkeiten von Elektronen in Stickstoff, Argon und Xenon, ermittelt aus Bildverstärkeraufnahmen von Elektronenlawinen," Z. Physik, Vol. 178, 1964, p. 64.
60. Massey, J. T., Schultz, A. G., Hocheimer, B. J. and Cannon, S. M., "Resonant Energy Transfer Studies in a Helium-Neon Gas Discharge," J. Appl. Phys., Vol. 36, 1965, p. 658.
61. Lamb, W. E., Jr., "Theory of an Optical Maser," Phys. Rev., Vol. 134, 1964, p. A1429.
62. Freiberg, R. J., Weaver, L. A. and Verdeyen, J. T., "Infrared Laser Interferometry Utilizing Quantum-Electronic Cross Modulation," J. Appl. Phys., Vol. 36, 1965, p. 3352.